Stony Brook University

Cooling, Trapping, and Transport of Atom Clouds in a New BEC Apparatus

A Thesis Presented

by

Stephan Gerhard Albert

to

The Graduate School

in Partial Fulfillment of the

Requirements

for the Degree of

Master of Arts

in

Physics

Stony Brook University

August 2007

Stony Brook University

The Graduate School

Stephan Gerhard Albert

We, the thesis committee for the above candidate for the

Master of Arts degree, hereby recommend

acceptance of this thesis.

Dominik Schneble - Thesis Advisor
Assistant Professor, Department of Physics and Astronomy

Harold Metcalf
Distinguished Teaching Professor, Department of Physics and Astronomy

Thomas Bergeman
Adjunct Professor, Department of Physics and Astronomy

This thesis is accepted by the Graduate School.

Lawrence Martin
Dean of the Graduate School

Abstract of the Thesis

Cooling, Trapping, and Transport of Atom Clouds in a New BEC Apparatus

by

Stephan Gerhard Albert

Master of Arts

in

Physics

Stony Brook University

2007

This thesis discusses laser cooling, magnetic trapping, and mechanical transport of ultracold atom clouds of rubidium in a new Bose-Einstein condensation (BEC) apparatus. After an introduction on different apparatus designs and a discussion of the techniques employed in our experiment, we describe the development of a preparation sequence for subsequent evaporative cooling and characterize the single stages.

We demonstrate a promising efficiency of the entire sequence: up to 1.2×10^{10} atoms can be caught from a rubidium vapor with a magneto-optical

trap, then compressed, and further cooled by optical molasses. The cloud is subsequently transferred into a quadrupole magnetic field. The coils for this magnetic trap are mounted on a translation stage, which moves the atoms to a 10^{-12} torr vacuum glass cell where evaporative cooling will be performed. We can transfer about 2.5×10^{9} atoms to this glass cell. We measure parameters important for successful evaporation and discuss the realizability of BEC in our apparatus.

parentibus carissimis

Contents

List of Figures

List of Tables

Acknowledgements

Two weeks before my return home, I am looking back on an interesting year in my life, which will remain in my memory mostly for the work in Dominik Schneble's group. I want to express my gratitude to him first and foremost. After three years of studies at my home school TUM that were characterized by theoretical teaching, homework, and exam-preparation rather than research, he gave me the opportunity to conduct concrete experimental work for the first time in my life as a physicist. Not only to execute the routine work in the lab, but also to develop and propose my own ideas was an especially motivating experience. It was also Dominik who convinced me to write this thesis, which had not been my initial intention, but yet definitely a good decision. He is a great teacher with an astonishing ability to give descriptive explanations of complex phenomena and an almost inexhaustable patience. Knowing both the American and the German academic system, he has also been an particularly valuable advisor. Most important, however, his uncomplicated, pleasant, and humorous personality made it fun to work in his lab, even in nights when the lasers were not turned off before dawn.

I also want to thank the other students in the group: David Sproles, who started with Dominik two years ago and set up the laser and the vacuum

system, taught me the basic operation principles in my first weeks. Rebekah Schiller proof-read large parts of the manuscript of this thesis. She has been a source of good mood for the entire lab, unflagging in mounting and aligning optics, and explained to me what is so special about being a Southerner. She has become a very good friend. Daniel Pertot designed the subtle electronics for the TOP trap and is the expert for electronic issues. He tracked down and eliminated all kinds of frequency noise. Now finished, his TOP coils work perfectly. Daniel Greif, who started working in the group in January, reduced my considerable work load from the fall term and developed the radio-frequency evaporation. He enriches the physical reflections of all group members with challenging questions he encounters during his study of the literature, and gave me his notes from the class on General Relativity which I often missed due to nights spent in the lab. Azure Hansen was always a helping hand for the entire group and shares my passion for mountains. I was often amazed by the wide knowledge of physics she has already acquired at her young age and wish her all the best for her graduate studies.

We did not achieve Bose-Einstein condensation during my stay, but I am certain that the group will succeed very soon and thus open the way for the actual experiments with optical lattices. During my time in the group, we had to struggle with frequent recurrences of bad luck: as many as four laser diodes had to be replaced within a period of eight months. The last one died on the night when Rebekah, Daniel, and Dominik had very likely been just one or two steps away from condensation. I am convinced, though, that the group's misfortune is now depleted and the progress will be much faster in the

next year.

I am also grateful for all teachers that I had at Stony Brook and want to mention especially Hal Metcalf whose lecture on laser cooling helped my understanding of the lab work a lot.

The Fulbright program supported my exchange year at Stony Brook with a generous scholarship.

Vor allem möchte ich aber meiner Familie und besonders meinen Eltern danken. Ohne ihre Unterstützung, ihren Glauben an mich und ihren Zuspruch in persönlich schwierigen Zeiten wäre die Anfertigung dieser Arbeit nicht möglich gewesen. Ihnen ist sie deshalb gewidmet.

Chapter 1

Introduction

In 1924 the Indian physicist Satyendra Nath Bose derived the spectrum of Planck's blackbody radiation by purely statistical arguments using the principle of indistinguishability of radiation quanta. He sent his article to Albert Einstein, who translated it to German, published it [1], and extended the work with considerations about the properties of the monatomic ideal quantum gas [2–4]. He predicted that below a certain (very low) critical temperature T_c, a considerable ("macroscopic") fraction of the gas atoms would gather in the common lowest energy level. The gas would undergo a phase-transition. This phenomenon became known as "Bose-Einstein condensation" (BEC).

Einstein's derivation only relates to non-interacting particles. It had been doubted that Bose-Einstein condensation could occur in reality because of the interaction between particles in any physical system. It was soon realized, however, that superfluidity in liquid helium, a strongly interacting system, discovered in 1937, could be understood with the theory of Bose-Einstein condensation. The phenomenon of superconductivity can also be regarded as

Bose-Einstein condensation of coupled electron pairs, so-called Cooper pairs. In dilute gases, the first Bose-Einstein condensates were observed in 1995, disproving the assumption that gases would solidify long before reaching the conditions for condensation. Three competing research teams were successful in that year: the group of Carl Wieman and Eric Cornell in Boulder [5] with the element rubidium, the group of Wolfgang Ketterle at MIT (sodium) [6], and the group of Randall Hulet at Rice University (lithium) [7–9][1]. The years following the observation of Bose-Einstein condensate in gases in 1995 were marked by extensive research on a great variety of fascinating properties Bose-Einstein condensates exhibit, such as observation of interference between two condensates [10], the realization of the first "matter laser" [11–13], phase-coherent amplification [14, 15], vortices [16, 17], the observation of Feshbach resonances, BEC in optical lattices, and the study of strongly correlated systems [18–20].

1.1 Bose-Einstein condensation - some quantum statistics

In this section we will summarize briefly the results of the statistical theory of Bose gases. For a more detailed treatment the reader is referred to the standard literature, e. g. [21, 22].

In a system of non-interacting bosons the average occupation $f(\epsilon_k)$ of a state

[1]The analysis of 1995 was corrected in 1997: the originally reported number of 2×10^5 condensed atoms was corrected to 1000. The conclusion that BEC had been observed, however, remained unchanged.

with single particle energy ϵ_k is:

$$f(\epsilon_k) = \frac{1}{\mathrm{e}^{\beta(\epsilon_k - \mu)} - 1} \quad , \tag{1.1}$$

where $\beta = \frac{1}{k_\mathrm{B} T}$, with T the temperature and μ the chemical potential. The total number of particles is then just given by summation of the above expression over all single particle states k, which can - for small energy spacings - be expressed as the integral:

$$N(T, \mu) = \int_0^\infty \frac{g(\epsilon)}{\mathrm{e}^{\beta(\epsilon - \mu)} - 1} \mathrm{d}\epsilon \quad , \tag{1.2}$$

where it was necessary to multiply by the density of states $g(\epsilon)$ in order to go from summation to integration properly. If the particles of mass m are confined in an anisotropic harmonic potential $U(x, y, z) = \frac{1}{2} m \left(\omega_x^2 x^2 + \omega_y^2 y^2 + \omega_z^2 z^2\right)$ as in most BEC experiments, the density of states, for example, is $g(\epsilon) = \frac{1}{2} \frac{\epsilon^2}{\hbar \omega}$, where $\omega := \sqrt[3]{\omega_x \omega_y \omega_z}$. For a gas confined in a box with volume V, $g(\epsilon)$ is $\frac{1}{(2\pi)^2} V \left(\frac{2m}{\hbar^2}\right)^{3/2} \sqrt{\epsilon}$. Bose-Einstein condensation occurs for a fixed atom number N at the **critical temperature** T_c, where the chemical potential $\mu(T)$, implicitly given by equation 1.2, becomes zero. The integral for this point $\mu(T_\mathrm{c}) = 0$ can be expressed as:

$$\frac{N}{V} = \frac{\left(2\pi m k_\mathrm{B} T_\mathrm{c}\right)^{3/2}}{\left(2\pi\hbar\right)^3} \zeta(3/2) \quad \text{for the gas in the box} \tag{1.3}$$

and

$$N = \left(\frac{k_{\mathrm{B}} T_{\mathrm{c}}}{\hbar\omega}\right)^3 \zeta(3) \quad \text{for the gas in the harmonic potential,} \tag{1.4}$$

where $\zeta(s) = \sum_{n=1}^{\infty} \frac{1}{n^s}$ is the Riemann Zeta-function, $\zeta(3) \approx 1.202$, $\zeta(3/2) \approx 2.612$. Defining the **thermal de Broglie wavelength** λ_{T} as

$$\lambda_{\mathrm{T}} = \frac{2\pi\hbar}{\sqrt{2\pi m k_{\mathrm{B}} T}} \quad , \tag{1.5}$$

we can give a criterion for BEC (for the gas in the box):

$$n\lambda_{\mathrm{T_c}}^3 \cong 2.612 \quad , \tag{1.6}$$

with $n = \frac{N}{V}$ the (number) density. The product $n\lambda_{\mathrm{T}}^3$ is also called "**phase space density**" $\mathcal{D}$. For a harmonic potential[2], a straightforward calculation gives the fraction of condensed particles from equation 1.2[3]:

$$\frac{N_0}{N} = 1 - \left(\frac{T}{T_{\mathrm{c}}}\right)^3 \quad \text{for} \quad T < T_{\mathrm{c}} \quad , \tag{1.7}$$

where N is the total number of particles and N_0 the number of condensed particles. The results in equations 1.6 and 1.7 give criteria for condensation that are very descriptive: BEC occurs at a critical temperature T_{c} when the

[2]For the gas in the box, the calculation is analog and the exponent in equation 1.7 is 3/2.

[3]Because $g(\epsilon = 0) = 0$, the integral does not count particles in the ground state, so for a macroscopic occupation of the ground state N_0, it only gives the number of atoms in excited states $N_{\mathrm{ex}} = N - N_0$, the "uncondensed fraction". By calculating, however, N with the parameters ($T = T_{\mathrm{c}}$, $\mu = 0$) and N_{ex} with ($T < T_{\mathrm{c}}$, $\mu = 0$) separately, one retrieves the number of condensed atoms by subtraction: $N_0 = N - N_{\mathrm{ex}}$.

thermal wavelength λ_{T}, i. e. the atoms' de Broglie wavelength associated with their thermal motion, becomes comparable to the typical distance between particles $(V/N)^{1/3}$. The more the gas is cooled under the transition temperature T_{c}, the more the single particle wavefunctions will overlap with each other. At $T = 0$, they form one big wavefunction which describes all of them. The particles have lost their "individuality" and become a pure condensate.

The fact that BEC in gases is a metastable phenomenon (with respect to the solid state) dictates the necessity of very low densities. In alkali gases, they should not exceed $\sim 10^{14}\,\mathrm{cm}^{-3}$. This, in turn, results in extremely low critical temperatures: the typical range is some hundred nanokelvins to a few microkelvins. It was soon clear that this temperature regime could not be reached with traditional cooling methods. Instead, the realization of BEC in alkali gases is intimately linked with the emergence and development of laser cooling in the 1980s [23], an entirely new field of atomic physics on its own. But even the astonishing capabilities of laser cooling mechanisms alone are not sufficient to produce the temperatures and densities needed. The final key for the realization of BEC was surprisingly simple: evaporative cooling, first proposed by Hess [24], could lower the temperature to and below the critical point. This mechanism is just what everybody knows from daily-life experience about the cooling down of a hot cup of tea: the hottest molecules in the liquid have so much thermal energy that they are able to escape it, each of them carrying away higher-than-average thermal energy. Thus, the remaining molecules rethermalize at a new, lower average energy. The necessary confinement of the atom cloud in a conservative potential during this final cooling

phase is provided by magnetic or optical trapping, which is the third major tool for successful condensation.

In the following section we will give a quick overview on the different experimental methods that successfully led to BEC. In the next chapter, we will then explain our own apparatus, which employs many standard techniques, but also exhibits some novel technological aspects.

1.2 Different designs

Almost all BEC machines have the combination of laser cooling, magnetic trapping, and evaporative cooling in common. Laser cooling (and trapping) reduces the temperature to a regime where the atoms can then be magnetically trapped. Once confined in a magnetic trap, the atoms are further cooled by evaporation. Different machine designs are different answers to some typical challenges that every new BEC experiment faces: one of them is the different requirements of laser cooling and evaporative cooling on pressure: evaporative cooling is a lengthy process and thus requires a very low gas pressure in order to not lose the magnetically trapped cloud by collisions with the background gas before condensation occurs. A common technique used for pre-cooling, the so called vapor cell magneto-optical trap (MOT), needs, however, a significantly higher background pressure in order to cool and trap a considerable amount of atoms. The operation principle of a MOT, first demonstrated by Raab *et al.* [25], will be discussed in more detail in section 2.4. For the purpose of this overview, the MOT may be described as a laser cooling mechanism in the

presence of a quadrupole magnetic field. The optical forces, in combination with the field, not only slow down, i. e. cool the atoms, but also trap them at the minimum of the magnetic field. Alternatively to the method described in this thesis, the aforementioned pressure issue, peculiar for the vapor cell MOT, can be avoided by loading the MOT not from a vapor, but from a slow atomic beam, produced by a Zeeman slower [26].

Another concern is the choice of the field geometry of the magnetic trap, for it turns out that certain traps, namely those with a vanishing magnetic field at the "bottom of the trap" (the local minimum of the trapping potential), have a "hole" at exactly that point: in a magnetic trap only atoms in certain magnetic hyperfine states ("trapped spin state") experience a confining potential while for atoms with an opposite spin quantum number the potential is repelling. The degeneracy of those states at zero field is removed in a magnetic field by the well-known Zeeman effect. Due to the possibility of spin flips to untrapped states ("Majorana losses") in regions of negligible fields, magnetic traps with a field zero at their bottom "leak out". This is not dramatic for the temperatures achieved by laser cooling, for which the relative size of that hole with respect to the total size of the cloud is small. However, the losses become severe during evaporative cooling. In fact, it is not possible to get even close to BEC with this obstacle. A typical example for traps with this problem is the magnetic quadrupole field (section 2.7).

The atoms are usually evaporated by applying radio frequency (RF), which can flip the spin state of an atom from a trapped to an untrapped state. Atoms in an untrapped state are repelled from the trap region and

thus removed from the rest of the trapped atomic cloud. In an inhomogeneous magnetic field, as in a magnetic trap, the energy splitting of the spin states is position-dependent. This allows to tune the RF so that only the outmost, i. e. hottest atoms are flipped. Evaporative cooling is then executed by slowly ramping down the frequency of the "RF knife".

The first BEC realized in Boulder [5] used a rubidium vapor cell magneto-optical trap (MOT). The atoms pre-cooled by the MOT were (after a compression of the MOT, see section 3.4) trapped with a quadrupole trap. Majorana losses were eliminated by adding a rotating bias field to the quadrupole field. This invention became known as TOP ("time-orbiting potential") trap [27]. The setup characterized in this thesis uses this scheme as well[4]. Evaporation was then performed by means of RF. Because the atoms were evaporated in the vapor cell itself, the observed BEC was small compared to the later experiments because of the pressure limitations described above.

The MIT experiment [6] took a different approach to BEC in some aspects. A Zeeman slower was used to load the atoms into a "dark SPOT" ("spontaneous-force optical trap") [28], a modification of the MOT. In this way, the problems of a vapor cell were avoided and the dark SPOT provided sufficiently high densities as a starting point for evaporation. In this experiment, the hole in the magnetic trap was quite literally "plugged" by focusing a laser beam to the center of the trap. The resulting optical dipole force repelled the atoms from the trap center.

A method used to solve the pressure dilemma in the vapor cell was the

[4]By the time this thesis was written the TOP trap had been designed, constructed, and extensively characterized, but not yet operated.

invention of the double MOT [29, 30]. This approach uses two MOTs: the first ("dirty" MOT) is placed in a chamber of the vacuum system where it can quickly load from an atomic vapor. By multiple transfer of the trapped atoms, the second ("clean") MOT, installed in a region with a pressure more than one order of magnitude lower than in the first chamber, is loaded. Also, the quadrupole field was replaced in many experiments by more complicated coil geometries, described in reference [31], which have a non-vanishing magnetic field at the potential minimum. Among them, the Ioffe-Pritchard, first implemented in reference [25], is the most prominent type. A variant of it was used for BEC by the MIT group as early as 1996 [32]. The first condensate in a pure Ioffe-Pritchard trap was demonstrated in 1998 [33].

BEC has also been demonstrated without the use of magnetic trapping. Instead, after conventional cooling with a MOT, the atoms were trapped by two intersecting high power laser beams, employing the intensity dependent optical dipole force [34]. The trapped cloud was then evaporatively cooled by lowering the intensity of the lasers, thereby decreasing the height of the potential and not overly reducing the trap stiffness. The method was called "all-optical" BEC although this term is misleading, because the experiment still employed a MOT, which does use a magnetic field. The final cooling was also conducted by an evaporation procedure, and not by laser cooling, which might be suggested by the term "all-optical".

Another innovation was the production of a BEC on a microelectric chip [35, 36]. Here, the magnetic trap consists of fields generated by lithographic conductors on the chip and external bias fields. The advantage of this ap-

proach is the realizability of much higher magnetic field gradients than in the conventional scheme, leading to better confinement and faster rethermalization during evaporation. The entire evaporation stage on a microchip lasts about 1 s, a factor of 20 less than in standard magnetic traps, and the requirements on background pressure are thus less stringent. The experiments also demonstrated the transport of a condensate along an "atomic conveyor belt" on the chip [35].

The idea of the double MOT design, namely spatial separation of the capture and laser cooling part from the evaporation part can also be achieved by transport of magnetically trapped clouds. This was realized in two variants: a chain of quadrupole coils was built to guide atom clouds from a MOT to the magnetic trap in which evaporation was executed [37]. A second approach is the mechanical transportation of cooled and trapped atoms just with one quadrupole trap that is mounted on a translation stage [38]. The trap moved by the stage can thus freely travel through the vacuum system. The design of our experiment is inspired by this idea.

Chapter 2

Description of the apparatus and theory of the employed techniques

This chapter will give an overview of our BEC apparatus. The apparatus is designed to produce condensates from the ^{87}Rb-isotope of the element rubidium. This overview will be followed by explanations of the theory and the basic principles of the employed cooling and trapping techniques intended for a reader unfamiliar with this field.

2.1 Overview

Figure 2.1 shows a schematic view of the apparatus. The two core parts are the vapor cell (or "MOT cell") and the science cell ("glass cell"). This realizes a spatial separation of the laser-cooling (vapor cell) and the evaporative cooling (science cell) stages of the experiment in regions with suitable pressures. The vapor cell consists of Pyrex glass and the science cell of quartz glass. The shape of the vapor cell is cylindrical with an outer diameter of 5.7 cm. Its

axis is oriented in the x-direction[1]. The science cell is cuboidal. Its width (y-direction) is 1.0 cm and its height (z) 2.0 cm (inner dimensions). Both cells are placed in different regions of a vacuum system, which is pumped by two ion pumps, one for each region. The regions are connected by a differential pumping tube ("thin tube"). The vapor cell is characterized by a non-rubidium pressure of $\sim 2\times10^{-10}$ torr and typical rubidium pressures of 10^9-10^8 torr while the pressure in the ultra-high vacuum science cell is less than 5×10^{-12} torr. We will sometimes refer to the transfer chamber between the differential pumping tube and the science cell as "square chamber". The vacuum system is to be treated in more detail in reference [39]. Connected to the vapor cell is the rubidium oven, which provides the rubidium gas in the vapor cell. The oven can be manually opened and its temperature is controllable.

Up to 1.2×10^{10} Rb atoms are captured, laser-cooled, and trapped with a magneto-optical trap (MOT) directly from the vapor (section 2.4) in a time of ~ 10 s. At this point, the cloud has a temperature of a few hundred microkelvins. The magnetic field is generated by a fast-switching quadrupole magnetic trap (section 2.7). Residual magnetic fields, such as Earth's magnetic field, are eliminated by three bias field coils (not shown). Subsequent to the MOT stage, a sudden compression of the MOT (section 3.4) within ~ 500 ms increases the density of the atomic cloud. This stage is immediately followed by laser cooling via optical molasses (section 2.5) for ~ 5 ms, which lowers the temperature to $\sim 25\ \mu$K, a temperature that clearly indicates sub-Doppler cooling mechanisms (section 2.6). Optical pumping (section 3.6) for a

[1]See the figure for definition of the lab coordinate system.

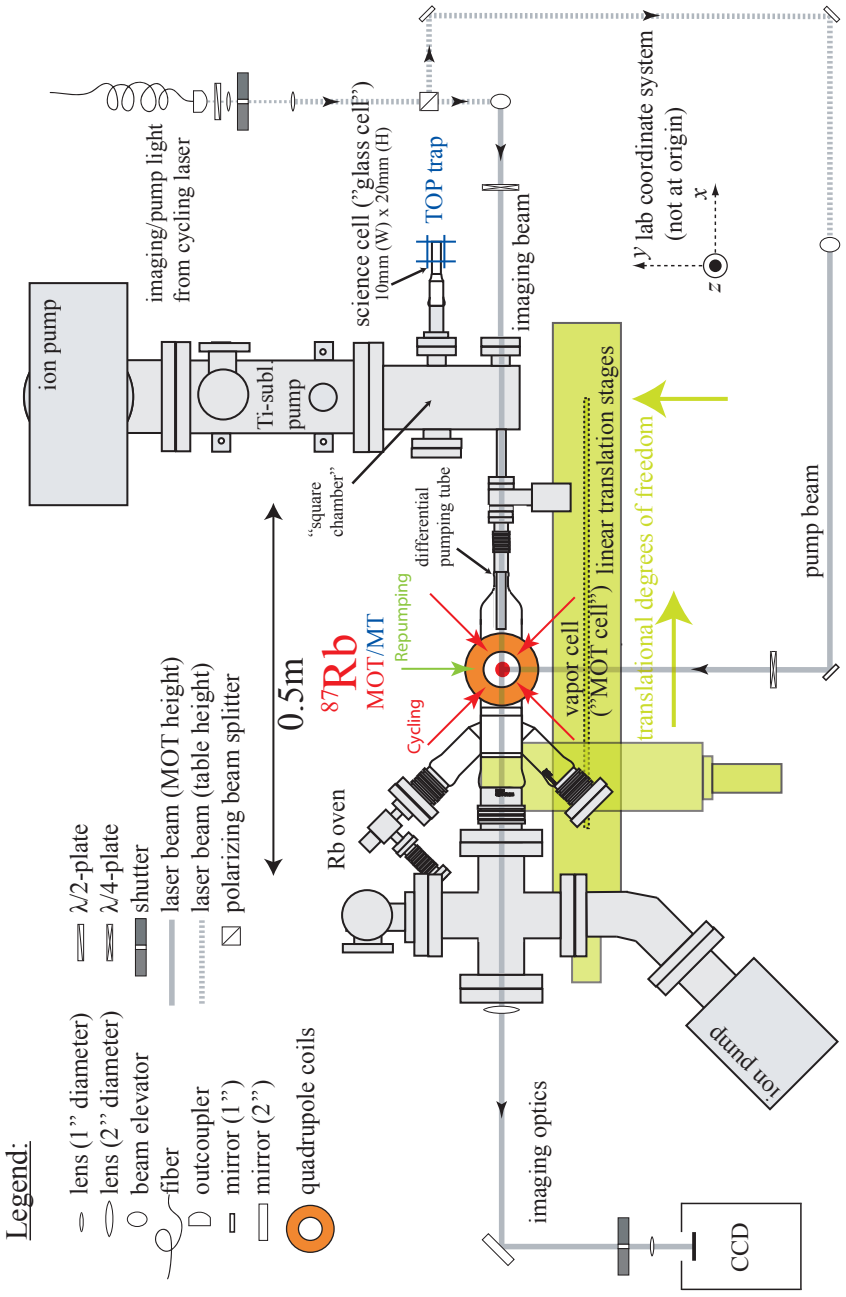

Figure 2.1: The apparatus: the figure shows a schematic drawing (to scale) of the parts of the apparatus that are relevant for the discussion of this thesis. The MOT optics and laser system, however, are not shown in this figure. The apparatus also includes: coils for bias fields, cooling hoses and holders for the quadrupole coils, various stages for optical installations etc.

few milliseconds then increases the number of atoms in magnetically trappable atomic states. The cloud, having been prepared thusly, is then caught in a magnetic trap (section 2.7) produced by the same quadrupole coils that create the magnetic field for the MOT. We can catch 1-3$\times 10^9$ atoms in the magnetic trap. Immediately after the catch, the temperature of the cloud is $\sim 80\,\mu$K. A quasi-adiabatic compression in the magnetic trap raises the temperature to $\sim 350\,\mu$K. The quadrupole coils are mounted on a mechanical translation stage that can freely travel in the x and y-directions, allowing movement of the trapped atoms through the vacuum system. The transport of the trapped cloud already starts during compression of the trap and guides the atoms on a z-shaped path to the UHV region. We can transfer the atoms with an efficiency of $\sim$ 70-80 % in $\sim 3.5\,$s from the vapor cell to the science cell (section 3.8), where the evaporation will then be performed. The TOP trap for the evaporation has already been designed and constructed, but not yet operated. We do not use an additional magnetic trap in the science cell: the TOP trap just consists of the same quadrupole coils used for the MOT and the transport and two smaller coil pairs that create the rotating bias field. The TOP trap will not be described in this thesis.

2.2 Rubidium and laser system

The set of elements which can be Bose-condensed is limited by some constraints: 1) Needless to say, they must be bosons. 2) Laser cooling must (generally) be possible, which limits the choice to alkali, alkaline-earth atoms,

and some metastable noble gases. 3) High-power laser light must be available. 4) The element must have a favorable ratio of so-called "good" collisions, which support rethermalization, to "bad" collisions, which cause trap losses. Because of these limitations, BEC was originally pursued in alkalis and spin-polarized hydrogen (which is an exceptional case, for it is not laser-cooled). After the observation of BEC in ^{87}Rb [5], ^{23}Na [6], and ^{7}Li [7] in 1995, it was also reported in atomic hydrogen [40], ^{85}Rb [41], ^{41}K [42] [2], metastable ^{4}He [43, 44], ^{133}Cs [45], ^{174}Yb [46], and ^{52}Cr [47]. For this experiment, rubidium was chosen. It can be cooled with low priced diode lasers (instead of expensive dye lasers), and it also exhibits favorable properties for the optical lattice experiments that will be performed in this research group.

Laser cooling relies on the scattering of photons by the atoms that are to be cooled. In the simplest picture, atoms moving in a certain direction are slowed down, hence cooled, by a bombardment of photons traveling in the opposite direction. The photons come from a laser that is tuned to a transition frequency of the atomic level structure. They are absorbed by the atom, which consequently goes to an excited internal state. The momentum of a photon $\hbar k$, with $k = \frac{2\pi}{\lambda}$ and λ the laser light wavelength[3], is transferred to the atom by a first kick slowing it down. The atom returns to its internal ground state by spontaneous reemission of the photon in a *random* direction. To conserve momentum, the atom experiences a second recoil kick in the direction opposite

[2]BEC in ^{85}Rb and ^{41}K was indirectly obtained by evaporation of (^{87}Rb), which was in thermal contact with those gases during the process, a method called "sympathetic cooling".

[3]Definitions of abbreviations with a global meaning in the context of this thesis, such as λ, may not be repeated every time they appear. Instead, the reader can find a list of those abbreviations in appendix D.

to that reemission. Because of the random nature of this second recoil kick, its net effect after many scattering events is zero while every absorption event slowed the atom down by $\hbar k/m$ in its defined direction of travel. It can also be easily shown that the energy of the emitted photons is higher than that of the absorbed photons due to the Doppler effect. The energy difference is supplied by the kinetic energy of the atoms. Thus, the atom's velocity in its direction of travel is reduced.

To slow down atoms from room temperature to close to 0 K, tens of thousand scattering events are necessary. For this reason, one needs a **closed transition** within the atomic level structure, i. e. the atom needs to return after every excitation to the same ground state it came from. Atoms that have fallen into another ground state are lost because the laser light can only couple one specific ground state to one specific excited state. Rubidium (as all alkalis) provides such a closed transition. Figure 2.2 shows the D_2-line of the level structure of ^{87}Rb. Important data for ^{87}Rb is found in appendix D. We use the $5\,^2S_{1/2}, F = 2 \rightarrow 5\,^2P_{3/2}, F' = 3$-transition to cool the atoms. Because of the iterative nature of the process, it is usually called the "**cycling transition**" and the laser used is referred to as cycling laser. This is a closed transition because of the selection rules for angular momentum. For the hyperfine quantum number F only $\Delta F = 0, \pm 1$ is allowed in a transition. Thus, atoms in the $F' = 3$-state can only decay to the $F = 2$-state. Hence, the cycling laser is tuned to that frequency. The cycling laser in our experiment is an external cavity diode laser built by Sacher Lasertechnik with an output power of ~ 1000 mW. It is frequency-stabilized with a polarization spectroscopy locking

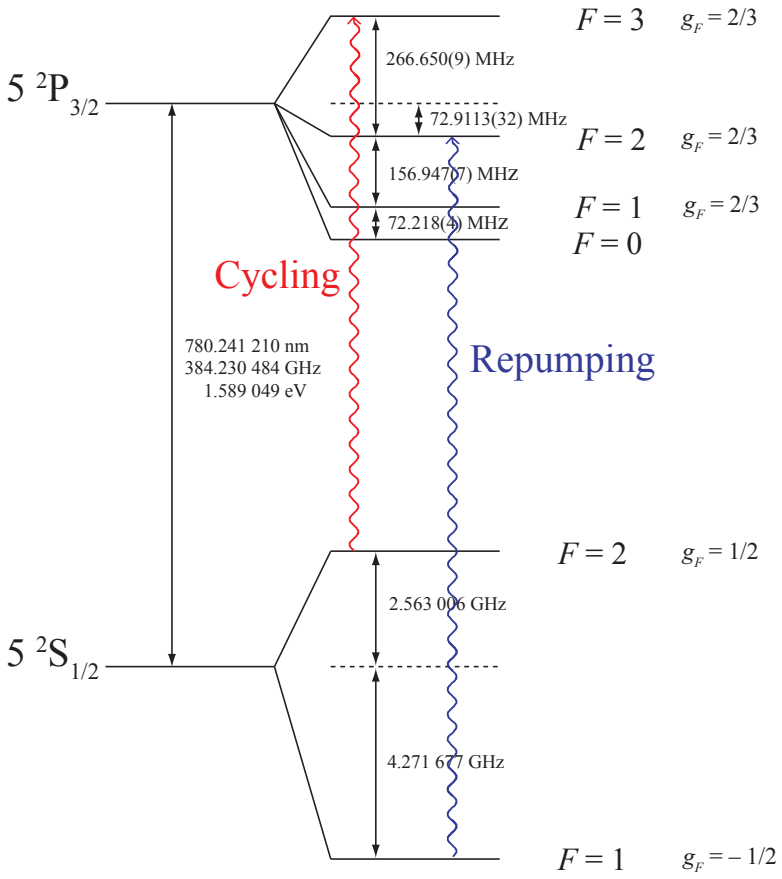

Figure 2.2: Relevant part of the level structure of ^{87}Rb (D_2-line): the cycling $F = 2 \rightarrow F' = 3$ and the repump transition $F = 1 \rightarrow F' = 2$ are marked. The drawing is not to scale. The data is taken from reference [48].

technique described in reference [49]. Detuning from the locking frequency and power can be controlled with acousto-optical modulators. A small amount of the laser power is used for absorption imaging (chapter 3) and optical pumping (chapter 3). The cycling light is coupled into an optical fiber which guides it to the (separate) table with the vacuum apparatus and the MOT optics, for which $\sim 250\,\mathrm{mW}$ of laser power are available. The laser system and the locking techniques will be described in more detail in reference [39].

The cycling transition is not totally closed, however. Because of the small energy spacing in the $5\,^2\mathrm{P}_{3/2}$ between $F' = 3$ and $F' = 2$ of $\sim \hbar \times 2\pi \times 267\,\mathrm{MHz}$, atoms can also be excited to the $F' = 2$ by the cycling laser with a small, but considerable probability. From there, they can not only decay to $F = 2$, but also to $F = 1$, where they are lost for the cooling process. For this reason one needs a second laser which is commonly called the "**repumper**". It is tuned to the $5\,^2\mathrm{S}_{1/2}, F = 1 \rightarrow 5\,^2\mathrm{P}_{3/2}, F' = 2$-transition and excites the atoms to the $F' = 2$-state so that they can decay back to the $F = 2$-state, thus bringing the "lost" atoms back into the cooling cycle. The repumper in this experiment is also an external cavity diode laser, made by Toptica Photonics. Its output power is $\sim 120\,\mathrm{mW}$. It is frequency-stabilized with the same method as the pumping laser. Its light runs directly to the vapor cell.

2.3 Atom-light interaction and laser cooling - a very short introduction

The next paragraphs will be devoted to some basic aspects of the theory of atom-light interaction which are necessary to understand the following sections on magneto-optical trapping, optical molasses, and sub-Doppler cooling. Most importantly, we will touch on the Rabi two-level problem, which serves as a model in many descriptions of laser cooling mechanisms. Complete derivations of the results are beyond the scope of this thesis and will not be given. Rather, we will point out the important steps and the usual assumptions made in the derivations. We will also neglect all phenomena that do not directly relate to

the techniques used in this experiment. The section follows largely the book by Metcalf and van der Straaten [23]. An exhaustive theoretical treatment of the subject can be found in reference [50].

2.3.1 Time-dependent perturbation theory and two-level problem

In order to describe the interaction with the light field, we assume an atomic Hamiltonian $\mathcal{H}$ that can be decomposed into a time-independent part $\mathcal{H}_0$ describing the internal atomic structure and a time-dependent perturbation $\mathcal{H}'(t)$ that contains the interaction with the (classically described) radiation field. The Schrödinger equation for the atom including the interaction with the light field is then:

$$\mathcal{H}\psi(\vec{r},t) = (\mathcal{H}_0 + \mathcal{H}'(t))\,\psi(\vec{r},t) = \mathrm{i}\hbar\frac{\partial\psi(\vec{r},t)}{\partial t} \tag{2.1}$$

Since the eigenfunctions $\phi_n(\vec{r})$ of $\mathcal{H}_0$ form a complete set, we can make the following ansatz for the solution of equation 2.1:

$$\psi(\vec{r},t) = \sum_k c_k(t)\phi_k(\vec{r})\mathrm{e}^{-\mathrm{i}\omega_k t} \tag{2.2}$$

where $E_k = \hbar\omega_k$ are the eigenvalues (so the unperturbed energy states) of $\mathcal{H}_0$. This is the standard approach in time-dependent perturbation theory found in all quantum mechanics textbooks covering the subject. The ansatz leads to

coupled differential equations of the form:

$$\mathrm{i}\hbar\frac{\mathrm{d}c_j(t)}{\mathrm{d}t} = \sum_k c_k(t)\mathcal{H}'_{jk}(t)\mathrm{e}^{\mathrm{i}\omega_{jk}t} \tag{2.3}$$

where $\mathcal{H}'_{jk}(t) := \langle\phi_j\,|\mathcal{H}'(t)|\,\phi_k\rangle$ and $\omega_{jk} := \omega_j - \omega_k$. Here, the first of three major approximations is made: the atom is treated as a **two-level system** consisting only of a ground (g) and an excited (e) level, which is a reasonable assumption for an atom in a narrow-band laser field. The equations 2.3 then lead to:

$$\begin{aligned}\mathrm{i}\hbar\frac{\mathrm{d}c_\mathrm{g}(t)}{\mathrm{d}t} &= c_\mathrm{e}(t)\mathcal{H}'_\mathrm{ge}(t)\mathrm{e}^{-\mathrm{i}\omega_\mathrm{a}t}\\ \mathrm{i}\hbar\frac{\mathrm{d}c_\mathrm{e}(t)}{\mathrm{d}t} &= c_\mathrm{g}(t)\mathcal{H}'_\mathrm{eg}(t)\mathrm{e}^{\mathrm{i}\omega_\mathrm{a}t}\end{aligned} \tag{2.4}$$

where $\omega_\mathrm{a} := \omega_\mathrm{e} - \omega_\mathrm{g}$ is the atomic resonance frequency. The time dependent part of the Hamiltonian $\mathcal{H}'(t)$ for a single electron in an electromagnetic field is

$$\mathcal{H}'(t) = -e\vec{E}(\vec{r},t)\vec{r} \quad , \tag{2.5}$$

with e the elementary charge and $\vec{E}(\vec{r},t)$ the electric field of the light at the position of the atom. At this point, two other assumptions are generally made: the **rotating wave approximation** (RWA) neglects terms of the order $1/\omega_\mathrm{l}$ compared to $1/\delta$ where ω_l is the laser frequency and δ is the detuning of the laser from resonance: $\delta := \omega_\mathrm{l} - \omega_\mathrm{a}$. For a laser tuned close to the atomic resonance frequency ω_a, this is again an adequate assumption. The third important approximation is the **electric dipole approximation**. It

states that the spatial variation of the light field over the the relevant region is negligible. This approximation is also valid for the case discussed; the wavelengths in this context are usually in the range of ~ 100 - 1000 nm whereas the typical size of an atoms is ~ 1 nm. For a plane wave $\vec{E}(\vec{r},t) = E_0\hat{\epsilon}\cos(kz - \omega_l t)$, the matrix element $\mathcal{H}'_{\mathrm{eg}}(t)$ of the time-dependent Hamiltonian can be expressed as $\mathcal{H}'_{\mathrm{eg}}(t) = \hbar\Omega\cos(kz - \omega_l t)$, where the **Rabi frequency** is defined by

$$\Omega = \frac{-eE_0}{\hbar}\langle\phi_{\mathrm{e}}|\hat{\epsilon}\vec{r}|\phi_{\mathrm{g}}\rangle = \frac{-eE_0}{\hbar}\langle\phi_{\mathrm{e}}|r|\phi_{\mathrm{g}}\rangle \quad [4]. \tag{2.6}$$

With these approximations and some manipulation equations 2.4 become:

$$\begin{aligned} \frac{\mathrm{d}^2 c_{\mathrm{g}}(t)}{\mathrm{d}t^2} - \mathrm{i}\delta\frac{\mathrm{d}c_{\mathrm{g}}(t)}{\mathrm{d}t} + \frac{\Omega^2}{4}c_{\mathrm{g}}(t) &= 0 \\ \frac{\mathrm{d}^2 c_{\mathrm{e}}(t)}{\mathrm{d}t^2} + \mathrm{i}\delta\frac{\mathrm{d}c_{\mathrm{e}}(t)}{\mathrm{d}t} + \frac{\Omega^2}{4}c_{\mathrm{g}}(t) &= 0 \quad . \end{aligned} \tag{2.7}$$

These equations can be solved analytically. They yield oscillating probabilities for the atom to be in the ground or in the excited state. The frequency of these oscillations is $\Omega' := \sqrt{\Omega^2 + \delta^2}$, the generalized Rabi frequency.

2.3.2 Spontaneous emission and optical Bloch equations

As pointed out in section 2.2, spontaneous emission plays a crucial role in (conventional) laser cooling schemes, for it provides the necessary dissipation. To include spontaneous emission in the treatment of an ensemble of two-level atoms, one has to make a transition to a statistical description because of the

[4] The last equality only holds for the electric dipole approximation, which assumes that the atom dipole moment $e\vec{r}$ aligns with the polarization $\hat{\epsilon}$.

incoherence of the system. This is done by the introduction of the density matrix ρ [21]

$$\rho = \begin{pmatrix} \rho_{ee} & \rho_{eg} \\ \rho_{ge} & \rho_{gg} \end{pmatrix} \quad . \tag{2.8}$$

The equations 2.7 then lead to equations for the elements of the density matrix, for example:

$$\frac{d\rho_{gg}}{dt} = i\frac{\Omega^*}{2}\tilde{\rho}_{eg} - i\frac{\Omega}{2}\tilde{\rho}_{ge} \tag{2.9}$$

where[5] $\tilde{\rho}_{ge} := \rho_{ge}e^{-i\delta t}$. Spontaneous emission is introduced by an exponential decay of ρ_{eg}:

$$\frac{d\rho_{eg}}{dt} = -\frac{\Gamma}{2}\rho_{eg} + \text{induced effects} \quad . \tag{2.10}$$

This leads to the so-called **optical Bloch equations**:

$$\begin{aligned}
\frac{d\rho_{gg}}{dt} &= +\Gamma\rho_{ee} + \frac{i}{2}\left(\Omega^*\tilde{\rho}_{eg} - \Omega\tilde{\rho}_{ge}\right) \\
\frac{d\rho_{ee}}{dt} &= -\Gamma\rho_{ee} + \frac{i}{2}\left(\Omega\tilde{\rho}_{ge} - \Omega^*\tilde{\rho}_{eg}\right) \\
\frac{d\tilde{\rho}_{ge}}{dt} &= -\left(\frac{\Gamma}{2} + i\delta\right)\tilde{\rho}_{ge} + \frac{i}{2}\Omega^*\left(\rho_{ee} - \rho_{gg}\right) \\
\frac{d\tilde{\rho}_{eg}}{dt} &= -\left(\frac{\Gamma}{2} - i\delta\right)\tilde{\rho}_{eg} + \frac{i}{2}\Omega\left(\rho_{gg} - \rho_{ee}\right) \quad .
\end{aligned} \tag{2.11}$$

The optical Bloch equations can be easily solved for the steady-state where the time derivatives on the left hand sides of equations 2.11 are zero. One

[5] These equations are derived by assuming the relation of the density matrix of a pure state to the coefficients of the corresponding wavefunction $\rho_{eg} = c_e c_g^*$ etc. In reference [51] however, it is shown that spontaneous emission and the effects of the light field on the atom from equations 2.7 can be treated separately, thus justifying the next step.

finds:

$$\rho_{\mathrm{ee}} = \frac{s_0/2}{1 + s_0 + \left(\frac{2\delta}{\Gamma}\right)^2} \quad . \tag{2.12}$$

This is the population ratio of the atoms in the excited state to the atoms in the ground state in an ensemble of atoms. Here, we use the common **saturation parameter** s_0 which is defined as

$$s_0 := \frac{2\left|\Omega\right|^2}{\Gamma^2} = \frac{I}{I_{\mathrm{s}}} \tag{2.13}$$

where I is the intensity of the incident light beam and the **saturation intensity** I_{s} is defined as

$$I_{\mathrm{s}} = \frac{2\pi^2\hbar c}{3\lambda^3\tau} \quad \text{with} \quad \tau = \frac{1}{\Gamma} \quad . \tag{2.14}$$

This gives us finally the total **scattering rate** Γ_{sc}, which is simply the product of the population in the excited state multiplied by the decay rate of that state:

$$\Gamma_{\mathrm{sc}} = \Gamma\rho_{\mathrm{ee}} = \frac{\Gamma}{2}\frac{s_0}{1 + s_0 + \left(\frac{2\delta}{\Gamma}\right)^2} \quad . \tag{2.15}$$

This result is important because of its direct applicability for the dissipative (i. e. cooling) effects of laser light: it gives the rate by which the atoms are slowed down by portions of $\hbar k/m$. In the limit of weak intensities ($s_0 \ll 1$) equation 2.15 becomes

$$\Gamma_{\mathrm{sc}} = \frac{\Gamma}{2}\frac{I}{I_{\mathrm{s}}}\frac{\Gamma^2/4}{\Gamma^2/4 + \delta^2} \quad . \tag{2.16}$$

As a function of the detuning δ, this equation describes a Lorentzian with FWHM = Γ, the **natural linewidth** of the transition. For high intensities ($s_0 \gg 1$), $\Gamma_{\rm sc}$ saturates to $\Gamma/2$ on resonance. For intensities comparable to or greater than $I_{\rm s}$, s_0 cannot be neglected with respect to 1, and $\Gamma_{\rm sc}(\delta)$ is a Lorentzian with FWHM = $\Gamma\sqrt{1+s_0}$:

$$\Gamma_{\rm sc} = \frac{\Gamma}{2}\frac{s_0}{1+s_0}\frac{(1+s_0)\Gamma^2/4}{(1+s_0)\Gamma^2/4+\delta^2} \quad . \tag{2.17}$$

This is the well-known effect of power-broadening: in a Doppler-free spectroscopy technique, spectral lines are broadened with respect to their natural linewidth Γ if too much laser power is applied.

With these results, the **scattering cross section** of an atom $\sigma_{\rm sc}$ can be obtained with the relation $I\sigma_{\rm sc} = \hbar\omega\Gamma_{\rm sc}$. For low intensities, the dependence on I drops out and one finds the important result that the scattering cross section for atom light interaction is on the order of λ^2.

2.3.3 Light shifts

The interaction Hamiltonian $\mathcal{H}'(t)$ also effects shifts of the energy eigenstates $E_{\rm g}$ and $E_{\rm e}$. After a suitable manipulation of the Hamiltonian that offsets the energy of the excited state by $\hbar\delta$ ($c_{\rm g}(t) \rightarrow c_{\rm g}(t), c_{\rm e}(t) \rightarrow c_{\rm e}(t)\mathrm{e}^{+\mathrm{i}\delta t}$) and application of the rotating wave approximation, equations 2.4 become time-

independent and the new interaction matrix $\tilde{\mathcal{H}}'$ can be written as[6]:

$$\tilde{\mathcal{H}}' = \frac{\hbar}{2}\begin{pmatrix} -2\delta & \Omega \\ \Omega^* & 0 \end{pmatrix} \quad . \tag{2.18}$$

The eigenvalues $\lambda_{\mathrm{e,g}}$ of this matrix are:

$$\lambda_{\mathrm{e,g}} = (-\delta \mp \sqrt{\delta^2 + |\Omega|^2})\frac{\hbar}{2} \quad . \tag{2.19}$$

Expansion for low intensities ($\delta \gg |\Omega| \propto I$) yields (after reversal of the manipulation of the Hamiltonian):

$$\Delta E_{\mathrm{g}} = \frac{|\Omega|^2\hbar}{4\delta}, \qquad \Delta E_{\mathrm{e}} = -\frac{|\Omega|^2\hbar}{4\delta} \quad . \tag{2.20}$$

These energy corrections are called **light shifts**. In a strong light field, they are $\Delta E_{\mathrm{g,e}} = \pm\frac{\delta}{|\delta|}\frac{\hbar|\Omega|}{2}$. For negative detunings ($\delta < 0$), the energy levels are spread apart. An atom in the ground state is attracted to regions of high intensity. An important application of the light shift are optical lattices: in a standing wave the intensity varies spatially with a period of $\lambda/2$. Because of the light shift, atoms in such a wave experience an effective potential and are attracted to regions of higher or lower intensity depending on the detuning. The resulting force is called the **dipole force**. If the scheme is extended to three dimensions, a regular three-dimensional pattern of spots preferred by the atoms is created, just like in a crystal, and is, therefore, called an **optical lattice**. The light shift also plays an important role in the theoretical

[6]The notation is such that $\alpha\,|\mathrm{e}\rangle + \beta\,|\mathrm{g}\rangle \rightarrow \begin{pmatrix} \alpha \\ \beta \end{pmatrix}$.

description of lin $\perp$ lin-polarization gradient cooling which will be explained below (section 2.6).

2.4 The magneto-optical trap

Almost all BEC experiments use a magneto-optical trap (MOT) for pre-cooling. Since its first demonstration [25], the MOT has become the workhorse of ultracold atomic physics. It uses the combination of an inhomogeneous magnetic field and the dissipative radiative forces to cool *and* trap neutral atoms. Thus, it confines the atoms in both momentum and position space. In this respect, it differs from e. g. optical molasses, which will be described in the next section 2.5.

We will here discuss the simplest one-dimensional case of a hypothetical atom with total angular momentum $J_\mathrm{g} = 0$ in the ground state and $J_\mathrm{e} = 1$ in the excited state. In a linear magnetic field $B(z) = b_z z \equiv bz$, the Zeeman shift causes a position-dependent splitting of the three magnetic sublevels of the excited state $m_\mathrm{e} = 0, \pm 1$:

$$\Delta E_\mathrm{e} = \omega_\mathrm{Z}(z)\hbar = g_J \mu_\mathrm{B} m_\mathrm{e} B(z) = g_1 \mu_\mathrm{B} m_\mathrm{e} bz \quad . \tag{2.21}$$

Such a linear magnetic field can be generated by a quadrupole coil pair. Our experiment uses for the magnetic trapping the same quadrupole coils as for the MOT. The quadrupole field will therefore be discussed in section 2.7 about magnetic trapping. Two circularly polarized counterpropagating laser beams with opposite helicities are directed to the (spatial) region of the local min-

imum of the magnetic field strength. Figure 2.3 shows a schematic view of the situation discussed. We assume the laser light to be red-detuned, so $\delta = \omega_\mathrm{l} - \omega_\mathrm{a} < 0$. As explained qualitatively in the figure caption, the setup is such that the laser beams exert a repulsive force that drives atoms at rest to the trap center, as well as a damping force that slows down atoms that are moving away from the trap center. Quantitatively, we can calculate a force F of a laser beam on an atom by use of equation 2.15 by multiplying the scattering rate with the momentum transfer per absorption:

$$F = \dot{p} = \hbar k \Gamma_\mathrm{sc} = \frac{\hbar k \Gamma}{2} \frac{s_0}{1 + s_0 + \left(\frac{2\delta}{\Gamma}\right)^2} \quad . \tag{2.22}$$

If F_+ is the force from the σ^+-beam and F_- the force from the σ^--beam, then the total force is $F_\mathrm{MOT} = F_+ - F_-$ for low saturation. For F_+ and F_-, we just have to replace the detuning δ in equation 2.22 by effective detunings $\delta_\pm$ that take the Zeeman effect $\pm g_1 \mu_\mathrm{B} b z$ and the Doppler shift $\mp k v$ into account:

$$\delta_\pm = \delta \mp k v \pm g_1 \mu_\mathrm{B} b z \quad . \tag{2.23}$$

The total force F_MOT can be expanded if the Doppler shift and the Zeeman effect are small compared to δ. One finds:

$$F_\mathrm{MOT} \approx -\beta v - \kappa z \quad , \tag{2.24}$$

where the damping constant is $\beta = \frac{8\hbar k^2 |\delta| s_0}{\Gamma(1+s_0+(2\delta/\Gamma)^2)^2}$ and the spring constant is $\kappa = \frac{g_1 \mu_\mathrm{B} b}{\hbar k} \beta$. Those two contributions represent the dissipative, cooling and the

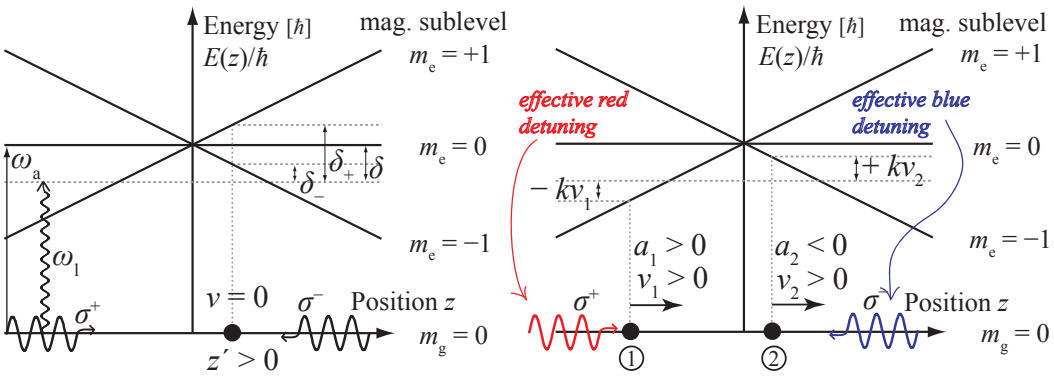

Figure 2.3: Magneto-optical trapping: the degeneracy of the magnetic sublevels is removed by the Zeeman effect. A linear magnetic field with $B(z) = bz$ is assumed. The counterpropagating beams are circularly polarized with opposite helicities as shown. The laser light is red-detuned $\delta < 0$.

The **left** figure shows an atom at rest at $z' > 0$. It is in the $m_g = 0$-state. Because both beams are circularly polarized, it can only be excited to the $m_e = 1$-state by absorption of a photon from the σ^+-beam or to the $m_e = -1$-state by absorption from the σ^--beam. For $z > 0$ and $\delta < 0$, the Zeeman effect, however, shifts the $m_e = -1$-state closer to resonance and reduces the detuning δ_- for the transition to this state while it increases the detuning δ_+ for a transition to $m_e = +1$. Thus, following equation 2.15, absorption from the σ^--beam coming from the right is more likely, which pushes the atom back to the trap center. For $z < 0$ the situation is analog with opposite signs.

The **right** figure shows an atom at $z < 0$ with positive velocity v (position 1). Its finite velocity causes a Doppler shift: it "sees" the σ^+-beam shifted to the red by $\omega_D = -kv_1$. The atom is at a position where the Zeeman shift ω_Z for $m_e = +1$ ($\delta_+ > 0$) is so large that the Doppler effect $\omega_D = -kv$ shifts the atom right in resonance for the σ^+-beam. This accelerates the atoms ($a_1 > 0$) and drives it to the trap center. At position 2 the situation is opposite: the atoms is traveling *toward* the relevant beam (σ^-). The Doppler effect is therefore a blue shift $\omega_D = kv_2$. Thus, absorption happens from the σ^--beam decelerating the atoms ($a_2 < 0$). Both situations are, however, not totally symmetric: the acceleration for $z < 0$ causes an increase of the Doppler shift, which does not correspond to the decrease of δ_+ in the direction of travel. The deceleration for $z > 0$ decreases the Doppler shift which accords with the decrease of (the absolute value of) δ_-. Qualitatively spoken, this means that the effective range of deceleration is larger than the one of acceleration: the atoms are decelerated by a larger velocity than they are accelerated. Because of that the MOT is actually able to effectively slow down and trap atoms.

restoring, trapping force in a MOT. The trapping force is also called spontaneous forces because it originates from the spontaneous emission of the atoms. This simple model can readily be extended to three dimensions so that one needs a total number of six beams (figure 2.4). If one considers real atoms, the magnetic sublevel structure is more complicated, but it was shown in computer simulations [25] and – more important, experimentally – that the technique not only works in the simple example given above, but also in reality.

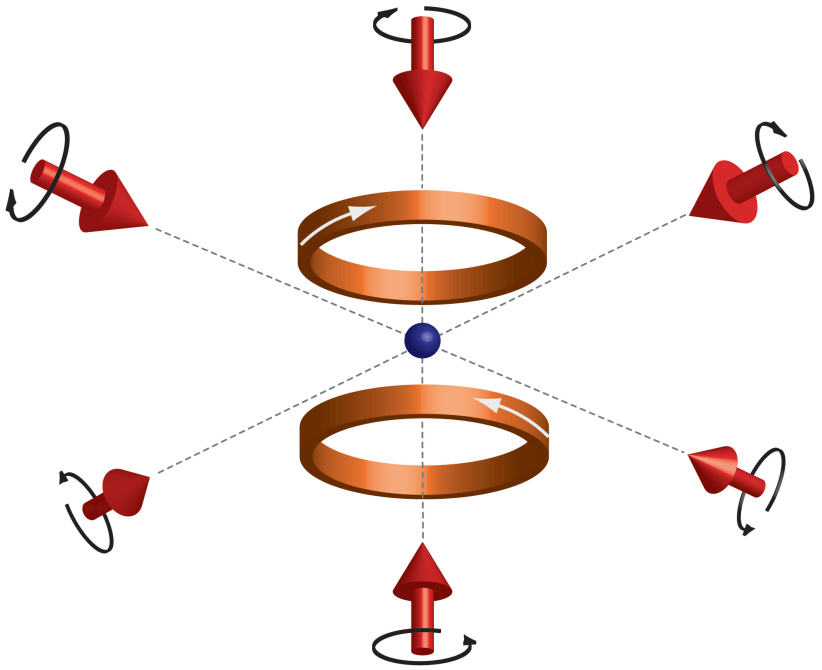

Figure 2.4: A real MOT consists of a total number of six beams in three pairs, one pair for every direction in space. The beams in a pair are counterpropagating with opposite helicities (defined in an absolute frame). The schematic figure shows the six beams and the two quadrupole coils with opposite currents, which generate the magnetic field.

The number of atoms N in a MOT after switch-on is described by a

simple rate equation:

$$\frac{\mathrm{d}N}{\mathrm{d}t} = R - N\left(\frac{1}{\tau_1} + \frac{1}{\tau_2}\right) - \chi \int n_{\mathrm{MOT}}(\vec{r})^2 \, \mathrm{d}^3 r \quad . \tag{2.25}$$

The first contribution R is the loading rate for an empty MOT. It depends on the temperature of the vapor (which is usually a constant at room temperature), the mass of the species trapped, the capture volume (the volume of space where atoms are caught), the capture velocity (the maximum speed at which atoms can be trapped[7]), and the density n_{VC} of the gas in the vapor cell. Capture volume and capture velocity are dependent on the operating parameters of the MOT: magnetic field gradient b, beam diameter, and detuning δ. The second term describes loss mechanisms: the time constant τ_1 gives the lifetime of an atom in the trap limited by collisions with atoms of the *same* species as the trapped gas, so rubidium in our case. It is inversely proportional to the density of that gas n_{VC}. The time constant τ_2 reflects the losses due to collisions with atoms of *other* species that may exist in the vapor cell. Both time constants can be summarized to a single lifetime $\tau = \frac{\tau_1 \tau_2}{\tau_1 + \tau_2}$. If the density of the trapped gas n_{VC} is much greater than the density of atoms of other species n_{al}, which is equivalent to $\tau_1 \ll \tau_2$, then τ is approximately equal to τ_1, and the influence of other species can be neglected. The third term takes losses from inner-trap collisions into account. For this reason, it is

[7] Following an estimate expression from reference [52], the capture velocity for rubidium is $\sim \ 20 \, \frac{\mathrm{m}}{\mathrm{s}}$, which means that a MOT collects the atoms from the low energy wing of the Boltzmann distribution. The most probable speed of an atom in a rubidium gas is $\sqrt{\frac{2k_{\mathrm{B}}T}{m}} = 239 \, \frac{\mathrm{m}}{\mathrm{s}}$ at $T = 25\,^{\circ}\mathrm{C}$.

proportional to the integral over the square[8] of the density *inside* the MOT n_{MOT}. The constant χ is dependent on the nature of those collisions. If the χ-term is neglected, equation 2.25 has the simple solution[9]:

$$N(t) = R\tau(1 - \mathrm{e}^{-\frac{t}{\tau}}) \quad . \tag{2.26}$$

So, the collision constant τ is also the characteristic time constant for the loading of the MOT. Figure 2.5(a) shows the fluorescence of a MOT during the loading, exhibiting the exponential form of equation 2.26 (see the remark in the footnote there). It can also be inferred from the solution that the maximum atom number in a MOT, N_{max}, is given by

$$N_{\mathrm{max}} = R\tau = R\frac{\tau_1\tau_2}{\tau_1 + \tau_2} \quad . \tag{2.27}$$

Even though R can only be estimated in theoretical considerations, this result has an important implication: for rubidium densities n_{VC} much larger then the density of other gases, so $n_{\mathrm{VC}} \gg n_{\mathrm{al}}$ or $\tau \approx \tau_1$, the lifetime τ is inversely proportional to n_{VC}, while the initial loading rate R is (always) proportional to n_{VC}. This means that the maximum total atom number does not depend on the vapor cell density n_{VC} or, using the ideal gas law $p = nk_{\mathrm{B}}T$, the background pressure p_{VC}. In fact, Monroe *et al.* [54] observed a change of N_{max} by only 30 % over a range of two orders of magnitude of pressure. For

[8] Two collision partners, therefore the square.

[9] For $n_{\mathrm{MOT}}(\vec{r}) = \text{const.} = n_{\mathrm{s}}$, the solution is the same, but the loss constant τ has to be replaced by a modified loss constant τ_{s}: $\tau \to (1/\tau + \chi n_{\mathrm{s}})^{-1}$ since $\chi \int n_{\mathrm{MOT}}(\vec{r})^2 \, \mathrm{d}^3r = \chi n_{\mathrm{s}}^2 V = \chi n_{\mathrm{s}} N$ [53]. This is an adequate approximation for MOTs far in the regime where the density in a MOT is saturated because of photon reabsorption (see below).

increasing pressure, $N_{\max}$ develops as a function of pressure p as $\frac{c\tau_2}{\tau_2+c/p}$ where c is some constant relating p and τ_1 (see also figure 2.5(b)).

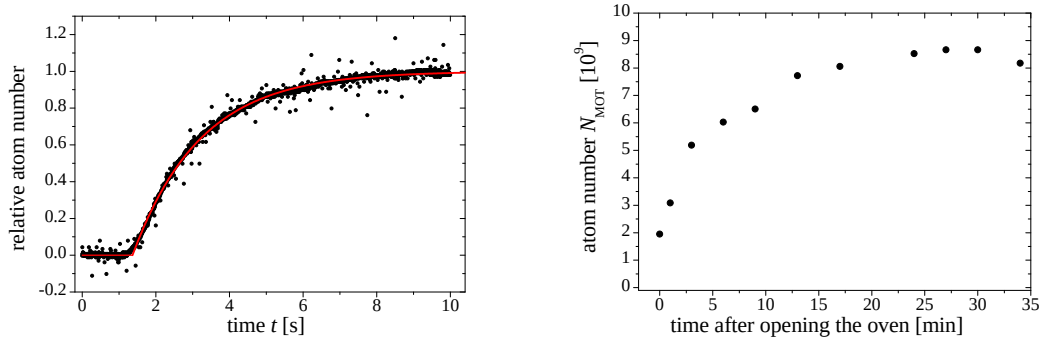

(a) MOT loading curve

(b) Pressure dependence of the MOT

Figure 2.5: MOT properties: the two figures illustrate remarks made in the text about the MOT. Figure (a) is a measurement of the fluorescence of a MOT during loading. The fluorescence is proportional to the atom number in the MOT. A function of the form in equation 2.26 is fitted to the data. This is an appropriate procedure because we operate our MOT at parameters at which it enters the density-saturated regime (see below) very soon after the start of the loading, and thus the remarks in the footnote to equation 2.26 apply. The value for the modified loss constant (defined in the aforesaid footnote) τ_s in figure (a) is 1.8 s. In the experiments (chapter 3), the MOT is usually loaded for 10 s. Figure (b) shows that from a certain background pressure on the maximal atom number in a MOT does not depend on pressure any more as explained in the text. For the measurement, the rubidium oven at a temperature of 55 °C was opened so that the Rb pressure could rise, and the maximal atom number was determined over a time of thirty-five minutes. The upper limit for the atom number in our MOT is $\sim 1\times10^{10}$ depending on different other conditions. A typical size (4σ) of a MOT is 0.6-1.0 cm.

In the introduction we emphasized the decisive role of the density n for the critical transition temperature T_c. Because of that dependence, we want to give a short qualitative discussion on the **density in a MOT**. One can principally distinguish three different regimes [55]. In the first regime, the MOT contains only few atoms and the size of the cloud is limited by

temperature. Since the repulsive force in equation 2.24 is linear, the MOT has a harmonic potential. Therefore, we can use the equipartition theorem: $^1/_2\, k_\mathrm{B}T = {}^1/_2\, \kappa_j \langle r_j \rangle$ where we want to indicate with the subscript j that the spring constant κ_j is not necessarily the same in each direction. If more atoms are added to the MOT, the size stays the same and the density increases. This is, however, only true as long as laser beam photons scattered by atoms inside the trap can leave the trap without reabsorption by other atoms inside the trap. With more and more atoms in the trap, this reabsorption becomes more likely, resulting in a repulsive force. The density in the MOT is then limited at a value where the repulsive force just balances the restoring force in equation 2.24. The numerical value of this maximum density n_s is on the order of $\sim\ 10^{11}\,\mathrm{cm}^{-3}$ for the parameters at which we operate our MOT (see chapter 3). The density has a linear dependence on the spring constant κ which is exploited in the CMOT stage of our sequence (chapter 3). A nice discussion of that effect is contained in reference [52]. The repulsive force by rescattering causes a growth of the size of the MOT if more atoms are added. Finally, the MOT extends even to regions where the absolute value of the magnetic field B is large[10]. In those regions, sub-Doppler cooling, a term which summarizes mechanisms that cool the atoms even under the Doppler cooling limit (discussion in the next section, equation 2.29), does not work. Those processes work only close to the magnetic field zero. The cloud then enters the "two-component regime", which means that two distributions are present in the MOT: one is characterized by a very low temperature, high

[10] "Large" here means that the frequency associated with B, the Larmor frequency $\omega_\mathrm{Z} = \frac{g_J m_J \mu_\mathrm{B} B}{\hbar}$, is larger than the scattering rate Γ_sc.

density, and restricted to a small region around the trap center, the other is hotter, less dense, and extends much farther. The result of a measurement that illustrates this behavior is found in chapter 3.

2.5 Optical molasses

The spontaneous force of laser light associated with the scattering rate Γ_{sc} can be used in a simple scheme to cool atoms: as in a MOT, the atoms are exposed to six red-detuned beams, two counterpropagating for each direction in space. Because of the negative detuning, an atom only experiences a large spontaneous force from a beam if it is moving toward it, for the Doppler effect shifts the atom closer to resonance in that case. In one dimension, the total force on a atom can be calculated, exactly as in the discussion for the MOT in the previous section, by subtracting the forces F_+ and F_- from the two beams with the only difference that the effective detunings $\delta_\pm$ now solely consist of the Doppler shift $\omega_{\mathrm{D},\pm} = \mp kv$. This leads to the same friction coefficient as in the discussion for the MOT:

$$\beta = \frac{8\hbar k^2 \left|\delta\right| s_0}{\Gamma(1 + s_0 + (2\delta/\Gamma)^2)^2} \quad . \tag{2.28}$$

A figurative representation of the forces from the two beams and the resulting force is shown in figure 2.6. It illustrates that the two forces combine to a force F_{Mol} that is damping for a certain region around around $v = 0$ where it can be approximated as $F = -\beta v$, thus acting like a viscous force. For this reason this technique was given the name "optical molasses" and its cooling

effect was first observed in three dimensions in 1985 [56].

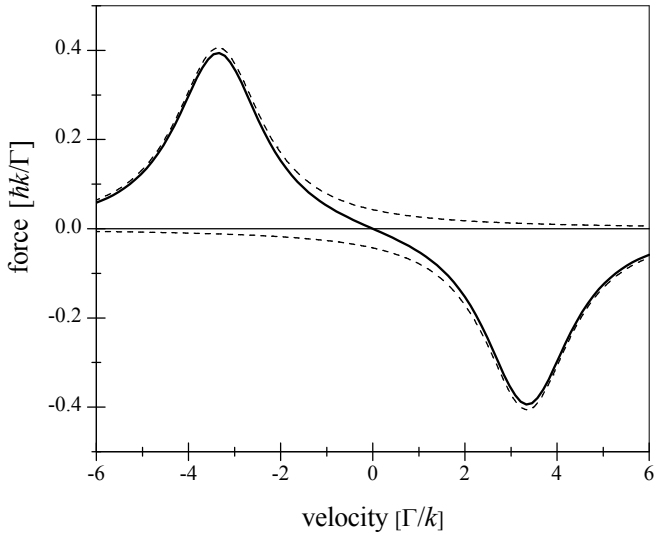

Figure 2.6: Doppler Optical molasses in one dimension: two counterpropagating red-detuned laser beams result in a damping force for velocities $v \lesssim \delta/k$. The parameters are chosen to be comparable with the situation in our experiment: $\delta = -3.5\,\Gamma$ and $s_0 = 4$.

Laser cooling cannot achieve temperatures arbitrarily close to 0 K. With the example of the one-dimensional optical molasses, we want to discuss[11] briefly the limits of laser cooling. With the friction coefficient β, the energy dissipated per unit time, the cooling rate, is given by $\frac{\mathrm{d}W_\mathrm{c}}{\mathrm{d}t} = F_\mathrm{Mol}\, v = \beta v^2$. However, there is also heating by the recoil energy $\frac{(\hbar k)^2}{2m}$ acquired by the atom during absorption and during spontaneous emission. Its rate is $\frac{\mathrm{d}W_\mathrm{h}}{\mathrm{d}t} = 2 \times 2 \times \frac{(\hbar k)^2}{2m}\Gamma_\mathrm{sc}$. The two prefactors reflect that there are two beams involved and that there are also two recoil kicks per scattering event. Cooling stops when both the heating and the cooling rate are equal: $\dot{W}_\mathrm{c} = \dot{W}_\mathrm{h}$. If one solves this

[11] The following derivation of the Doppler temperature was taken from [23].

equation for v^2 and plugs the result into $\frac{1}{2}\, k_\mathrm{B} T_\mathrm{fin} = \frac{1}{2}\, m v^2$, one recovers an expression for the final temperature T_fin as a function of δ. This expression can be minimized, yielding the result for the minimum temperature:

$$T_\mathrm{D} = \frac{\hbar \Gamma}{2 k_\mathrm{B}} \quad \text{, where } s_0 \ll 1 \text{ was assumed.} \tag{2.29}$$

This temperature limit is the so-called **Doppler temperature limit** T_D. It is the limit for a large group of cooling schemes and can be derived in a much broader context than shown here. It is also the limit for the MOT mechanism introduced in the previous section. For the D_2-line in ^{87}Rb, the cycling transition in our experiment shown in figure 2.2, it is 146 µK.

It had originally been assumed that the Doppler limit is the fundamental limit of laser cooling. The measurement of temperatures significantly below the Doppler limit [57] was, therefore, a big surprise. In the next section we are going to discuss two models of cooling below T_D.

2.6 Sub-Doppler cooling

The observation of temperatures below the Doppler limit triggered the development of a model by Dalibard and Cohen-Tannoudji that could explain the effect [58]. They identified polarization gradients in the light field as reason for the observed cooling below the Doppler limit. Polarization gradients occur when two counterpropagating beams of different polarization interfere. In a one-dimensional or two-dimensional discussion with two, respectively four interfering beams, polarization gradients can be avoided because the orientations

of the electric fields of all four beams can be chosen to be the same. In the three-dimensional case, this is no longer possible and polarization gradients are always present. We want to restrict ourselves to the usual discussion of two special cases in a one-dimensional scheme. The first case is the so-called lin $\perp$ lin-configuration where the two counterpropagating beams are both linearly polarized, but their polarization vectors are perpendicular with respect to each other. The second case is the σ^+-σ^--constellation. Both beams are circularly polarized, but with different helicities.

2.6.1 lin $\perp$ lin polarization gradient cooling

We consider two laser beams traveling along the z-axis in different directions. For simplicity, we assume equal intensities, so equal amplitudes $E_0/\sqrt{2}$ of the electric field. The beam traveling in positive direction is linearly polarized along the x-axis, the other beam along the y-axis. The electric fields of the two light fields can then be written as plane waves:

$$\begin{aligned} \vec{E}_+(z,t) &= \frac{E_0}{\sqrt{2}}\hat{\epsilon}_x \cos(kz-\omega t) \\ \vec{E}_-(z,t) &= \frac{E_0}{\sqrt{2}}\hat{\epsilon}_y \cos(kz+\omega t) \quad , \end{aligned} \tag{2.30}$$

where $\hat{\epsilon}_x$ and $\hat{\epsilon}_y$ are the unit vectors in x and y-direction respectively. Superposition of the two beams gives the total electric field $\vec{E}(z,t)$:

$$\vec{E}(z,t) = E_0\left(\frac{1}{\sqrt{2}}(\hat{\epsilon}_x+\hat{\epsilon}_y)\cos(kz)\cos(\omega t) + \frac{1}{\sqrt{2}}(\hat{\epsilon}_x-\hat{\epsilon}_y)\sin(kz)\sin(\omega t)\right) \quad . \tag{2.31}$$

This result implies the existence of polarization gradients in the electric field: for $z = 0$, the light is polarized along the unit vector $\frac{1}{\sqrt{2}}(\hat{\epsilon}_x + \hat{\epsilon}_y)$, which we shall call the 45 °-direction. For $z = \lambda/8$, the light is right-circularly (σ^-) polarized. For $\lambda/4$ the light is again linearly polarized, but in the -45 °-direction. For $3\lambda/8$, the light is left-circularly polarized, so σ^+-polarized, for $z = \lambda/2$, the polarization is again linear in 45 °-direction. Between these values it has elliptical polarization. The polarization thus changes within half a wavelength, which is illustrated in figure A.1 (d) of appendix A.

The changing polarization is reflected in changing coupling strengths for different magnetic substates in the ground level. Again for simplicity, we want to assume that there are only two of them: $m_g = \pm 1/2$. Following the discussion in the section on the two-level atom, different coupling strengths are equivalent to differing lightshifts. An atom that travels along the propagation direction of the light beams is thus exposed to a potential rising and falling with a period of $\lambda/2$. That means, however, that it permanently converts kinetic energy into potential energy and vice-versa. The key mechanism for the cooling effect is now **optical pumping** between the two substates, for potential hills of one substate always coincide with potential valleys of the other: if the atom is pumped after it has reached the top of a potential hill, potential energy is not reconverted to kinetic energy. Instead, the atom finds itself in a valley and has to climb a potential hill again. The difference in energy has been given away to the light field. Hence, the atom always has to climb the hills, but can never descend them and thus dissipates energy. Because of the analogy of that situation with the fate of a famous figure of Greek mythology, this

cooling mechanism has been called **Sisyphus cooling**. The interested reader finds some illustration along with more a detailed explanation in appendix A.

Similarly as in the remarks on optical molasses, one can derive a friction coefficient for Sisyphus cooling. It is larger than the one for optical molasses, but its validity is restricted to a smaller velocity range. Thus, the scheme can cool atoms pre-cooled by ordinary Doppler molasses to even lower temperatures than the Doppler temperature T_{D}, which we identified as the cooling limit in section 2.5.

2.6.2 σ^+-σ^- polarization gradient cooling

In the σ^+-σ^--constellation the two beams can be written as:

$$\begin{aligned} \vec{E}_+(z,t) &= \frac{E_0}{2}\left(\hat{\epsilon}_x \cos(kz-\omega t) + \hat{\epsilon}_y \sin(kz-\omega t)\right) \\ \vec{E}_-(z,t) &= \frac{E_0}{2}\left(\hat{\epsilon}_x \cos(kz+\omega t) + \hat{\epsilon}_y \sin(kz+\omega t)\right) \quad . \end{aligned} \tag{2.32}$$

The total field is found to be:

$$\vec{E}(z,t) = E_0 \cos(\omega t)\left(\hat{\epsilon}_x \cos(kz) + \hat{\epsilon}_y \sin(kz)\right) \quad . \tag{2.33}$$

This field is always linearly polarized, but the direction of the polarization performs a complete rotation within half a wavelength, which is shown in figure 2.7. This rotation also evokes a cooling effect which does, however, not allow a nice description as in the lin $\perp$ lin-case. We want to give here only a very qualitative explanation. We assume an atom with ground state $J = 1$,

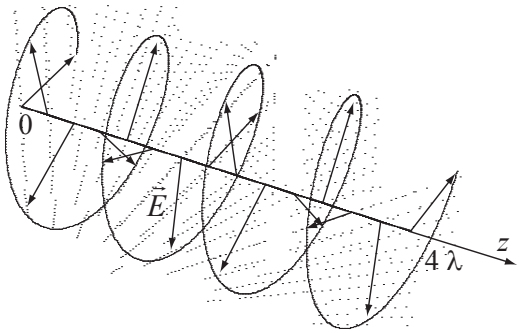

Figure 2.7: σ^+-σ^--polarization gradient cooling: in the σ^+-σ^--configuration the polarization is always linear, but rotates with a period of $\lambda/2$. For an atom in motion, this effects preferred scattering from one beam compared to the other, which - for negative detuning - slows the atom down.

so three magnetic sublevels $m_g = 0, \pm 1$, and $J = 2$ in the excited state. For atoms at rest in linearly polarized light, the population of the $m_g = -1$ and the $m_g = +1$-state are the same. The motion of the atom in a field with changing direction of polarization, however, gives rise to an additional term in the Hamiltonian describing the response to the rapidly changing polarization. This new Hamiltonian has different eigenstates than the Hamiltonian for the atom at rest. The relevant effect of the additional term in the Hamiltonian is that it perturbs the populations of the old eigenstates: the populations of the $m_g = -1$ and the $m_g = +1$-state are no longer balanced. Because transitions strengths also differ ($m_g = -1 \rightarrow m_e = -2$ from σ^- e. g. is stronger than $m_g = -1 \rightarrow m_e = 0$ from σ^+), the imbalance in the population induced by motion eventually causes a preferred scattering from one beam compared to the other. For red detuning, the effect of this preferred scattering is such that it slows the atoms down, regardless of their direction of motion. The complete description is a nice exercise in perturbation theory [58].

Although both mechanisms (the lin $\perp$ lin and the σ^+-σ^--scheme) described above work quite differently, both rely on polarization gradients, and their relevant effect is the same: temperatures well below the Doppler limit are attainable even in ordinary optical molasses. The final temperature that can be reached by the processes described scales with $|\delta|^{-1}$. For this reason, one increases the red detuning during a molasses step; one starts with detunings suitable for Doppler molasses and then enforces the polarization gradient cooling by detuning the laser further from resonance. Sub-Doppler cooling exists both in optical molasses and in the magneto-optical trap. In the MOT it is, however, restricted to a small region around the zero of the magnetic field. For higher magnetic fields, other effects (e. g. velocity-selective resonance [59]), which we will not discuss here, become important and the benefits from sub-Doppler cooling disappear. The three-dimensional case, so e. g. the optical molasses and the MOT in our experiment, can never be a pure case of the two schemes presented above and is little understood. The experimental results, though, confirm that polarization gradient cooling also works in three dimensions: temperatures as low as 1.1 µK have been observed [54].

2.7 Magnetic trapping

After pre-cooling with laser means, magnetic trapping provides the confinement necessary in a BEC experiment for two reasons: evaporative cooling needs some form of containment for the atoms so that they do not drift apart and to generate the necessary density for a quick rethermalization after a cool-

ing step. As the atoms are cooled, the trap also compresses the atom cloud and increases the density that is critical for the BEC transition (equation 1.6).

Ions can be trapped only with a.c.-electric fields because trapping of monopoles with static fields is not possible as stated in Earnshaw's theorem. Neutral atoms, however, can be trapped by use of the interaction V_{Z} of their magnetic dipole moment $\vec{\mu}$ with a static magnetic field:

$$V_{\mathrm{Z}} = -\vec{B} \cdot \vec{\mu} \quad . \tag{2.34}$$

If we assume that the magnetic field is oriented along the z-axis, $\vec{B} = B\hat{\epsilon}_z$, and that the magnetic moment is also quantized along $\hat{\epsilon}_z$, the quantum mechanical operator for this part of the Hamiltonian is:

$$\mathcal{H}_{\mathrm{Z}} = g_J \frac{\mu_{\mathrm{B}}}{\hbar} \vec{B} \cdot \vec{J} = g_J \mu_{\mathrm{B}} m_J B \quad , \tag{2.35}$$

where $\vec{J}$ is the total angular momentum and g_J is the g-factor for $\vec{J}$. This result can generally just be written as $g_J \mu_{\mathrm{B}} m_J B$ where $B := |\vec{B}|$ is the magnetic field strength (regardless of its direction) if the magnetic moment $\vec{\mu}$ has enough time to adjust to a (spatially or timely) changing field. The criterion for this "**adiabatic following**" is that the Larmor frequency $\omega_{\mathrm{Z}} = g_J \mu_{\mathrm{B}} m_J B/\hbar$ is larger than the rate at which the magnetic field changes:

$$\omega_{\mathrm{Z}} \gg \frac{1}{B} \left| \frac{\mathrm{d}\vec{B}}{\mathrm{d}t} \right| \quad . \tag{2.36}$$

Except near field zeros, this condition is generally fulfilled in neutral atom

traps. The right side of equation 2.35 represents energy shifts of the atom level structure by the magnetic field, the familiar Zeeman effect. But we can also think about it as an effective conservative potential $V_{\mathrm{Z}}(\vec{r})$, which is especially useful if the magnetic field spatially varies $B = B(\vec{r})$. From this perspective, atoms can be trapped in two cases: a local minimum of the magnetic field means a potential minimum of V_{Z} and thus confinement for atoms with $g_J m_J > 0$. Those are called low-field-seekers. A local maximum of the magnetic field would trap, in contrast, atoms with $g_J m_J < 0$ (which are consequently called high-field-seekers) if it existed: it was shown by Wing [60] that in a region without currents or charges the magnitude of a magnetic (or electric) field cannot have a local maximum. Local minima, however, do exist[12]. That means that only **low-field seekers** can be trapped.

The magnetic dipole interaction is much weaker than the interaction energies of ions in electric fields. If the interaction energy of the order $\mu_{\mathrm{B}} B$ with realistic laboratory magnetic fields of $B \sim 0.1\text{-}1\,\mathrm{T}$ is compared with the thermal energy $k_{\mathrm{B}} T$, then atoms with $T = 100\text{-}1000\,\mathrm{mK}$ can be trapped. Often, this temperature is even much lower. It is common to specify this **trap depth** in temperature units. This temperature range implies the necessity of some sort of pre-cooling, e. g. laser cooling. It also explains the strict limitations on background pressure that we have noted in the introduction: an atom from the background gas with $T = 300\,\mathrm{K}$ can easily transfer enough momentum to a trapped atom in a collision to kick it (and many more) out of the trap. The

[12]Wing's theorem is a nice curiosity from a historical perspective: although its proof just needs Maxwell's theory of electromagnetism which had been known since the 1880s, it took more than a hundred years for someone to discover it – or to bother to write down [61].

average lifetime of a trapped atom in a vapor cell with $p \sim 1 \times 10^{-9}$ mbar is on the order of a few seconds.

The simplest magnetic field geometry with a local field minimum is the **quadrupole field**, which is also the configuration employed in this experiment for magnetic trapping. This field can be generated by two identical circular coils arranged coaxially (along the z-axis). The currents in the coils have opposite directions. The configuration is, therefore, called anti-Helmholtz. The field produced by the coils clearly has a vanishing magnitude on the axis in the middle between the two coils. The magnetic field can be approximated to first order just by two simple arguments: if we put the origin at the field zero, the fields in x and y-direction must be the same because of axial symmetry. They are also radially orientated and have no z-components, so $\vec{B}(x,0,0) = (b_x x, 0, 0)$ and $\vec{B}(0,y,0) = (0, b_y y, 0)$ with $b_x = \frac{\partial B}{\partial x}\Big|_{\vec{r}=(0,0,0)} = b_y = \frac{\partial B}{\partial y}\Big|_{\vec{r}=(0,0,0)}$. The magnetic field to lowest non-vanishing order is then $\vec{B}(\vec{r}) = (b_x x, b_x y, b_z z)$. Because of the Maxwell equation $\vec{\nabla} \cdot \vec{B} = 0$, it follows:

$$b_z := \frac{\partial B}{\partial z}\bigg|_{\vec{r}=(0,0,0)} = -2b_x = -2b_y \quad . \tag{2.37}$$

In the notation of this thesis, *the* **magnetic field gradient** is the gradient in z-direction b_z. It will sometimes just be abbreviated with $b := b_z$. Its numerical value per current in the coils I for our setup was measured to be $\frac{b}{I} = 0.88 \, \frac{\mathrm{G}}{\mathrm{cm\,A}}$ [39]. The magnetic field of the quadrupole configuration to lowest order is

thus:

$$\vec{B}(\vec{r}) = \frac{b}{2}\begin{pmatrix} -x \\ -y \\ 2z \end{pmatrix} \quad . \tag{2.38}$$

Its magnitude (strength) is

$$B(\vec{r}) := \left|\vec{B}(\vec{r})\right| = \frac{b}{2}\sqrt{x^2+y^2+4z^2} \quad . \tag{2.39}$$

Respecting the presence of gravity in the experiments, the full potential is[13]:

$$V_{\mathrm{Z}}(\vec{r}) = mgz + \frac{g_J m_J \mu_{\mathrm{B}} b}{2}\sqrt{x^2+y^2+4z^2} \tag{2.40}$$

The density $n(x,y,z)$ of a thermal atom cloud in equilibrium as a function of position in a quadrupole trap respecting the influence of gravity is given by a barometric height formula:

$$n(\vec{r}) = n_0 \mathrm{e}^{-\frac{mgz}{k_{\mathrm{B}}T}} \mathrm{e}^{-\frac{g_J m_J \mu_{\mathrm{B}} b}{2k_{\mathrm{B}}T}\sqrt{x^2+y^2+4z^2}} \quad . \tag{2.41}$$

Figure 2.7 shows a calculated contour plot of the magnetic field strength and the plots of the calculated radial and axial fields in a quadrupole trap, which is idealized as two current loops.

For later discussion, it is helpful to derive the scaling laws for temperature and volume in an **adiabatic compression** of the potential (neglecting the influence of gravity). We assume a compression by a factor η of the potential, so $b \rightarrow \eta b$. The temperature may scale with a factor ξ:

[13]It is assumed that the strong axis z of the quadrupole field coincides with the direction of gravity as in our experiment.

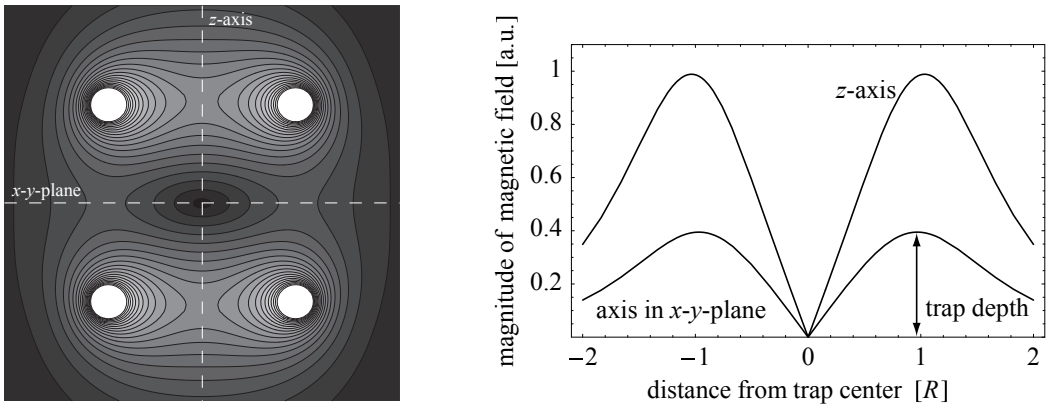

(a) contour plot

(b) field strength along axes

Figure 2.8: Field of a quadrupole trap, idealized as two current loops. The distance between the coils is chosen to be equal to the diameter ($2R$) of the coils. Figure (a) shows a contour plot of the magnetic field strength. The coil axis is located at the center of the plane. The field zero in the center can be seen as well as the divergences where the coils intersect the plane. Figure (b) shows a plot of the magnetic field along the z-axis and along an arbitrary axis in the x-y-plane. The field gradient along the z-axis close to the field zero is twice as large as in the x-y-plane.

$T \to \xi T$. The new density distribution with correct normalization is then: $n'(\vec{r}) = \left(\frac{\eta}{\xi}\right)^3 n_0 \mathrm{e}^{-\frac{g_J m_J \mu_\mathrm{B} \eta b}{2 k_\mathrm{B} \xi T}\sqrt{x^2+y^2+4z^2}}$. The new average distance from the center in the cloud is given by $\langle r' \rangle = \int r n'(\vec{r})\,\mathrm{d}^3 r = \frac{\xi}{\eta}\int r n(\vec{r})\,\mathrm{d}^3 r = \frac{\xi}{\eta}\langle r \rangle$. So, we have $V' \propto \langle r' \rangle^3 \propto \left(\frac{\xi}{\eta}\right)^3$. Using the adiabatic condition for a monatomic gas

$$TV^{2/3} = \text{const.} \quad , \tag{2.42}$$

we find:

$$\xi = \eta^{2/3} \quad \Rightarrow \qquad T \propto \eta^{2/3}, \qquad \langle r \rangle \propto \eta^{-1/3}, \qquad V \propto \eta^{-1} \quad . \tag{2.43}$$

Chapter 3

Methods, experiments, and results

3.1 Imaging

Nearly all information about ultracold atomic clouds and their various properties can be obtained by analysis of optical images. For the results of this thesis, two optical imaging methods were employed, which are presented in the following paragraphs.

3.1.1 Absorption imaging

One technique to image an ultracold atom cloud is absorption imaging. Speaking in simple terms, one analyzes the shadow of the atoms which they cast in an imaging beam. The darker the shadow is, the more atoms must have been contained in the cloud to absorb and scatter the light of the imaging beam. The geometry of the absorption beam in our setup is shown in figure 2.1: the beam is delivered from the laser system [39] through an optical fiber, enters the vacuum system through a window, propagates through the differential pump-

ing tube, and hits the cloud in the vapor cell. The beam is turned on and off using a combination of a mechanical shutter (slow, reaction time: 4 ms) and an acousto-optical modulator (AOM, fast, reaction time: 5 µs) inside the laser box. The exposure timing is defined by the AOM. The shutter completely extinguishes any leakage of light through the AOM from hitting the cloud during the preparation sequence. The $\lambda/4$-waveplate in front of the entrance window allows us to make the light circularly polarized if desired. The light then passes through a window at the front of the "square chamber" and runs through a differential pumping tube to the vapor cell, where it hits the cloud. It leaves the vacuum system again and is then scaled down with a telescope and directed onto the chip of the camera. Figure 3.1 shows a schematic for the beam path behind the vacuum system. The distances are chosen such that both absorption and fluorescence imaging (see section 3.1.2) can be done with the same optical setup.

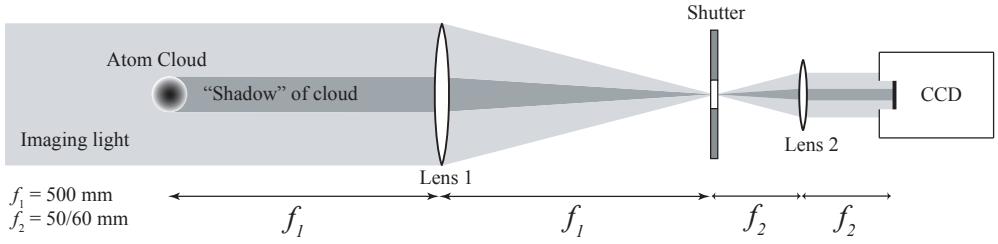

Figure 3.1: Absorption imaging: the image shows the beam path in absorption imaging. The second lens (initially $f_2 = 50$ mm) was later replaced by a lens with $f_2 = 60$ mm. The magnification is thus 1:10 or 1:8.3 respectively. The shutter in this picture is not necessary for absorption imaging, but needed for fluorescence measurements.

The CCD-chip is typically exposed for 100 µs to the imaging light by

flashing on the AOM[1]. In order to obtain quantitative information from absorption images and eliminate systematic errors, three pictures are acquired for every measurement, each with the same exposure time: the first, B^{atoms}, with the atom cloud, the second one, B^{light}, as normalization reference without the atoms, but with the imaging beam turned on. The last picture, B^{dark}, is taken without imaging light and serves to subtract the effects of stray light sources and the dark current of the camera. The imaging software automatically creates a new image $(B^{atoms} - B^{dark})/(B^{light} - B^{dark})$ from the three images.

With a short calculation, we now show how the three images can give information about the atom number in a cloud. In an absorbing medium the intensity of light decreases with Beer's law as $dI = -\alpha I dx$ where the Beer absorption coefficient α is proportional to the imaginary part n_I of the index of refraction of the medium: $\alpha = 2kn_I$. For a dilute atom cloud the energy scattered per volume is $\hbar\omega n(x)\Gamma_{sc}$, where $n(x)$ is the density of atoms, Γ_{sc} is the scattering rate (from equation 2.15), and $\hbar\omega$ is the energy of one scattered photon. The scattering rate is related to the scattering cross section σ_{sc} through $\hbar\omega\Gamma_{sc} = I\sigma_{sc}$. We get:

$$dI = -\alpha I dx = -\hbar\omega n(x)\Gamma_{sc} dx = -\sigma_{sc} n(x) I(x) dx. \tag{3.1}$$

[1]The chip collects, however, light for a much longer duration because the internal shutter of the camera needs $\sim$60-100 ms to open and close.

With $n(x) = \mathrm{d}N/\mathrm{d}V$, taking $\mathrm{d}V = A\mathrm{d}x$, we can transpose and integrate:

$$\mathrm{d}N = -\frac{1}{\sigma_{\mathrm{sc}} I}\frac{\mathrm{d}I}{\mathrm{d}x}\mathrm{d}V = -\frac{A}{\sigma_{\mathrm{sc}} I}\frac{\mathrm{d}I}{\mathrm{d}x}\mathrm{d}x = -\frac{A}{\sigma_{\mathrm{sc}}}\frac{\mathrm{d}I}{I} \quad \Rightarrow \quad N = -\frac{A}{\sigma_{\mathrm{sc}}}\ln\left(\frac{I_{\mathrm{trans}}}{I_0}\right). \tag{3.2}$$

The assumption $\mathrm{d}V = A\mathrm{d}x$ is justified as long as A is small enough so that the density does not significantly change over the size of A. Equation 3.2 gives us a formula with which the atom number in the cloud can be extracted from the absorption images:

$$N_{\mathrm{atom}} = -\frac{A_{\mathrm{pixel}}}{\sigma_{\mathrm{sc}}}\sum_{i,j}\ln\left(\frac{\mathrm{B}_{i,j}^{\mathrm{atoms}} - \mathrm{B}_{i,j}^{\mathrm{dark}}}{\mathrm{B}_{i,j}^{\mathrm{light}} - \mathrm{B}_{i,j}^{\mathrm{dark}}}\right) \quad , \tag{3.3}$$

where A_{pixel} is the length calibration ([m^2/pixel]) and the sum runs over all rows and columns of the images. It can be seen from the result that this method is independent of the intensity (as long as the intensity is well under the saturation intensity I_{sat}), though care must be taken to control the polarization, which affects σ_{sc}. For this reason, the $\lambda/4$-plate is placed directly in front of the vacuum apparatus.

3.1.2 Fluorescence imaging

Observing the fluorescence of an atom cloud exposed to near-resonant light is another way of imaging it. The cloud is exposed to the MOT beams (both the cycling and repumping lasers) for a duration of 1 ms during which the scattered light is collected with the CCD camera. We typically use a detuning of $\delta = -3.5\,\Gamma$ and the maximally available power in the MOT beams. Figure

3.2 shows schematically the optics that are used to image the cloud on the CCD-Chip. The objective lens (L1) is placed directly behind a window of

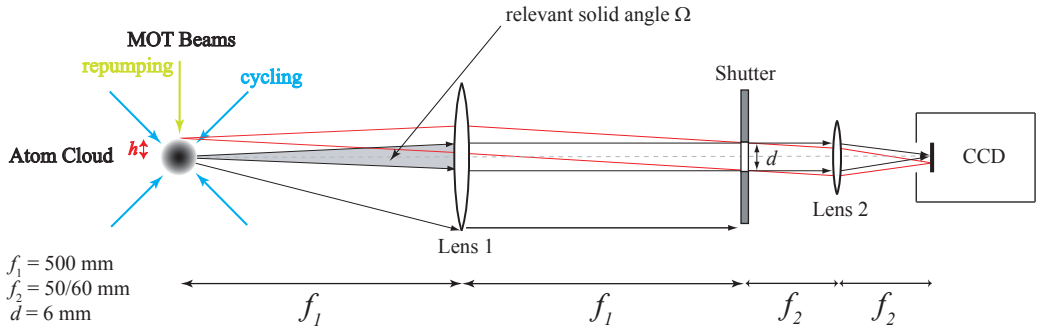

Figure 3.2: Fluorescence imaging: the figure shows the beam path in fluorescence imaging. A shutter controls the exposure time because the built-in shutter of the camera does not work reliably.

the vacuum apparatus. It has an diameter of 2″ and its focal length is $f_1 = 500\,\text{mm}$. The ocular was exchanged during the measurements for this thesis. Originally, it had a diameter of 1″ and a focal length $f_2 = 50\,\text{mm}$, but it was replaced by a 2″-lens with $f_2 = 60\,\text{mm}$. Since we use the same setup also for absorption imaging, the optical pathlength between the two lenses is exactly the sum of both focal lengths. The objective lens itself is $f_1 = 500\,\text{mm}$ away from the object, namely the cloud in the magneto-optical trap. In the actual setup, a mirror is located between lens 1 and lens 2 for practical reasons (lack of space, see figure 2.1).

It was checked that vignetting [62], a common imaging problem for off-axis objects, is not a problem in our setup. For a detailed discussion see appendix B.1.

The number of photons scattered per time t by a cloud with N_{atoms} atoms

is $N_{\mathrm{atoms}}\Gamma_{\mathrm{sc}}t$, where Γ_{sc} is the atomic scattering rate from equation 2.15. The atom number N_{atoms} can thus be extracted from fluorescence images according to

$$N_{\mathrm{atoms}} = \frac{4\pi}{\Omega}\frac{N_{\mathrm{counts}}\,QE}{c_{\mathrm{e}^-}\,\Gamma_{\mathrm{sc}}\,t_{\mathrm{exp}}\,0.96^k} \quad , \tag{3.4}$$

where Ω is the solid angle effectively contributing to the image, N_{counts} is the number of counts from the CCD that constitute the image of the cloud, QE (0.75 for the camera used) is the quantum efficiency of the camera chip, c_{e^-} ($2^{16}/100000$) is the number of counts that are registered per photo electron, t_{exp} the exposure time of the chip to the fluorescent cloud (usually 1 ms), and the factor 0.96^k takes into account losses by reflection on glass surfaces with k being the number of surfaces without anti-reflection coating ($k = 2$). From figure 3.2, it can be inferred that the relevant solid angle Ω is determined by the diameter $d = 6$ mm of the shutter and the focal length f_1, so $\Omega = 4\pi\frac{\pi(d/2)^2}{4\pi f_1^2}$.

Both the absorption and fluorescence images are processed with the computer algebra program Mathematica. The number of counts in a fluorescence image is calculated after subtraction of a suitable background picture B^0 from the image B to obtain a corrected image where potential counts from stray light have been eliminated. Two methods exist to extract N_{counts} then from the corrected image: either all counts of the whole image array are simply added up, so $N_{\mathrm{counts}} = \sum_{i,j}\mathrm{B}_{i,j} - \mathrm{B}^0_{i,j}$. Or alternatively, a Mathematica routine determines the 1-D column density $n(z)$ and fits a model Gaussian distribution ($n(z) = a\mathrm{e}^{-z^2/(2\sigma^2)}$) to it, whose parameters give the count number: $N_{\mathrm{counts}} = a\sqrt{2\pi}\sigma$. Summation works better for large clouds where it is more accurate because in most cases a Gaussian function is only an approximation

to the real shape of the cloud (e. g. an atom cloud in the linear potential of a quadrupole magnetic trap is *not* a Gaussian). The strength of the second method is that it is less sensitive to noise by stray light that would be counted by the summation method. A particular source of stray light, which cannot be removed by subtraction of a background image, are reflections from the differential pumping tube connecting the vapor cell and the "square chamber". This reflects so much of stray light from the fluorescing atom cloud that it can be seen on all fluorescence measurements. Thus, the integration method is usually applied only for small clouds.

3.1.3 Choice of imaging method

Principally, absorption imaging is superior to fluorescence imaging because it provides a much better signal to noise ratio. Particularly for small atom numbers, it is more accurate. It is also not dependent on intensity while quantitative analysis of fluorescence images is. On the other hand, absorption imaging needs a clear quantization axis as it depends on σ_{sc}, so all residual magnetic fields must be eliminated and a bias field along the imaging axis must be applied. Then, σ^+ light, e. g., can be chosen, for which σ_{sc} is well-defined. For fluorescence imaging, in contrast, it is sufficient to assume the saturation intensity for unpolarized light, $I_{\mathrm{sat,unpol}} = 4.1\,\frac{\mathrm{mW}}{\mathrm{cm}^2}$ for the cycling transition in ^{87}Rb. Fluorescence imaging can be only performed in the vapor cell, where the MOT beams can be used as light source.

For all quantitative analysis in this thesis, fluorescence imaging was chosen for two reasons: 1) It allowed longer times of flight for temperature mea-

surements (see next section). For absorption imaging the cross sectional area of the differential pumping tube limits the observable region for an atom cloud. The maximum time of flight for a cloud with diameter 6 mm is then ~ 20 ms. In fluorescence imaging, the observable region is defined by the first imaging lens, for which it was calculated that flight times up to 56 ms are possible with our setup (see appendix B.1). 2) It was discovered that the frequency of the cycling laser had a considerable jitter, even when locked. This jitter influences the detected atom number in absorption images much more than in fluorescence images due to the short exposure time and the low saturation (see appendix B.2). Because of these two reasons and knowing that the atom numbers in MOT and MT are still large enough (in contrast to the shrinking clouds during an evaporation stage), fluorescence imaging was chosen as primary imaging method. For analysis of clouds in the science cell, where no light source for fluorescence imaging is available, we will change to absorption imaging again.

3.2 Determination of temperatures

In order to determine the temperature of a cooled atom cloud, we observe its thermal expansion after release from the trap as a function of time. For this, we take a sequence of images of clouds that have been prepared under identical conditions and have freely expanded for a varying time t. As all measurements described in this thesis have been taken for thermal clouds well above T_c, we can treat the cloud classically. In this case, the expansion of a

Gaussian thermal cloud with one-dimensional initial density profile for $t = 0$

$$n(x, t = 0) = \frac{n_0}{\sqrt{2\pi}\sigma_{x,0}} \exp\left(-\frac{x^2}{2\sigma_{x,0}^2}\right) \quad , \tag{3.5}$$

where n_0 is the peak density and $\sigma_{x,0}$ the $1/\sqrt{\mathrm{e}}$-width, can be expressed as:

$$\begin{aligned} n(x,t) &= \frac{n_0}{\sqrt{2\pi}\sigma_{x,0}} \frac{1}{\sqrt{2\pi m k_\mathrm{B} T_x}} \iint \exp\left(-\frac{x_0^2}{2\sigma_{x,0}^2}\right) \exp\left(-\frac{p^2}{2mk_\mathrm{B}T_x}\right) \\ &\qquad \delta\left(x - x_0 - \frac{pt}{m}\right) \mathrm{d}p \, \mathrm{d}x_0 \end{aligned} \tag{3.6}$$

where δ is the Dirac δ-distribution, m the mass of the gas atoms, p the momentum, and $1/\sqrt{2\pi m k_\mathrm{B} T_x} \exp\left[-p^2/(2mk_\mathrm{B}T_x)\right]$ the momentum distribution at temperature T_x. The double integral represents a convolution of the initial density profile with the momentum distribution. It has a descriptive meaning: the two integrals express the expansion of every point x_0 due to the thermal velocity distribution at that point, which yields after integration the new density distribution:

$$n(x,t) = \frac{1}{\sqrt{2\pi}\sqrt{\sigma_{x,0}^2 + \frac{k_\mathrm{B}T_x}{m}t^2}} \exp\left[-\frac{x^2}{2\left(\sigma_{x,0}^2 + \frac{k_\mathrm{B}T_x}{m}t^2\right)}\right] \tag{3.7}$$

From this expression, the $1/\sqrt{\mathrm{e}}$-width after an expansion time t is clearly:

$$\sigma_x(t) = \sqrt{\sigma_{x,0}^2 + \frac{k_\mathrm{B}T_x}{m}t^2} \quad , \tag{3.8}$$

The temperature now is simply obtained by fitting the model function 3.8 to the data (after generating a 1-D column density). This proves to be a robust

method, and we usually do not need more than four data points to obtain trustable results. This discussion respected only one dimension, but can be immediately expanded to three dimensions because of the separability of the involved integrals. It is important to note that the temperature T_x was introduced as a parameter describing the one-dimensional velocity distribution in the x-direction. Under the condition of thermal equilibrium (which can be reached in a magnetic trap), the value for T_j should be the same in each direction $j \in \{x, y, z\}$. However, for many experiments a full rethermalization before detection is not possible. Therefore, we often determine two "temperatures" T_y and T_z (see section 3.7.2). Practically, we can calculate the column densities only along the y or the z-axis. Expansion along the x-direction is not observable as it is the optical axis of the imaging optics; we thus detect only the projection of the cloud along this axis.

3.3 Magneto-optical trap

The collection of the atoms in the magneto-optical trap (MOT) is the first stage of any preparation sequence in our experiment. In various measurements done prior to the time the author spent in the research group, the MOT was optimized and characterized [39, 63]. It was found to work best at a magnetic field gradient[2] of $\partial B/\partial z = 8.8\,\mathrm{G/cm}$, and a detuning of the pumping lasers of $\delta_{\mathrm{MOT}} = -3.5\,\Gamma$. As discussed in [64], there is an optimal set of these

[2] At that time, the quadrupole coils were not the same as in the later experiments performed by the author: this field gradient now corresponds to a coil current of $I_{\mathrm{MOT}} = 10\,\mathrm{A}$ while at the time of the measurements a current of 12 A was needed.

parameters for every possible laser intensity and diameter of the trapping beams. Increasing the field gradient means reducing the effective capture range of a MOT. This effect is balanced by detuning the cycling frequency further from resonance. Our values are roughly consistent with those reported in literature ([38, 54, 64]).

Figure 3.3(c) shows the dependence of the maximum atom number collected in the MOT on detuning for a magnetic field gradient of $\partial B/\partial z = 7.0\,\mathrm{G/cm}$. As shown in figure 3.3(b), the shape of the cloud is a two-component distribution, particularly for larger detunings: a central peak with a much higher atom density arises over a broader, less dense distribution (figure 3.3(b)). This fact was predicted in [52] and first observed in [55, 65]. As explained in chapter 2, it is interpreted as manifestation of polarization gradient cooling in the center of a MOT: for the small magnetic fields in the center of the trap, sub-Doppler mechanisms are viable while they are impaired for the higher field strengths in the outskirts of the cloud. We could also confirm the results in [55, 65] that for increasing field gradients the total number of atoms is approximately constant while the number in the central distribution declines reaching $\sim 50\,\%$ of the total atom number at a gradient of $20\,\mathrm{G/cm}$ (figure 3.3(d)). Since the atoms contained in the central distribution are much colder and their density is higher, optimization includes maximization of the size of this part of the MOT. This explains the choice of our MOT-parameters: for a detuning of $-3.5\,\Gamma$ and a field gradient of $8.8\,\mathrm{G/cm}$, more than $90\,\%$ of the atoms were found to be in the center of the cloud, containing up to 1×10^{10} atoms (figure 3.3(d)).

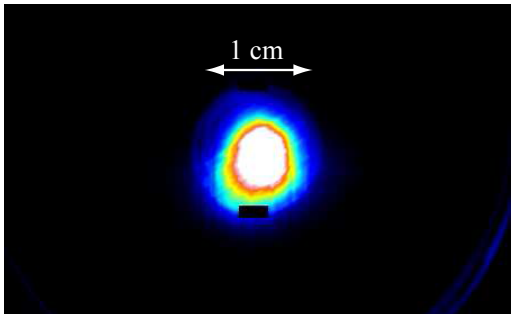

(a) Fluorescence image of a MOT

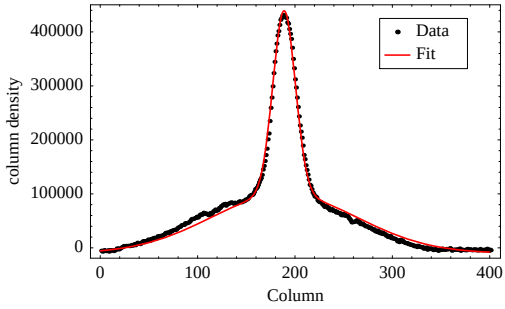

(b) Two-component regime

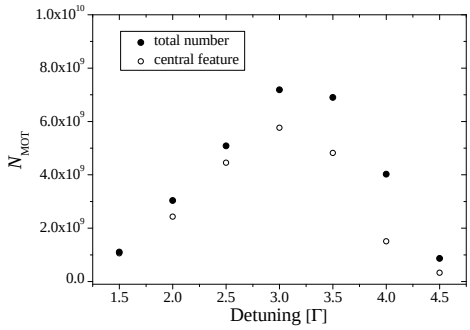

(c) Dependence on detuning

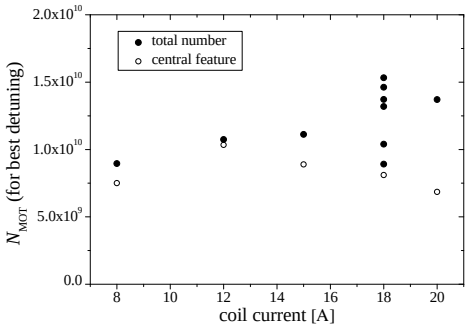

(d) Dependence on field gradient

Figure 3.3: Optimization of MOT loading parameters: figure (a) shows a fluorescence image of the magneto-optical trap. The atom number for this image is 1.2×10^{10}. The cut-outs that are visible are necessary because of reflections from pieces of the vacuum apparatus. The error caused by this correction is negligible. Figure (b) is a graph of the one-dimensional column density in a MOT for a field gradient of 7.0 G/cm. It shows the typical two-component distribution in a MOT. Figure (c) shows the atom number in the MOT for $I_{\mathrm{MOT}} = 8$ A and various detunings. The filled dots in figure 3.3(c) give the total atom number in the MOT while the circled ones represent the size of the central peak. Figure (d) shows the atom number in a MOT for various field gradients where the result for the best detuning was taken for each field gradient from measurements as in figure (c). The data in figures (b)-(d) was taken from references [39, 63]. At that time, the magnetic field calibration was not the same as in the later measurements (different quadrupole coils).

3.3.1 Light induced atomic desorption

Klempt *et al.* [66] showed a multiple increase in the atom number of a magneto-optical vapor cell trap by light-induced atom desorption (LIAD) of trappable atoms from the walls of the vacuum chamber. This effect is analog to the well-known photoelectric effect: atoms that have deposited to the inside surfaces of the vacuum chamber can be dissolved by shining ultra-violet light from outside onto the chamber. This causes a sudden increase of the background pressure in the vapor cell and consequently raises the maximum atom number in the MOT $N_{\max}$ following equation 2.27, unless the background pressure p is in the regime where the MOT atom number does not depend on pressure anymore and has saturated. When the light is turned off, the atoms stick to the walls again and the pressure drops quickly. This phenomenon offers the opportunity to artificially raise the pressure during the loading phase of the MOT and trap a high atom number by turning on a UV-source. The UV light is then turned off while the MOT beams stay switched on. This allows the background pressure to drop again. The pressure falls much faster than the MOT atom number reacts to this decrease, and one can use the advantages of a low pressure for the magnetic trap stage and the transport while having at the same time the benefits from high pressure, i. e. high atom number.

The initial loading rate of the MOT R is directly proportional to the rubidium background pressure in the vapor cell. We exploit this proportionality to measure the time constant with which the background pressure settles back to its equilibrium value. For this purpose, the UV source is turned on for 10 s, which is more than sufficient to solve the majority of absorbed atoms

from the wall, then turned off again. After a varied delay time t, the MOT is loaded for 300 ms and the atom number in the MOT after this duration is determined. This number serves as a measure of the pressure. Note, however, that especially for short times t this is only an integrated (over 300 ms) value because the pressure falls very quickly in the beginning. The actual pressure-time-dependence is probably even more pronounced than in our results in figure 3.4. This aspect may have been interpreted incorrectly in reference [66]

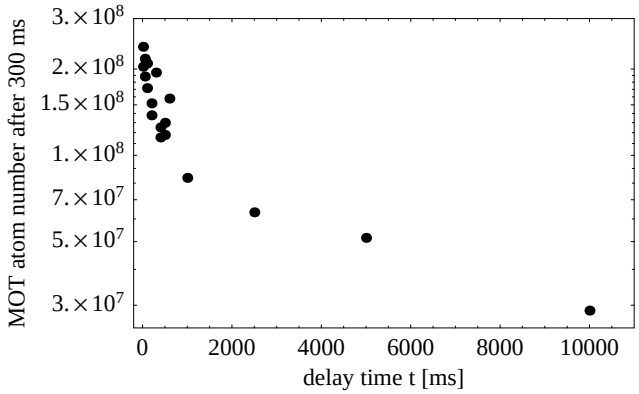

Figure 3.4: Atom number in a MOT after 300 ms loading with different delay times t after turn-off of the LIAD UV-light. The atom number is proportional to the background pressure integrated over 300 ms at time t. The figure shows the data on logarithmic scale: clearly two time constants, which suggest two different participating processes, are involved while the pressure is returning to its initial value.

as they employed the same measurement method (varying delay time with 300 ms loading time), but assumed the resulting curve to be proportional to the pressure decay. We can, however, confirm their results that the pressure drop involves two time constants: an initially very fast fall turns into a slow convergence to the value received without the use of desorbing light. This can be explained if adhesion of Rb atoms to a glass surface is more favorable than to a rubidium layer. If this is the case, the first layer of atoms will build up

on the glass very quickly while the later layers will need more time to develop. With a photodiode, we also measured the fluorescence of a MOT loaded with LIAD after the UV-light had been turned off: it takes many seconds ($\sim 30\,\mathrm{s}$) for the fluorescence to decay to a value equal to the fluorescence if loaded without LIAD.

The enhancement factor of the atom number by use of LIAD is about 20-30 for very low background pressures. Similarly to the procedure in section 3.22, we also examined the enhancement as a function of background pressure: the rubidium oven was opened and over a duration of two hours the atom number in MOTs loaded without and then with LIAD was measured along with the lifetime of a magnetic trap, which is inversely proportional to the background pressure in the vapor cell. The data was taken in intervals of five minutes to allow enough time for readsorption of the dissolved atoms. It is shown in figure 3.5. It was found that for higher pressures the positive effect of LIAD degrades dramatically and finally vanishes. This is not surprising since the MOT atom number does not increase with rising background pressure anymore in the regime where the rubidium density dominates the density of other species in the MOT (see explanation in chapter 2). Consequently, the additional increase of pressure by LIAD does not show any effects. The enhancement for low background pressures is not large enough to operate the apparatus in this regime: with the short transport times to the "square chamber" realizable with the translation stage, it is still more efficient to load a MOT with a large atom number at high pressure than to load it with LIAD at a low background pressure.

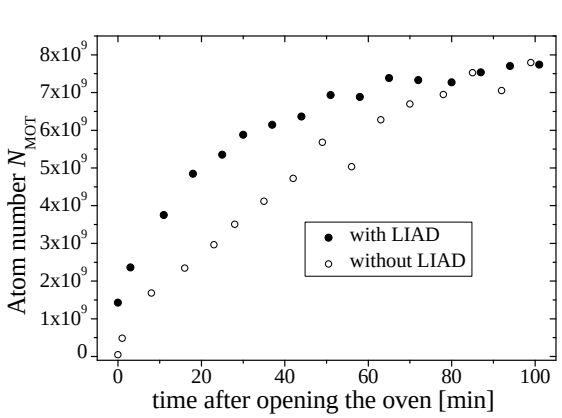

(a) MOT atom number N_{MOT} with and without LIAD

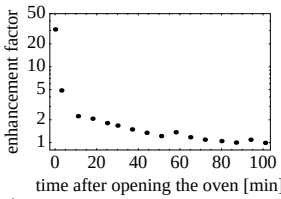

(b) Enhancement by LIAD

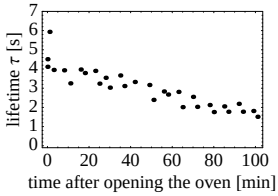

(c) MT lifetime τ_{VC}

Figure 3.5: Light induced atomic desorption: figure (a) shows the atom number in the MOT N_{MOT} as a function of time after opening the oven, so as a function of background pressure with and without the use of LIAD. Figure (b) shows the enhancement, i. e. the ratio of the two data sets in figure (a). Figure (c) shows the decrease of the lifetime τ_{VC} in the vapor cell during the experiment. The runs were taken in equal intervals over a time of two hours after the rubidium oven at a temperature of 22 °C had been opened.

3.4 Compressed magneto-optical trap

While the low field gradient of a MOT is suitable to capture a big number of atoms and to reduce losses due to reabsorption of photons, it is not adequate for the following sequence steps for two reasons. First, the density of the cloud is low, which is not desirable for evaporative cooling; second, the size of the cloud is large, which makes transfer into a magnetic trap difficult. Therefore, a typical element in any preparation sequence is the compression of the magneto-optical trap (CMOT), first demonstrated by Petrich *et al.* [65]. It exploits the dependence of the density n in a MOT on the spring constant κ in the regime where the density is limited by reabsorption of scattered photons (see chapter

2) [52]:

$$n = \frac{3\kappa c}{I\sigma_{\mathrm{l}}^2(\sigma_{\mathrm{r}}/\sigma_{\mathrm{l}} - 1)} \quad , \tag{3.9}$$

where σ_{l} is the cross section for absorption of photons from the laser field and σ_{r} the cross section for reabsorption of scattered photons. The spring constant κ is proportional to the field gradient b. An increase of b, therefore, raises the density in the MOT. This is, however, only a transient effect as the capture volume of the MOT, which influences the maximum atom number, is decreased by the compression. After a time comparable to the trap loss constant τ (equation 2.26), the gain in density must be paid with a loss in atom number. Therefore, the compression must be fast and immediately followed by the switch-off of the MOT and an efficient cooling stage by optical molasses that reduces the high temperatures in the cloud (some hundred microkelvins) after MOT and CMOT.

The CMOT was optimized with respect to the following conditions (in this order): first, the total atom number should not decrease significantly during the compression[3]. Second, the density is to be maximized. Similarly to [65], we found that a ramp of the magnetic field gradient is better than a sudden change, during which atoms can be lost. The two parameters to be varied in the CMOT step are essentially the ramp time and the maximum field gradient after compression. In practice, we optimized the CMOT with a subsequent standard molasses stage (see figure 3.6(b) for illustration of the sequence). Because we observed that the cooling effect of any molasses is

[3]This follows the general agreement that the atom number is the most important single parameter of a MOT/CMOT in predicting the chances for a BEC.

quite independent of the properties of the cloud that is loaded into it (such as atom number, density, and temperature), we think that this was an acceptable procedure. Adding the molasses, however, allows us to determine the temperature more easily due to the low temperatures produced by it. Figure 3.6(a) shows the phase space density $\mathcal{D}$ (defined in chapter 1) for various final field gradients after the compression and application of optical molasses. Because there is no strong dependence visible, we decided on using the parameters for which we lose the least atoms. For a final field gradient of about 90 G/cm (in lab units[4]: A07 = 2.0 V and a compression time of 500 ms), we lost an negligible amount of atoms. It was not necessary to adjust the detuning for

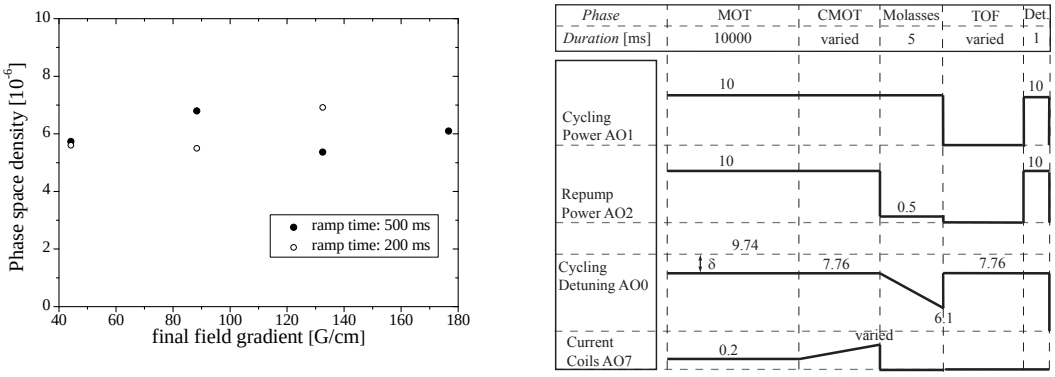

(a) Phase space density $\mathcal{D}$ (b) Sequence

Figure 3.6: Optimization of the compressed MOT: figure (a) shows the phase space density $\mathcal{D}$ after MOT compression and molasses for different field gradients after the compression. Figure (b) illustrates the employed sequence. The compression time and the final field gradient are varied. The temperature is determined by time of flight measurements after a standard molasses. The atoms are detected (Det.) by fluorescence imaging. All values are in lab units.

the CMOT compared to the MOT stage. It must be mentioned, however,

[4]The calibrations defining the lab units are listed in appendix B.3.

that these measurements were taken at a time when the background pressure in the MOT cell as well as the absolute atom number in the MOT was very low. In later measurements, we directly observed the losses in each single sequence step (see section 3.9.3). The CMOT still worked well for small clouds (negligible losses compared to MOT), but for high MOT-numbers of up to 10×10^9 atoms it had to be readjusted so that we could still hold about 85% of the initial atom number. Both the final field gradient and the detuning had to be increased. For large clouds, the best parameters are a compression to $\partial B/\partial z = 110\,\mathrm{G/cm}$ (A07 = 2.5 V) and a jump of the detuning after the MOT stage from $-3.5\,\Gamma$ to $-4.9\,\Gamma$. This confirms an assumption made in [65]: for big MOTs the atom number is limited by reradiation of absorbed photons. Because the dependence of the reradiation force on the detuning is stronger than for the trapping forces, increasing the detuning helps hold the atoms.

3.5 Molasses

The CMOT is followed by an optical molasses stage for further cooling. Although in early BEC experiments [5] the clouds were directly loaded from the CMOT into the magnetic trap, it was clear from the beginning that this could not be realized with the high atom number in our experiment. We found temperatures after MOT and CMOT that were substantially higher ($\sim 900\,\mu\mathrm{K}$) than the Doppler limit $T_\mathrm{D} \approx 146\,\mu\mathrm{K}$. We tried to reduce this temperature by varying different parameters with little success. However, a general dependence of the attainable temperature on the absolute number of atoms in

the cloud was observed (see figure 3.7). We first tried to lower the temper-

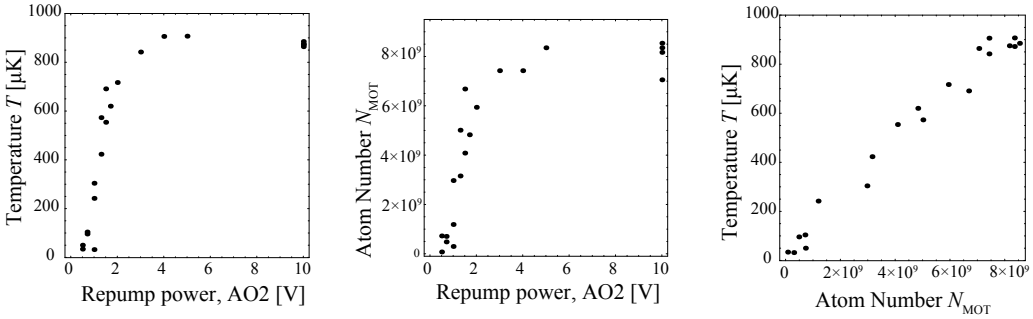

(a) Temperature dependence

(b) Atom number dempendence

(c) Temperature vs. atom number

Figure 3.7: Temperature in a MOT as a function of atom number: figure (a) shows the dependence of the temperature in a MOT on the repump power. Figure (b) shows the atom number for the same experimental runs as in (a). The similar trends suggests a direct relation of temperature and atom number, plotted in (c)

ature in a MOT by changing the repump power, which could be a source of unnecessary heating. We found that as soon as the temperature decreases, the atom number also starts declining. Plotting the atom number against the temperature though shows that there is a direct relation between these two quantities for large MOTs, probably because of the increasing importance of multiple scattering with increasing atom number.

The temperatures attained in our MOT are a bad starting point for magnetic trapping. For this reason, one usually implements an optical molasses stage, which further cools the atoms down. During the molasses, we sweep the detuning of the cycling linearly from $\delta = -3.5\,\Gamma$ to a final value of $-6.0\,\Gamma$ in 5 ms. During this interval, the cycling laser is kept at full power while the repump laser is switched to a value of $\sim 2\%$ of its maximum power. This did not affect the atom number compared to leaving the repumper at full

power, but reduced the temperature by a factor of two. In combination with the CMOT, the molasses reduces the temperature to 25 µK (figure 3.8). This value was very robust against fluctutations in atom number, changes in the CMOT, etc. Detuning the laser during the molasses further from resonance would produce even lower temperatures, but also increase the losses in atom number. The PSD $\mathcal{D}$ after the molasses is on the order of 1×10^{-5}.

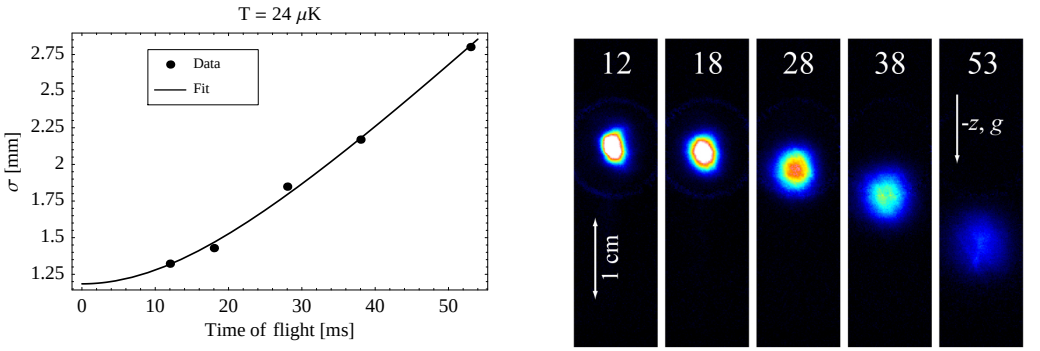

(a) Analysis

(b) Time-of-flight images (times in ms)

Figure 3.8: Determination of molasses temperature by time of flight measurements. The phase space density $\mathcal{D}$ after optical molasses is $\sim 1\times10^{-5}$. The solid line in figure (a) is the model (equation 3.8).

3.6 Optical pumping

After cycling the rubidium atoms on the $(5\,^2\mathrm{S}_{1/2}, \mathrm{F}=2 \rightarrow 5\,^2\mathrm{P}_{3/2}, \mathrm{F}'=3)$-transition during the laser cooling stages, we are principally able to magnetically trap three species, namely atoms in the $m_F=-1$-substate[5] of $F=1$ ($|1,-1\rangle$) or in the $m_F=+1,+2$-substates of $F=2$ ($|2,+1\rangle$, $|2,+2\rangle$). A

[5]Note that for $F=1$ the g_F-factor is $-1/2$. Therefore, the state with *negative* m_F is low-field-seeking.

$|1,-1\rangle$-cloud can be produced by turning off the repump laser for a few milliseconds after molasses while still cycling: all atoms will eventually gather in the $F=1$-state, which has only one magnetically trappable substate $m_F=-1$. We decided, however, on choosing the $|2,+2\rangle$-substate since the trapping force $g_F m_F \mu_B \partial B/\partial z$ is twice as large, giving us a factor $2^3 = 8$ in the initial density before evaporation. The hyperfine level $F = 2$ has five substates. If the magnetic trap stage is placed directly after the molasses, only a certain fraction of the atoms (less than 20 %), which is determined by the Clebsch-Gordon coefficients, would be in the $|2,+2\rangle$-substate. In order to collect as many atoms in the $|2,+2\rangle$-state as possible, optical pumping of atoms in other states to $|2,+2\rangle$ is implemented following the molasses phase.

Because we observe that complete pumping to $|2,+2\rangle$ is not possible (see below), we choose the parameters for the magnetic trapping (see corresponding section) such that the atoms in the other trappable substate of $F = 2$ ($|2,+1\rangle$) are also caught. They will function as a cooling agent during evaporation for the $|2,+2\rangle$-atoms because they are first evaporated in a magnetic trap due to their weaker confinement. This "sympathetic cooling" was first demonstrated by Myatt *et al.* [67]. In the pumping step, the cloud is exposed to on-resonance σ^+-polarized light from the pumping laser for several milliseconds. We couple this light out of the linearly polarized, on-resonance absorption imaging beam with a polarizing beam splitter (see figure 2.1). The power of this pumping beam is on the order of 100-200 µW (on a area of 4 cm^2). The efficiency of the pumping can be analyzed with the Stern-Gerlach method described below (section 3.6.1). Doing this, we found that complete pumping to the $m_F = 2$-

state is not realizable. It was never possible to bring more than $\sim 65\%$ in the $|2,+2\rangle$-state with $\sim 25\%$ in the $|2,+1\rangle$-state. Bad alignment, insufficient pumping power, mismatched polarization, and incomplete repumping were ruled out as reasons. Instead, it is very likely that reabsorption of photons with random polarization scattered by the optically dense cloud limits the pumping efficiency. This is quickly shown by a rough estimate. The mean free path l of a photon is given by $l = \frac{1}{n\sigma_{\rm sc}}$, with n the atom density and $\sigma_{\rm sc}$ the scattering cross section. We use $\sigma_{\rm sc} I = \hbar\omega\Gamma_{\rm sc}$:

$$l = \frac{1}{n\sigma_{\rm sc}} = \frac{I}{n\hbar\omega}\frac{2}{\Gamma}\frac{1+s_0+(\frac{2\delta}{\Gamma})}{s_0} \approx \frac{I_s}{n\hbar\omega}\frac{2}{\Gamma} \quad \text{for } I \ll I_s \text{ and } \delta = 0. \qquad (3.10)$$

and typical values ($I_s = 1.67\,\mathrm{mW/cm^2}$ [6], $N = 5\times 10^9$, $V = 4/3\pi\sigma^3$, with $\sigma = 3\,\mathrm{mm}$), this gives $l = 0.1\,\mathrm{mm} \ll \sigma$, so on average, a photon will experience multiple rescattering. This is in agreement with the following observations: the pumping efficiency gets smaller for larger atom numbers in the MOT. We see differences on the order of 10 % for clouds whose atom numbers differ by a factor of 5. Also, the pumping efficiency could be increased significantly by first releasing the cloud and allowing the density to decrease before pumping. The fraction of atoms in $|2,+2\rangle$ increased from $\sim 60\,\%$ to $\sim 80\,\%$ when the time of flight before pumping was increased from 4 ms to 20 ms.

This is a basic limitation for our experiment, for we cannot afford a reduction of the density, which is decisive for the success of evaporation. Eventually, we use pumping times of 4-8 ms. The relative gain in atom number (in the $m_F = 2$-state) depends strongly on the absolute atom number: for unpumped

[6] This is the saturation intensity for σ^+-light on the cycling transition. See appendix D.

clouds, we measured 41 % in the two trappable states ($m_F = 1$: 24 %, $m_F = 2$: 17 %, atoms in molasses $\sim 8 \times 10^8$), shown in figure 3.10[7]. With pumping, we could bring as many as 90 % in trappable states for small clouds[8] (24.5 %, 65.5 %, 8×10^8). For the highest atom numbers possible with our apparatus, this ratio goes down to[9] ~ 50 % (14.5 %, 35.5 %, 6.3×10^9).

3.6.1 Stern-Gerlach analysis of optical pumping

In order to determine the efficiency of the optical pumping phase described in the previous section, we exploit the separation of the five magnetic substates of $5\,^2\mathrm{S}_{1/2}, F = 2$ in an inhomogeneous magnetic field by performing a Stern-Gerlach measurment. Figure 3.9 shows schematically the sequence we employ. After pumping, we let the cloud fall for 19 ms. After this time, the cloud is at a position where the magnetic field gradient (and thus the force it exerts) has a definite direction (whereas around the trap center the field lines go in all directions). Here the field of the quadrupole coils is suddenly turned on at a value of 353 G/cm for 5 ms. This kicks the atoms of the different substates in different directions, with different accelerations and with different final speeds after this flash (or has no effect on them[10] for $m_F = 0$), thus spatially separating them. To achieve full separation, we let the system evolve for another 14.5 ms before detection with just a very weak bias field turned on

[7] run 37, 02/17/2007

[8] run 40, 02/17/2007

[9] run 38, 03/02/2007

[10] After $t = 19$ ms time of flight, the atoms experience a magnetic field strenght of $B = 353\,\frac{\mathrm{G}}{\mathrm{cm}} \times \frac{1}{2} g t^2 = 63$ G. This magnitude is well in the low-field regime for the $\vec{I}$-$\vec{J}$-coupling. The hyperfine Paschen-Back regime for the $5\,^2\mathrm{S}_{1/2}$ ground state starts around 1000 G (see reference [48]).

to avoid relaxation. Figure 3.10(a) shows a typical image for an unpumped cloud consisting of five separated density peaks representing the five substates. It can also be seen that for the "negative" substates ($m_F = -1, -2$) the clouds are expanded in the x-y-plane while the "positive" substates ($m_F = +1, +2$) are compressed. This is caused by the components of the field gradient in the x-y-plane, which only vanish on the z-axis. The cloud, however, is not a point on the axis, but an extended object, which explains the deformations. For the analysis, we calculate the column density on the z-axis from the pictures and use a fitting procedure to calculate the relative atom numbers in each of the states. The model function is the sum of five Gaussians with equally spaced centers and the same width. The relative atoms numbers are then given by the ratios of the five amplitudes (compare figure 3.10(b)).

3.7 Magnetic trap

Pumping to trappable states marks the last optical step on the road to BEC. Following this, the atoms are transferred to a magnetic trap (MT), then transported to the science cell, where eventually the evaporative cooling will take place. The magnetic trap of our experiment is of the quadrupole type with the strong axis in the direction of gravity (see chapter 2). The coils support currents up to 450 A, which corresponds to a field gradient of 400 G/cm. The field gradient per current is 0.88 G/(cm A). The coils can be switched on in 1.25 ms and completely switched off in 1.5 ms[11] using an integrated gate bipo-

[11] After these times, a steady state in current is reached again.

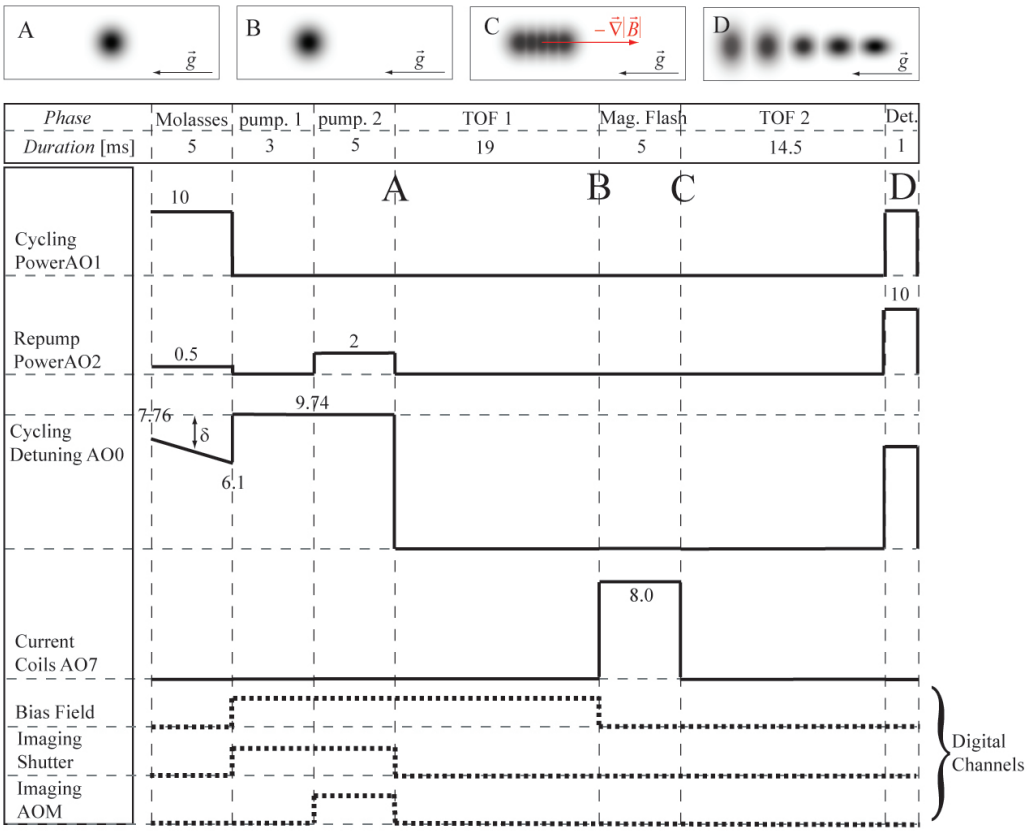

Figure 3.9: Stern-Gerlach analysis sequence: the schematic starts with optical molasses as the last step of the preparation sequence before optical pumping. The MOT and CMOT stages are left out. Optical pumping is executed in the stage "pump 2" by flashing on the imaging AOM. The stage "pump 1" is necessary to allow the imaging shutter enough time to open and to bring the majority of atoms into $F = 2$. Then the cloud is released (A) and falls for 19 ms to a position where the direction of the field gradient is well defined for the entire cloud volume (B). During this time of flight, a weak bias field prevents spin relaxation. Then the magnetic field is suddenly turned on for 5 ms, thereby separating the five substates (C). The system evolves for another time of flight of 14.5 ms to guarantee sufficient separation of the five substates at detection (D).

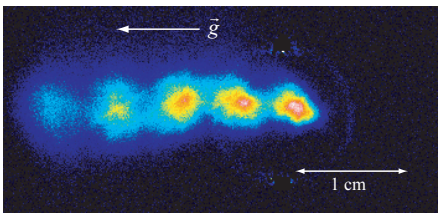

(a) Stern-Gerlach image

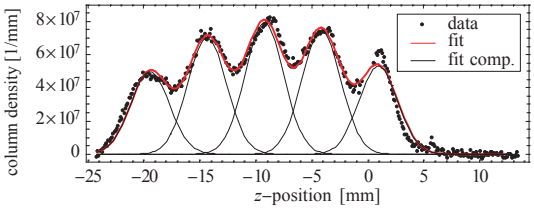

(b) Stern-Gerlach analysis

Figure 3.10: Figure (a) shows a typical result of a Stern-Gerlach measurment. Figure (b) shows the analysis: the resulting 1-D column density is fitted with a model function consisting of the sum of five Gaussians (equally spaced, equal widths, but different amplitudes).

lar transistors, which will be described along with the circuitry and the power supply in reference [39].

Optimization of the magnetic trap stage involves several aspects: a reasonable value for the initial magnetic field (from now on referred to as "catch field") has to be found. Ramping up the field starting with $\partial B/\partial z = 0$ or with a very low field gradient is unfavorable because the cloud could expand non-adiabatically during the ramp and gravity would cause a significant offset of the center of mass of the cloud with respect to the minimum of the potential, which would lead to a sloshing motion, i. e. additional energy, heating the cloud during rethermalization. However, if the field is starting with a high value, large parts of the cloud will suddenly be placed in regions of a high potential energy, which will introduce additional kinetic energy, again resulting in heating. There is consequently an optimum value for the catch field. This is sometimes referred to as mode matching [68]. The other concern in the MT phase is the compression of the trap. Here, a slow enough ramp speed needs to be found that guarantees adiabaticity and thus conserves phase space density.

The ramp also needs to be speedy since we want to move the MT as fast as possible out of the vapor cell (where it is exposed to more trap loss collisions than in the "good" vacuum in the square chamber and the science cell). We also have to pass the narrow differential pumping tube (see the machine drawing 2.1) with the MT, imposing a size limitation. Therefore, the MT needs to be (at least partially) compressed when it enters the tube in order to avoid hitting its edges.

3.7.1 Switching on the magnetic trap: the optimum catch point

The systematic measurements for the MT stage were done when it was still intended to produce a $|1,-1\rangle$-condensate. Later it was decided to seek a $|2,+2\rangle$-condensate because the magnetic force is twice as strong for this state, yielding a density eight times larger in the MT compared to $|1,-1\rangle$. The optimization described in the following paragraphs was not redone in full scale, but the results can be immediately applied to the $|2,+2\rangle$-state by rescaling the magnetic field by a factor of 2. To optimize the catch point we used the sequence illustrated in figure 3.11. The cloud is captured with a constant magnetic field, which stays turned on for 150 ms. This duration of the step ensures that all atoms in the $m_F = 0$-state have enough time to fall out of the field of view. It is also needed to observe the effect of a field gradient that causes a force on the $m_F = -1$-atoms just about as strong as gravity: if gravity exceeds this force just a bit, the cloud should slowly fall during the holding time. If, on the other hand, the magnetic force is slightly stronger than gravity,

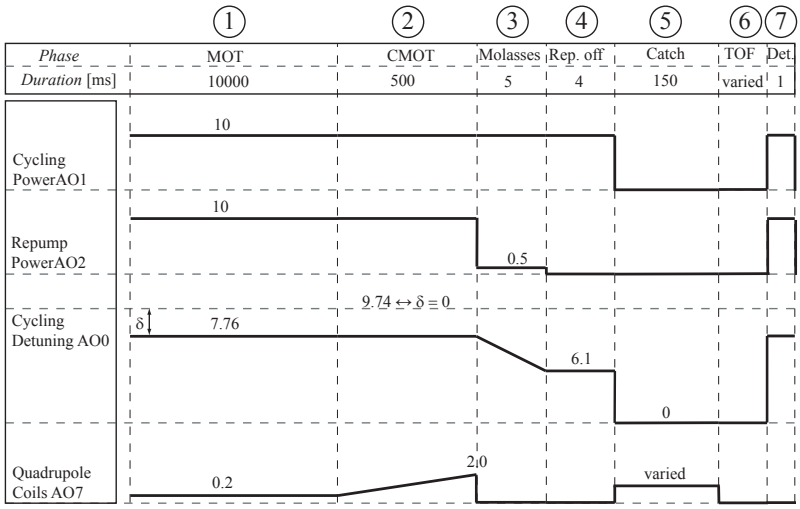

Figure 3.11: Sequence used to optimize the catch point (not drawn to scale): the "Repump off"-step (no. 4) creates a $F=1$-cloud. The magnetic field in the "catch"-step (no. 5) is varied. For each value of this field, we also vary the time of flight in order to determine the temperature. All values are in lab-units, i. e. the voltages applied on the analog channels. (Decreasing the AO0-voltage means actually increasing the (absolute) value of the detuning; the detuning must be measured from AO0 = 9.74 V as indicated in the schematic.)

the potential is deformed (as shown in figure 3.12), but its minimum stays at the same position. In thermal equilibrium, the density of the atoms in the trap is given by:

$$n(x,y,z) = n_0 \mathrm{e}^{-\frac{V(x,y,z)}{k_\mathrm{B}T}} = n_0 \mathrm{e}^{-\frac{g_F m_F \mu_\mathrm{B} b_z/2\sqrt{x^2+y^2+4z^2}+gmz}{k_\mathrm{B}T}} \quad , \tag{3.11}$$

where $V(x,y,z)$ is the full potential energy (consisting of the gravitational energy and the potential energy due to the magnetic field), $b_z = \partial B/\partial z$ the axial field gradient, g the earth acceleration, and m the mass of ^{87}Rb. It can be easily seen that the position of the maximum density does not change due to gravity. In our analysis, we do, however, not observe the actual density, but

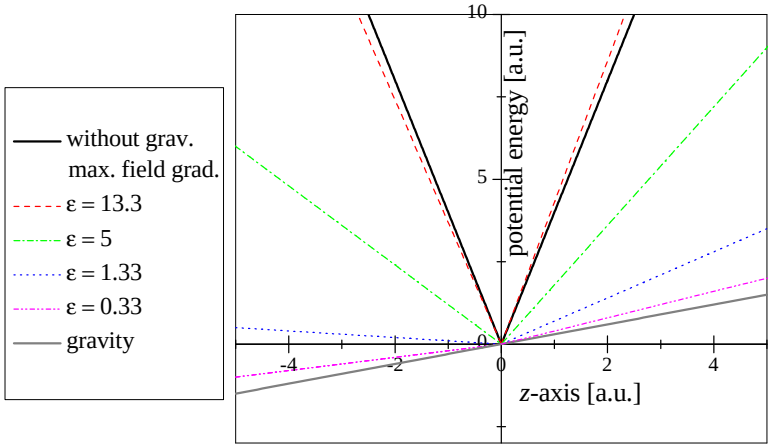

Figure 3.12: Gravity adds an additional term to the potential energy that breaks the point symmetry with respect to the field zero along the z-axis. This effect must be taken into account when the catch field for the magnetic field is chosen. The figure shows different situations: the pure magnetic potential (for maximal field gradient) and gravity is shown. The other curves represent the full potential for different field gradients $\partial B/\partial z$. The dimensionless quantity ϵ is defined as $\epsilon = \frac{m_F g_F \mu_B b_z}{mg}$. The ratios refer to $m_F = -1$ ($g_F = -1/2$).

we detect the projection of the cloud into the y-z-plane (which corresponds to an integration along the imaging axis x) and we then sum up the columns of the image with the analyzing routine again along the y-axis. Eventually, only the column-density along the z-axis is discussed. After integration along the x-axis one obtains for the two-dimensional density distribution ("column density") [69]:

$$n(y,z) = 2n_0 \mathrm{e}^{-\frac{mg}{k_B T}z} \sqrt{y^2+4z^2}\, K_1\left(\frac{1}{2}\frac{g_F m_F \mu_B}{k_B T}\frac{\partial B}{\partial z}\sqrt{y^2+4z^2}\right) \quad , \qquad (3.12)$$

where K_1 is the modified Bessel function of the second kind and first order. Figure 3.13(a) shows a column density plot for a magnetic force that is just

16% stronger than gravity, both in experiment and theory. It can be seen that the cloud leaks out in the direction of gravity. Also, the highest column

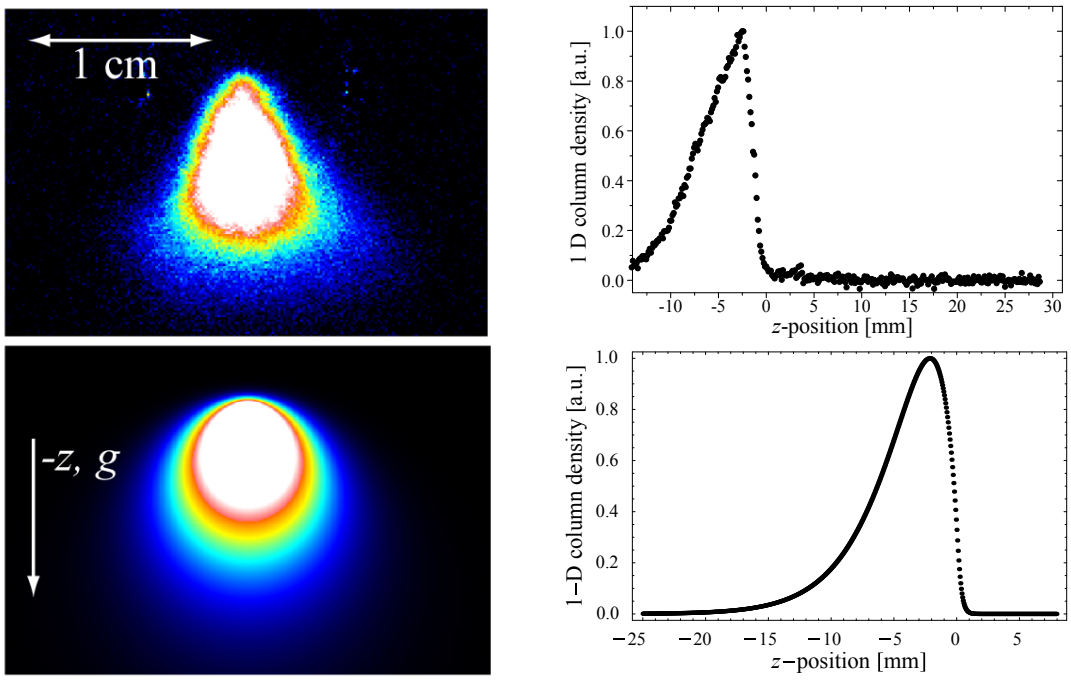

(a) (b)

Figure 3.13: Effects of gravity on clouds in linear potentials: figure (a) shows a density plot of an atom cloud in a linear potential that is just slightly stronger than gravity, $\epsilon = \frac{m_F g_F \mu_B b_z}{mg} = 1.16$. The top picture is the experimental data (after a time of flight of 5 ms) and the bottom one the theoretical calculation. The differences in shape is due to incomplete rethermalization after 150 ms. Figure (b) shows the 1-D column density (numerical top, experimental bottom) after summation along the y-axis. The maximum is shifted away to -2.16 mm from the minimum of the potential at $z = 0$.

density is not at the minimum of the potential. This effect is enhanced further by summation along the y-axis (which is done in the image analysis) as shown in figure 3.13(b). Consequently, when we extract the maximum of the column density, there is no sharp transition for its position when the magnetic force

surpasses gravity. This is reflected in figure 3.14(a), where the vertical dashed line marks the critical field gradient of $b_{\mathrm{crit}} = 30.6\,\mathrm{G/cm}$ that is necessary to support the $|1,-1\rangle$-atoms against gravity. Figure 3.14(b) shows the temper-

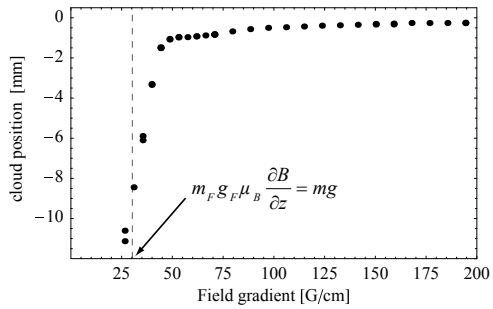

(a) Position of 1D peak column density after 150 ms of hold

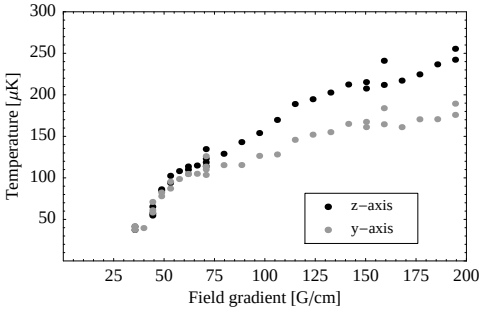

(b) Temperature after catch

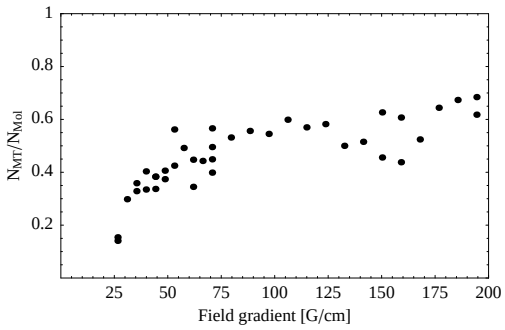

(c) Transfer efficiency to MT

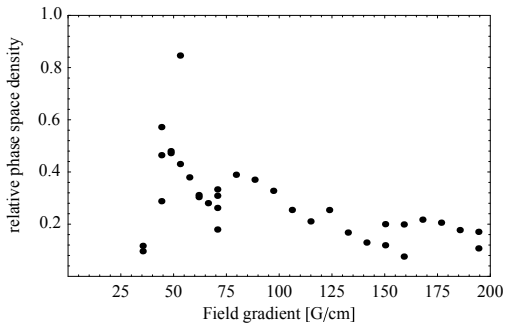

(d) Phase space density $\mathcal{D}$

Figure 3.14: Optimization of catch point for $|1,-1\rangle$-atoms. For discussion see text.

ature of the cloud after the hold in the trap (phase 5). The lowest values are close to the temperature we measured for the pure molasses (section 3.5). There is no significant heating by low catch fields. This changes for higher catch fields. It can also be seen that the temperatures[12] along the y- and the z-axis drift more and more apart for higher catch fields because the atoms ac-

[12]Note that these are not actual temperatures, but rather parameters describing the width of the velocity distribution along the axes. See the discussion in section 3.2.

quire more excess momentum along the z-axis where the field gradient is twice as strong as on the y-axis. This also means that the rethermalization time for the trapped clouds at those field gradients is longer than 150 ms, which is also suggested by the different shapes in figure 3.13(a). Figure 3.14(c) gives the fraction of atoms that are still present in the trap after the 150 ms hold duration. Above the critical field gradient this fraction first rises faster, but slows down. This is because for low field gradients the potential is very shallow for negative z (figure 3.12), allowing high-energetic atoms to escape as the trap depth discussed in chapter 2 is lowered by gravity[13]. Figure 3.14(d) shows the deduced phase space density $\mathcal{D}$ in arbitrary units after the procedure. As expected and just explained, the maximum of $\mathcal{D}$ is not found at the critical field gradient b_{crit}, but at a slightly higher value of $\sim 45\,\mathrm{G/cm}$. For lower field gradients (around b_{crit}), non-adiabatic expansion (that reduces the density n), and the thermal losses of fast atoms going over the hump of the potential (which diminishes the atom number N) reduce the phase space density while higher field gradients add excess potential energy that converts into kinetic energy, thus raising T and again reducing $\mathcal{D}$.

An attempt was made to redo this catch point analysis for a mixed $|2,+1\rangle$, $|2,+2\rangle$-cloud, but we had to deal with a quite unstable performance of the machine when the data was taken (appendix B.2). The results are shown in figure 3.15 and seem to confirm the earlier ones. As complete pumping to the $|2,+2\rangle$-state is not possible, it is not expected that the optimum catch

[13]Compare figure 3.13 and figure 2.8(b). Gravity makes the potential shallow (figure 3.13), but the linear potential, which is only an approximation around the field zero, does, of course, not extend to infinity. Rather, there is a hump (figure 2.8(b)), approximately at a position comparable to the radius of the quadrupole coils.

point would change significantly: if the catch point remains unaltered, there is, of course, more heating due to the acquired potential energy for the $|2,+2\rangle$-atoms. The resulting reduction of $\mathcal{D}$ is, however, compensated above a certain field gradient because the $|2,+2\rangle$-atoms are caught as well as the $|2,+1\rangle$-atoms. The final catch point was chosen at $\partial B/\partial z$= 48.5-53 G/cm (AO7 = 1.1-1.2 V),

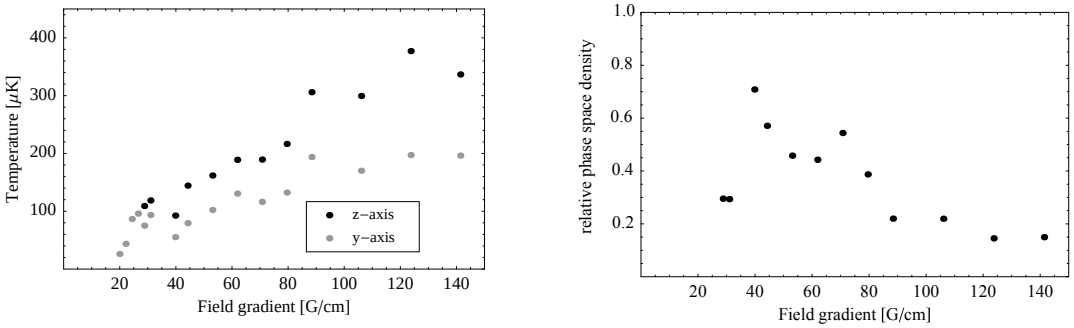

(a) Temperature after catch

(b) Phase space density $\mathcal{D}$

Figure 3.15: Optimization of catch point for pumped $|2,+2\rangle$-atoms-clouds

slightly higher than the optimum determined above, in order to minimize the loss of atoms during the subsequent compression of the magnetic field (see next section).

3.7.2 Compression of the magnetically trapped cloud

The next concern is to find a rate for compressing the magnetic field so that adiabaticity is guaranteed and $\mathcal{D}$ stays unaltered. The effect of this ramp is studied in the following way: the cloud is first caught with a catch field gradient of $\partial B/\partial z = 53$ G/cm (which is the optimum catch point, see previous section), which is immediately followed by a linear ramp of 125 ms to a varying peak field gradient and then again ramped down to 53 G/cm (compare figure 3.16). The

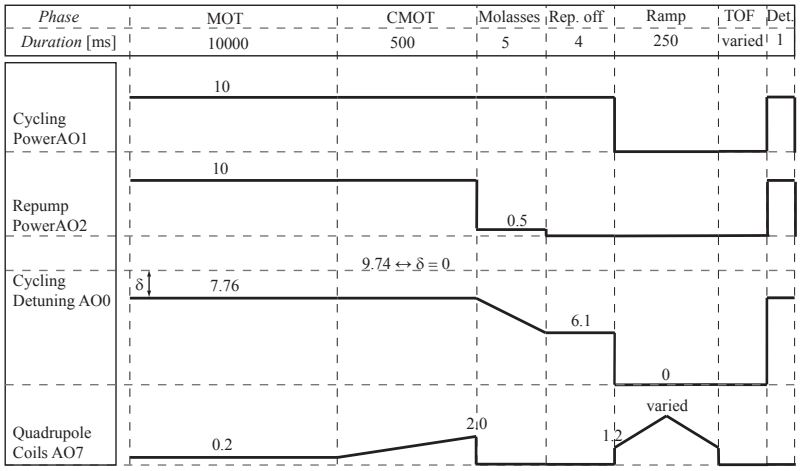

Figure 3.16: Sequence for ramp speed optimization: the atoms are caught with a catch field of 53 G/cm (AO7 = 1.2 V). The field is immediately increased linearly to a maximum field gradient within 125 ms and ramped down again in the same time to its initial value, followed by a temperature measurement.

"temperature" after this sequence is determined by the usual technique. With this method, different ramp speeds can be realized. An alternative method would be to ramp up to the same value and vary the ramp duration instead. However, such a procedure would suffer from the effects of the relatively short collisional lifetime in the vapor cell. Different heating rates are found for the z and the y-axis. This is expected because the field gradient along the z-axis is twice that on the y-axis and the procedure does not allow enough time for rethermalization. The heating rate due to ramping can, however, be estimated. The direction-dependent parameters T_x, T_y, and T_z are measures of the average kinetic energy of an atom in the specific direction:

$$\langle E_{\mathrm{kin}} \rangle \propto v_x^2 + v_y^2 + v_z^2 \ \propto T_x + T_y + T_z. \tag{3.13}$$

After rethermalization every degree of freedom carries the same energy according to the equipartition theorem, so:

$$T_x + T_y + T_z = 3T_{\text{reth}} \quad \Rightarrow \quad T_{\text{reth}} = \frac{1}{3}\left(T_x + T_y + T_z\right). \tag{3.14}$$

From fluorescence measurements, T_y and T_z can be extracted while T_x may be assumed to be the same as T_y because of the rotational symmetry of the trap in the x-y-plane. We assume that the non-adiabatic heating in a first approximation is not only dependent on the ramp speed $\Delta b/\Delta t$, but also, for a fixed rate $\Delta b/\Delta t$, on the ramp duration Δt, which is then proportional to $\Delta b = b_{\text{final}} - b_{\text{catch}}$. Therefore, figure 3.17 shows the dependence of temperature on the product of ramp rate and height $\Delta b^2/\Delta t$ additionally to the measured data in 3.17(a). The red line gives the rethermalization temperature calculated with equation 3.14. Its slope is $\kappa_{\text{ramp}} = (6 \pm 2)\,\frac{\text{K}}{100\,(\text{G/cm})\,(\text{G/cm/ms})}$. This calculation yields for a typical ramp of 350 G/cm in 500 ms a non-adiabatic heating of $\sim 15\,\mu\text{K}$. It must be mentioned that the error for this value is large as anticipated from the scatter of the data in figure 3.17(b). The error is $\pm 2\,\frac{\text{K ms}}{100\,(\text{G}^2/\text{cm}^2)}$. However, even in an extreme case, a full ramp from the catch point to the maximal field gradient with $\Delta b/\Delta t = 350\,\text{G/cm}/300\,\text{ms}$ and the upper bound of $\kappa_{\text{ramp}} = 8\,\frac{\text{K ms}}{100\,(\text{G}^2/\text{cm}^2)}$, leads to a non-adiabatic temperature increase of only[14] $\sim 33\,\mu\text{K}$ in contrast to $\sim 245\,\mu\text{K}$[15] by adiabatic heating. Perfect adiabaticity would require an infinitely slow ramp, which is, of course,

[14] $\Delta T_{\text{non-adiab}} = \kappa_{\text{ramp}} \frac{\Delta b}{\Delta t} \Delta b = 8.0\,\frac{\text{K ms}}{100\,(\text{G}^2/\text{cm}^2)} \times \frac{350}{300}\,\frac{\text{G}}{\text{cm ms}} \times 350\,\frac{\text{G}}{\text{cm}} = 33\,\mu\text{K}$

[15] $\Delta T_{\text{adiab}} = T_0(\eta^{2/3} - 1) = 245\,\mu K$ for $\eta = 8.2$ and $T_0 \approx 80\,\mu\text{K}$. The value for T_0 is taken from the data in figure 3.14(b).

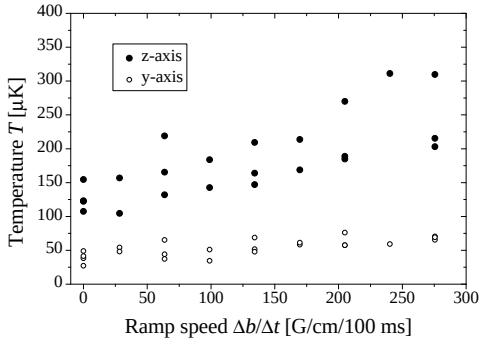

(a) Raw data

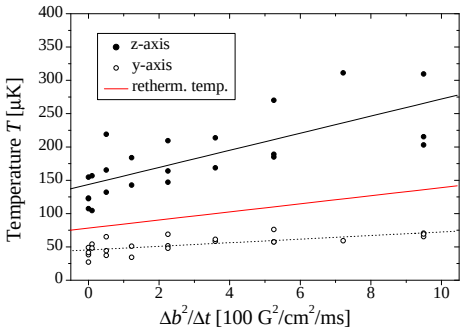

(b) Temperature as function of ramp speed and height

Figure 3.17: Effects of non-adiabatic compressing of the magnetic trap: figure (a) shows the data taken. In figure (b) the final temperature is plotted in dependence on the ramp speed $\Delta b/\Delta t$ and times the ramp height Δb. The red line gives the rethermalization temperature calculated with equation 3.14.

not viable due to the limited lifetime in the vapor cell. These measurements, again, were taken with $|1,-1\rangle$-clouds.

Other measurements also suggest that the typical ramp rates used by us come quite close to adiabaticity: instead of ramping the field gradient back down to its initial value (49 G/cm, AO7: 1.1 V) as in figure 3.16, the parameters T_y and T_z were measured immediately after reaching the peak field $b_{\max}$ gradient. From these values the rethermalization temperature T_{reth} can be calculated with relation 3.14 and compared to the expected value in an adiabatic compression with an initial temperature of $T_0 = 80\,\mu\mathrm{K}$. The latter value is the rethermalization temperature in the trap for a field gradient of $b_0 = 49\,\mathrm{G/cm}$ read off from figures 3.14(b) and 3.17(b). As derived in chapter 2, the temperature in an adiabatically compressed linear trap scales as $T = \eta^{2/3} T_0$, where η is the compression factor: $b = \eta b_0$. Table 3.1 gives the measured values

as well as the derived quantitites and the theoretically expected temperature T_{th}.

b_{max} [G/cm]	t_{ramp} [ms]	η	T_z [μK]	T_y [μK]	T_{reth} [μK]	T_{th} [μK]
124	250	2.5	262	136	**178**	**149**
353	750	7.3	428	270	**323**	**300**
398	750	8.2	453	289	**344**	**325**

Table 3.1: Comparison of measured temperatures and expected temperatures in an adiabatic process, assuming the initial temperature before compression was 80 μK. The initial field gradient b_0 was 49 G/cm.

The results listed in the table show that the measured temperatures are in reasonably good agreement with theory and that for typical compression rates in table 3.1 non-adiabatic heating is small compared to the adiabatic temperature increase.

To minimize the time spent in the vapor cell, the compression of the magnetic field can be done simultaneously with the start of the mechanical transport (see next section)[16]. In this case, one needs to make sure that the trap is already compressed enough upon entering the differential pumping tube that it fits through, with the inner diameter of this tube being $d = 10.9\,\mathrm{mm}$. For the maximum acceleration of the translation stage, the trapped atoms enter the tube at $t = 225\,\mathrm{ms}$ after the start of the transport. To estimate by what factor the magnetic trap must be compressed by this time so that

[16]By a simple argument it can be shown that atoms are not lost by the acceleration of the translation stage: the field gradient $b_z = \partial B/\partial z$ of the catch field is chosen so that it can support the atoms against gravity. The field gradient along the x-axis, which is the direction of the transport, is half of the one along the z-axis: $b_x = \frac{1}{2}b_z$. The maximum acceleration with which we operate the translation stage is $450\,\mathrm{cm/s^2} \approx g/2$ (with g being the earth acceleration). So, b_x should be equivalent to a force that has the same magnitude as the inertial force acting on the atoms because of accelerated motion and thus hold the atoms in the trap.

only a small ratio of the atoms is chopped off by the tube, we assume purely adiabatic heating and calculate numerically with equation 3.12 the radius ρ of a circle inside of which 95% of the trapped atoms are held. The center of this circle is chosen to be the center of mass in the two-dimensional distribution 3.12 (which does not coincide with either the peak 2-D-density or the peak 3-D-density because of the anisotropy due to gravity). Figure 3.18 shows the obtained values. The point at 155 G/cm is the field gradient reached at the front edge of the tube with a ramp rate of 47 G/cm/100 ms (which is the same as in the last row in table 3.1) and simultaneous motion with maximum acceleration: 95% of the atoms are within a radius of 3 mm. This means that the cloud should be able to pass the tube without significant losses as long as the center of this circle is not significantly displaced from the center of the tube and the path through the tube is parallel with respect to the axis of the tube. From the results of other measurements (section 3.9.3), we can conclude that the translation stages moves the trap apparently straight through the tube as we lose as little as 35 % on a two-way transport from the vapor cell to the science cell and back.

We conclude, therefore, that the compression rate will be determined by the speed of the first section of the transport since even for the maximum acceleration the compression can still be slow enough to guarantee adiabaticity. If one chooses, however, to wait with the transport, leaving even more time for the compression, one will apparently win only little in lowering the temperature, but accept a loss of atoms due to background collisions which is much more severe than the loss of phase space density in a faster ramp.

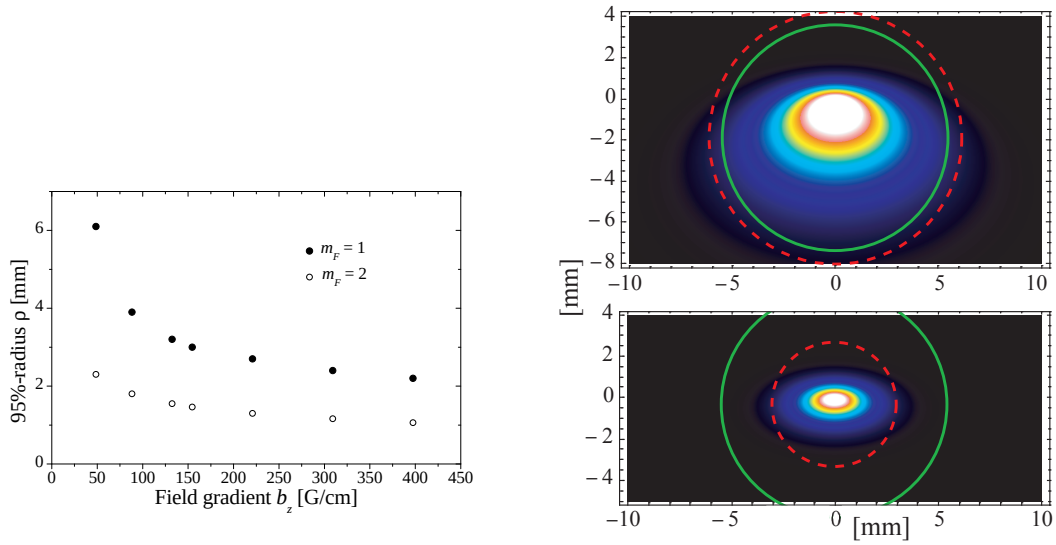

(a) Calculated cloud size ρ for different compression factors (adiabatic)

(b) Cloud in MT for two compression factors

Figure 3.18: Figure (a) shows the dependence of the 95%-radius on the field gradient. Figure (b) shows a visualization of the trapped cloud for the catch field gradient 49 G/cm (top) and 155 G/cm (bottom, the field gradient when the tube is reached). The green circle gives the size of the tube that the cloud enters during the transport. The red dashed circles are the 95%-radii ρ from (a) for $m_F = 1$-atoms.

3.8 Transport

The magnetically trapped cloud is moved on a z-shaped path by the translation stage to the science cell with ultra-high vacuum suitable for evaporative cooling. The path is shown in figure 3.19. The trap first passes the differential pumping tube, enters the "square chamber", makes a turn to the left, makes another turn to the right, and comes to a stop in the science cell.

The optimization of the transport efficiency to the science cell comprises two aspects: first, the effects of the acceleration on the temperature of the cloud have to be studied. Especially the first part of the motion, which is to

bring the atoms to the square chamber, should be fast in order to leave the vapor cell as quickly as possible. Second, the correct path has to be found to avoid accidental bumping of the cloud into pieces of the surrounding vacuum apparatus. For the following discussion we use a coordinate system as defined in figure 3.19. Luckily, the very first path programmed did not lose its entire

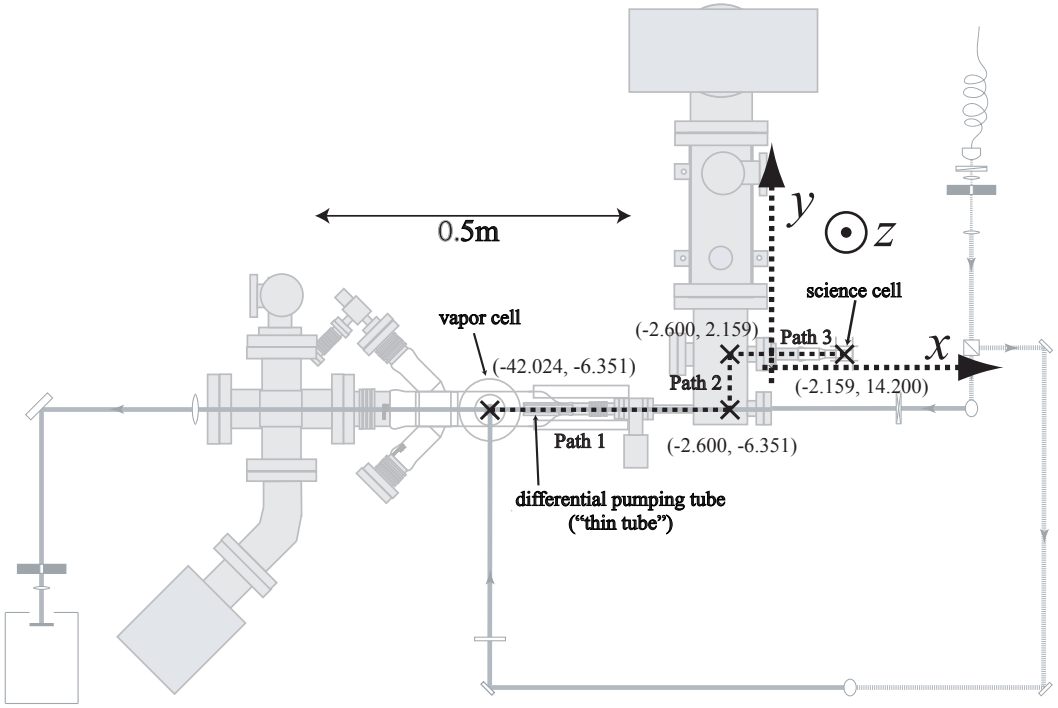

Figure 3.19: Defintion of the lab coordinate system and path of the transport. The picture also contains the coordinates limiting the final transportation path.

load and it was possible to detect atoms after loading, compressing the trap, and moving it all the way to the science cell and back. Only minor changes of this path were necessary. The different endpoints of the three (partial) paths in figure 3.19 were determined by a simple procedure: the compressed trap was moved to a specific point, which was varied in small intervals, moved back again, and the atom number was determined. Figure 3.20 shows the results for

the adjustment of the endpoint of path 3 in the science cell. The large scatter in the results for the y-position are probably due to the problems with the absorption imaging (see appendix B.2), which was used. The experiment for the y-axis was performed for three different durations for which the trap was held in the glass cell. From these results, it might be inferred that the curve gets sharper for longer holding times. This can be explained by the assumption that even for a fully compressed trap (the field gradient was 353 G/cm, A07 = 8.0 V) there are still some losses from collision with the walls, which will diminish the number of atoms more for positions close to the walls than in the middle of the glass cell, and thus a difference in the beginning will become more pronounced. This implies that the lifetime depends on the position in the glass cell. The figure also shows an analog measurement of the x-axis. Obviously, the cloud reaches the end of the science cell at ~ 18 cm. The final endpoint of path 3 will be determined by the installation of the TOP coils and probably be around 16 cm. Therefore, the dimensions of the glass cell in this direction will not be critical.

To measure the heating by the transport, we moved the trapped cloud with different accelerations and velocity profiles to the square chamber and back and performed then temperature measurements. We did not find any significant heating. This could, however, be due to the fact that for the short transfer times to the square chamber and back sufficient rethermalization is not guaranteed. If one expects the heating by the transport to act mainly along the direction of the transport (x), then this temperature increase could not be detected as the x-direction is also the optical axis of our imaging system.

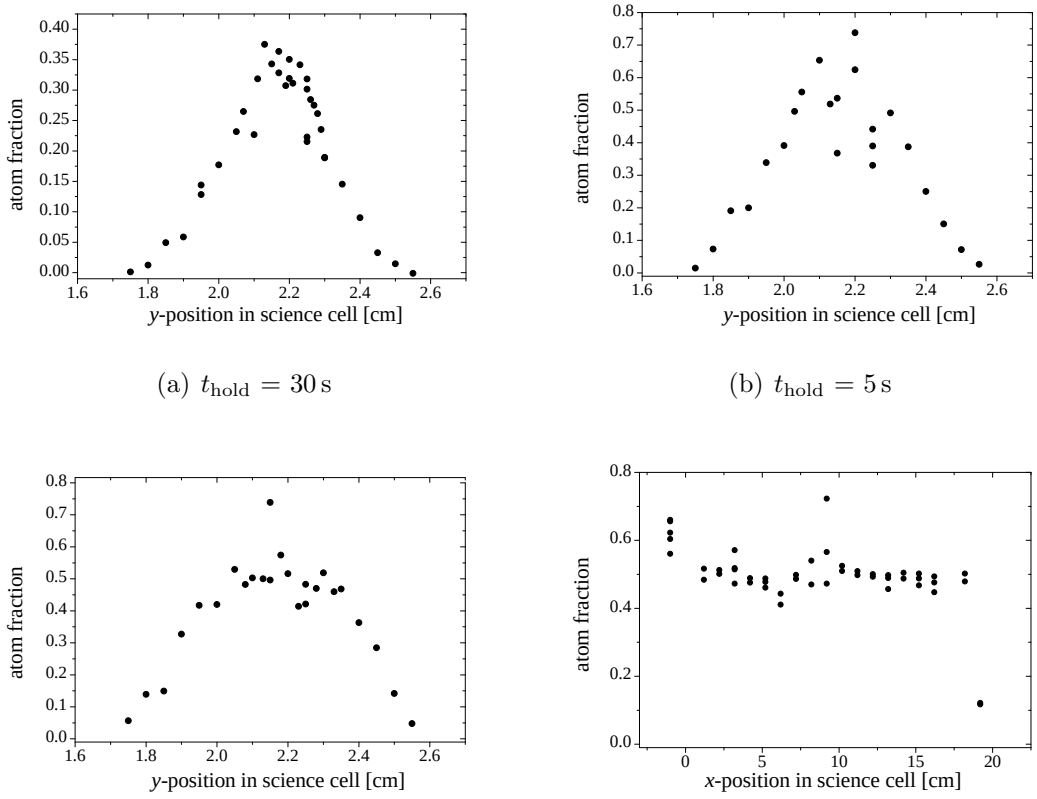

(a) $t_{\mathrm{hold}} = 30\,\mathrm{s}$

(b) $t_{\mathrm{hold}} = 5\,\mathrm{s}$

(c) $t_{\mathrm{hold}} = 0\,\mathrm{s}$

(d) x-axis

Figure 3.20: Optimization of transport: figures (a), (b), and (c) show the atom number after a full motion to the science cell and back, width the y-position in the science cell varied. The cloud was held for different durations t_{hold} in the science cell. The inner width of the glass cell in y-direction is 1.0 cm. Figure (d) shows the result of the same experiment with the x-position varied and the y-position held constant at 2.16 cm. Obviously, the cloud hits the end of the cell for x-values of $\sim 18\,\mathrm{cm}$ and larger.

Recent temperature measurements in the science cell, however, also suggest that there is indeed no significant heating by the transport. In the science cell, the temperature is determined by the measurement of the cloud's expansion in the y- and z-direction, which allows to study the effects of the first very fast transport motion to the square chamber. Given the racy motion of the translation stage in the experiments, it surprises that the transport does not cause additional heating. Though, if we apply the equivalence principle and compare the motion with the compression of the magnetic field, we find that the acceleration and deceleration of the stage should be an adiabatic process for the atom cloud. If the stage is moved with acceleration a, the atoms experience a force $F_{\mathrm{acc}} = ma$. The change of this force in time can be compared with the change of the trapping potential in a ramp of the magnetic field. Figure 3.21 shows the motion profile of the transfer with maximally realizable acceleration to the square chamber. The change of the inertial force is $\dot{F}_{\mathrm{acc}} = m\dot{a}$. In figure

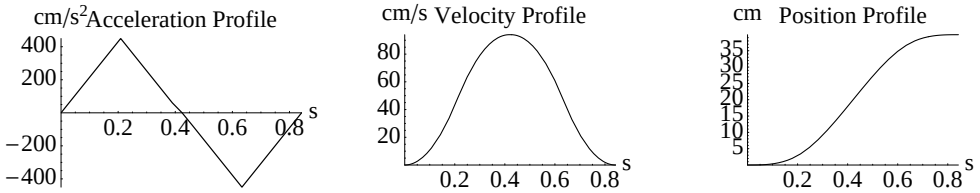

(a) (b) (c)

Figure 3.21: Motion profile of the transport to the square chamber with maximum acceleration. The transfer takes 0.84 s.

3.21(a), the acceleration is increased by $\Delta a = 450\,\mathrm{cm/s^2}$ within $\Delta t = 210\,\mathrm{ms}$. If we set the resulting change of the inertial force $\dot{F}_{\mathrm{acc}} = m\frac{\Delta a}{\Delta t}$ equal to the change of the magnetic force in a compression of the trap $\dot{F}_{\mathrm{mag}} = g_F m_F \mu_{\mathrm{B}} \frac{\Delta b}{\Delta t}$,

the motion is equivalent (for $m_F = 1$) to a ramp rate of $\frac{\Delta b}{\Delta t} = 6.7 \frac{\mathrm{G}}{\mathrm{cm}\,100\,\mathrm{ms}}$. The total acceleration increase of $\Delta a = 450\,\mathrm{cm/s^2}$ compares to a ramp height of $\Delta b = 14\,\mathrm{G/cm}$. The corresponding product of ramp rate $\Delta b/\Delta t$ and ramp height Δb as in figure 3.17(b) is $0.01\,(100\,\mathrm{G}^2)/(\mathrm{cm}^2\,\mathrm{ms})$. This is a very slow rate, and inspection of figure 3.17 confirms that it should be in very good approximation adiabatic. Thus, only extremely fast changes in acceleration, which are mechanically impossible, could cause a heating of the cloud. We also think that the transport is smooth enough to rule out the possibility of bumpiness causing abrupt small changes of the motion that would heat the cloud. We conclude that we can use motion profiles with the maximum acceleration supported by the translation stage and its mechanical limitations, which is $a_{\max} = 450\,\frac{\mathrm{cm}}{\mathrm{s}^2}$, in order to minimize the time spent in the vapor cell. For the paths 2 and 3 in figure 3.19, speed is not critical and we chose slower motions to avoid unnecessary stress of the translation stage.

3.9 Feasibility assessment for BEC

This section discusses a few general aspects of the efficiency of the entire pre-evaporation sequence as well as some figure of merits that will allow us to estimate the chances for successful evaporation.

3.9.1 Dependence of the transport efficiency on the background pressure

The background pressure in the vapor cell plays a critical role: it determines the maximally possible atom number (see equation 2.27, as long as the partial pressure of non-rubidium atoms is not negligible), but also limits the lifetime of a magnetically trapped cloud. Considering an entire sequence there are two competing effects: increasing the background pressure raises the atom number in the MOT, but increases the losses during the transport to the square chamber as well. Consequently, for a fixed transportation time (which is 840 ms if the maximum acceleration is used) to the square chamber, there is an optimum pressure, respectively lifetime. An approximate orientation about this parameter was obtained by opening the rubidium oven and thus increasing the background pressure while measuring the development of the lifetime, the number of atoms trapped in the MT, and the number of atoms that could be detected after the trap had been moved to the square chamber and back. Our measurements suffered mainly from the time necessary to conduct them (~ 3 hours for the full data set). On this time scale, laser drifts could not be avoided, tampering the results. Figure 3.22 shows the data obtained. The sudden jumps in the absolute atom numbers directly correlate with locking problems of the lasers. The maximum number of atoms after transport seems to be obtained around run 20. That means that one should aim to maintain a lifetime of ~ 2 s in the vapor cell. In a real sequence, one would only transport one way, so the optimum would shift to an even lower lifetime.

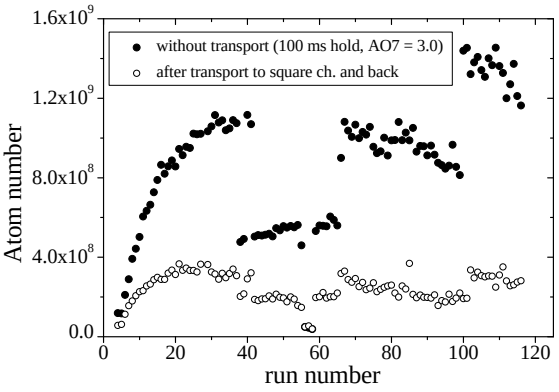

(a) Absolute transport efficiency: atom number in reference run and after transport

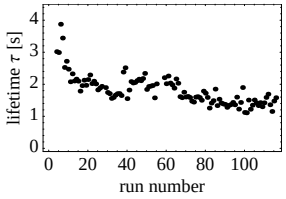

(b) Lifetime τ_{VC}

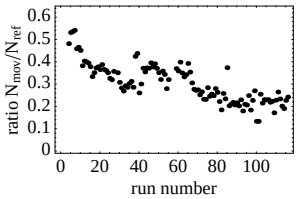

(c) Relative transport efficiency

Figure 3.22: The absolute efficiency of the transport is pressure-dependent: increasing MOT atom number and rising transport losses are competing effects resulting in an optimum background pressure (figure (a)). The lifetime (b) and the relative transport efficiency (c) decrease with rising pressure. The runs were taken in equal intervals over a time of three hours after the rubidium oven had been opened. The sudden jumps are caused by problems with holding the lock frequencies of the lasers. The ratios of atoms before and after the transport cannot be compared to those presented in section 3.9.3 because the measurements were done for $|1, -1\rangle$-atoms and the vapor cell was not isolated from residual stray light coming from the laser boxes at that time. The temperature of the rubidium oven was 30 °C.

3.9.2 Lifetime in the science cell

One very crucial parameter for the lifetime of atoms held in the science cell is, of course, the vacuum, respectively the pressure. Because of the necessary rethermalization processes, evaporation cooling is a (on the timescale of atomic physics) lengthy procedure: one evaporation cycle in the first BEC produced lasted 70 s [5]. A rule of thumb is that the lifetime of the trapped cloud in the environment where the evaporation is executed should be at least 150 times the initial elastic collision time in the cloud [53].

We determine the lifetime τ_{SC} in the science cell by a similar method as in the transport optimization: the trap is moved to the science cell, kept there for a varying time, and moved back to the vapor cell where the atom number is measured by absorption imaging. A simple exponential decay law is fitted to the data obtained. The lifetime τ_{SC} was measured at two different y-positions of the glass cell yielding two different values. This indicates again that the compressed trap is still so big that the walls of the science cell do have an influence on the lifetime, and that care must be taken to move the atoms exactly to the middle of the cell, found in section 3.8. The data again refers to measurements with $|1,-1\rangle$-atoms; clouds consisting of $|2,+2\rangle$-atoms are more compact, and thus the influence of the walls should be smaller. From the results in figure 3.23(c), we deduce a lifetime in the glass cell τ_{SC} of $\sim 100\,\mathrm{s}$. A lifetime exceeding 100 s was reconfirmed for $|1,-1\rangle$-atoms in more recent measurements by means of (more reliable) fluorescence imaging. That value for the lifetime should be long enough for evaporation until condensation under usual conditions.

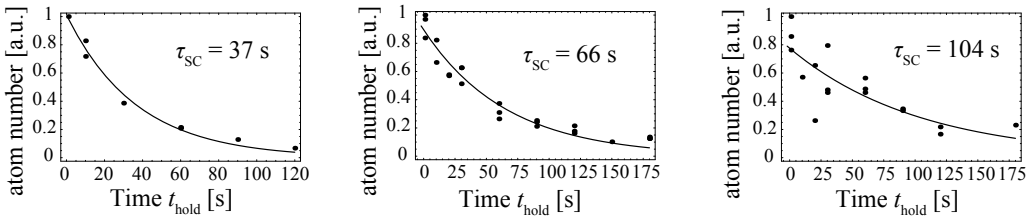

(a) $y = 2.36\,\text{cm}$, $b = 177\,\text{G/cm}$ (b) $y = 2.16\,\text{cm}$, $b = 177\,\text{G/cm}$ (c) $y = 2.16\,\text{cm}$, $b = 353\,\text{G/cm}$

Figure 3.23: Lifetime in the science cell: the data in figure (a) was taken at $y = 2.36\,\text{cm}$. The trap was then moved to a better postion ($y = 2.16\,\text{cm}$, figure (b)). In figure (c) the steepness of the trap was twice as high as in (a) and (b). The scatter of the data is caused by the problems with absorption imaging, which was used, described in appendix B.2.

3.9.3 Overall efficiency of the entire sequence

As all the optimization steps described in the previous sections were done separately, an overall estimation of the entire preparation sequence is not possible on the basis of the data from these sections. The fluctuations and changes of parameters like vapor cell pressure, laser power, laser stability, beam alignment, etc. influence the results too much and do not allow comparison of the specific data, especially regarding the values for the total atom numbers. For this reason, an analysis of the overall sequence was performed by measuring the total atom number after each single step, i. e. MOT, CMOT, molasses, MT, and transport. This procedure allows also a "fine tuning" of, e. g., the CMOT or the catch point of the magnetic field, as it turns out that the optima of these parameters depend on the total atom number.

Figure 3.24 shows the result of one of those measurements. The sequence that was used for this measurement is illustrated in appendix C. In a MOT, $\sim 9{\times}10^9$ atoms can be captured if the rubidium pressure is sufficient. In

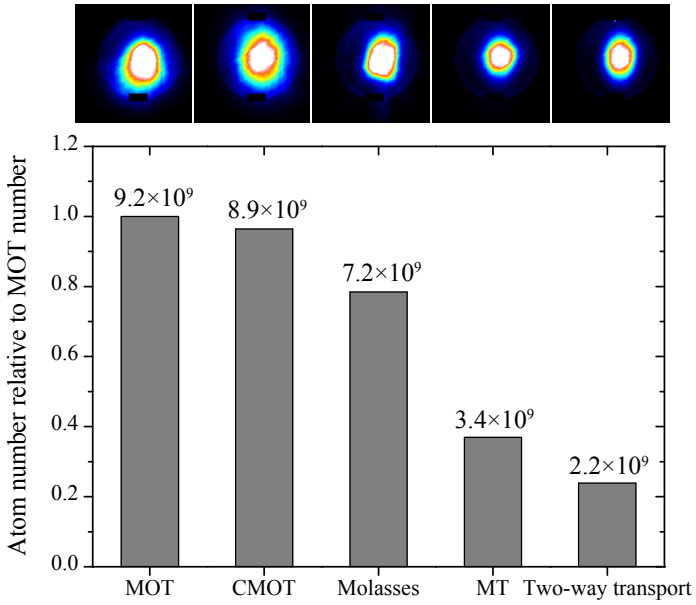

Figure 3.24: Overall efficiency of the preparation sequence: the figure shows the atom number after each step. The last two columns are clouds consisting of a mixture of $|2,+1\rangle$and $|2,+2\rangle$-atoms with a ratio of $\sim 70\,\%$ in $m_F = 2$ to $\sim 30\,\%$ in $m_F = 1$ (see section 3.6.1). The images of the clouds at each step are shown above. It can be seen that they are often not regularly and nicely shaped. The oval form of the cloud in the last image, however, reflects the shape of the quadrupole potential as the time duration of the two-way transport provides enough time for rethermalization. The color scale for the five images is dynamic.

practice, this can be guaranteed if the oven is opened every day before the experiments for a duration of $\sim 30\,\mathrm{min}$ so that the pressure can build up. We have measured MOT atom numbers as high as 1.2×10^{10}. The next step, the CMOT, is very sensitive to the atom number. While for small clouds the value of the detuning δ during compression is not very critical, careful attention must be given to it for large atom numbers. For the measurement in figure 3.24, the detuning during the 500 ms CMOT had to be changed to a linear ramp from $-4.9\,\Gamma$ to $-6.3\,\Gamma$ while the magnetic field was ramped only to a gradient of $66\,\mathrm{G/cm}$ (AO7 = 1.5 V). Large clouds extend to regions with large Zeeman shifts, which are scaled up during the compression. For this reason, the detuning has to be readjusted during the compression in order to not lose atoms in the outer regions of the cloud. After optical molasses and pumping, we are able to detect $\sim 50\,\%$ of the remaining atoms in the MT after a catch with the magnetic trap and a compression of the trap to its maximum value within 750 ms. This number is in good agreement with our analysis of the optical pumping to trappable states in section 3.6, where we found an efficiency of $\sim 50\,\%$ for large clouds. The last column in figure 3.24 represents the number of atoms detected in the vapor cell after a round trip of the fully compressed magnetic trap from the vapor cell to the science cell and back. It shows that $\sim 65\,\%$ of the original load of the trap remained. This ratio was increased from $\sim 35\,\%$ to this value after we had eliminated every possibilty of stray light by covering the laser boxes with black paperboard. We assume the losses to be caused mainly by collision with background gas atoms. The efficiency of the one-way transport would then be $\sqrt{0.65} = 80\,\%$. We can

thus expect to begin evaporation with an atom number of 2.5-3.0$\times 10^9$ atoms, which is in comparison with other experiments a promising starting point for successful Bose-Einstein condensation.

3.9.4 Rethermalization rate

The preparation in the vapor cell and the transport to the science cell will be followed by evaporative cooling. The speed of an evaporation cycle is determined by the rethermalization rate in the magnetically trapped atom cloud because after every evaporation "step"[17] the atom cloud needs to be given enough time to return to equilibrium. The lifetime of trapped atoms in the science cell, thus the time in which the complete evaporation must be performed, is long, but not infinite. For this reason, the initial rethermalization time is an important parameter to estimate the feasibility of Bose-Einstein condensation. The initial rethermalization time[18] is the duration which the thermal cloud (in the fully compressed magnetic trap) needs to return to equilibrium after a perturbation of its velocity distribution. It can be measured, e. g., by suddenly increasing the magnetic field gradient. This would cause a higher average velocity increase along the strong magnetic axis (z) than along a weak axis (e. g. y) and thus increase the width of the cloud along z, σ_z, in relation to the width along the y-axis, σ_y. After a certain rethermalization time τ_{reth}, the cloud will have re-equilibrated and the ratio of σ_z and σ_y will have reached a constant value.

[17] In reality evaporation is not executed in discrete steps, but continuously.
[18] "Initial" because this time decreases during evaporation.

Practically, one can determine τ_{reth} by measuring the ratio of the two widths $\frac{\sigma_z(t)}{\sigma_y(t)}$ as a function of time t. The duration t is the delay time between perturbation and detection. We employ the procedure illustrated in figure 3.25 to measure the rethermalization rate directly in the science cell. The

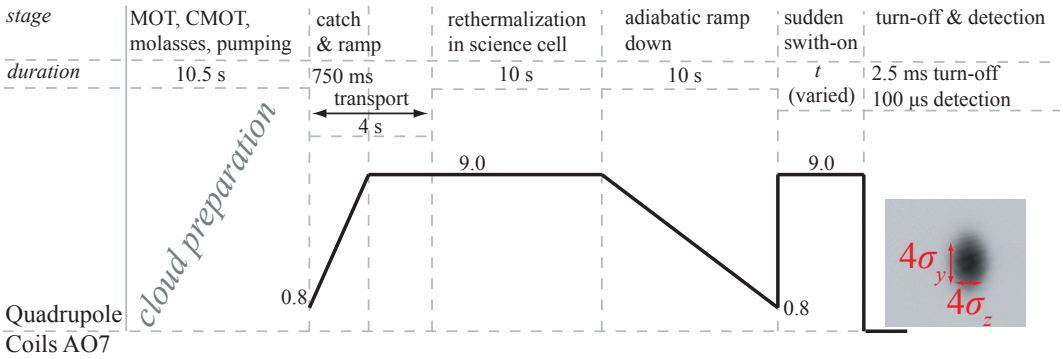

Figure 3.25: Determination of the rethermalization rate: the thermal equilibrium in the cloud is perturbed by a sudden switch-on of the magnetic field, which causes different heating along the strong and the weak axis of the trap. The time t that is given the cloud to return to equilibrium in the fully compressed magnetic trap is varied. By measuring the aspect ration $\sigma_z(t)/\sigma_y(t)$ as a function of t, one can determine the initial rethermalization time τ_{reth}.

cloud is prepared in the usual way and transferred to the science cell, where it is held with the maximum field gradient for 10 s so that equilibrium is guaranteed. Then, the trap is slowly opened by ramping the field gradient down to its catch value. This is immediately followed by a sudden switch-on of the full magnetic field, which causes asymmetric heating of the atoms along the strong and the weak axis of the field. We then vary the time t for which the cloud is held at maximum field. Doing this, we can determine the rethermalization time τ_{reth} by measuring the aspect ratio after a hold time t in the compressed trap as explained above. The images for this procedure are taken with absorption imaging in the science cell. The data obtained is shown

in figure 3.26. We measure a rethermalization time of $\tau_{\mathrm{reth}} \cong 2.0\,\mathrm{s}$. This time

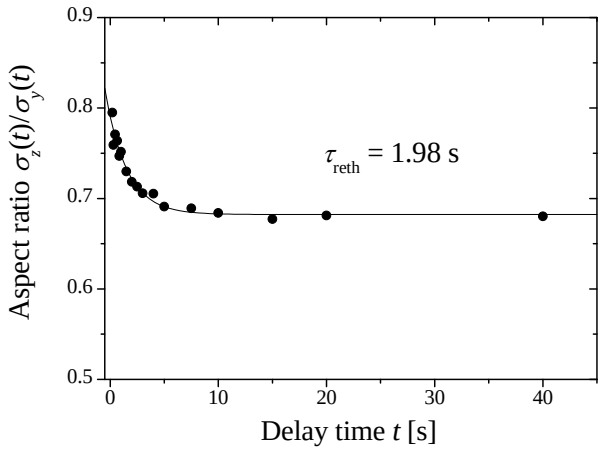

Figure 3.26: The figure shows how the aspect ratio of a thermal cloud of $|1,-1\rangle$-atoms returns to its equilibrium value. The initial rethermalization τ_{reth} time in the science cell is 2.0 s.

constant is connected to the elastic collision rate τ_{coll} by $\tau_{\mathrm{reth}} = 2.7 \times \tau_{\mathrm{coll}}$ [70]. It has been shown with Monte Carlo simulations that for successful evaporation the lifetime τ_{SC} of the magnetic trap should allow ~ 150 or more collision events [53]. With the lifetime $\tau_{\mathrm{SC}} = 104\,\mathrm{s}$ (section 3.9.2), our values yield ~ 140 collision events.

3.10 Conclusion

We have implemented an efficient pre-evaporation sequence for our BEC apparatus. After collection of $\sim 1\times 10^{10}$ atoms in the MOT from a dilute rubidium vapor, the atoms are compressed in the CMOT and cooled by optical molasses. Parameters were found for which the losses in the CMOT and molasses

stage could be minimized and efficient cooling well below the Doppler limit to $\sim 25\,\mu\mathrm{K}$ was realized. For the molasses, we measure a phase space density $\mathcal{D}$ on the order of $1{\times}10^{-5}$. Optical pumping brings about half of the atoms to trappable states. The subsequent catch with the quadrupole field was matched to the cloud size after molasses and pumping. The temperature after the catch is $\sim 80\,\mu\mathrm{K}$. The trap is quasi-adiabatically compressed to its maximum field gradient while a simultaneous transport of the trapped cloud to the science cell is initiated. We measure a phase space density for the fully compressed trap of $\sim 1.5\text{-}2{\times}10^{-7}$. More than $2{\times}10^{9}$ atoms could be detected in the vapor cell after a round trip of the magnetic trap to the science cell and back. The lifetime of the atoms in the compressed trap was measured to be $\sim 100\,\mathrm{s}$ in the science cell, where they rethermalize within an (initial) time constant of 2 s. Thus, the lifetime multiplied by the elastic collision rate of the trapped atoms is ~ 140, which is a promising value for this parameter.

All these parameters indicate very good prospects for a close realization of Bose-Einstein condensation. The phase space density in the trap as well as the collision rate are comparable to the values in other experiments while the atom number in the trap before evaporation is even slightly higher. After the development of an adequate evaporation procedure for our experimental situation, Bose-Einstein condensation should be achieved very soon. By the submission date of this thesis, a considerable increase in phase space density has, in fact, already been observed after the first trials of evaporative cooling.

Bibliography

[1] S. N. Bose, Plancks Gesetz und Lichtquantenhypothese, *Zeitschrift für Physik* **26**, 178 (1924).

[2] A. Einstein, Quantentheorie des einatomigen idealen Gases, *Sitzungsbericht der Preußischen Akademie der Wissenschaften* **XXII**, 261 (1924).

[3] A. Einstein, Quantentheorie des einatomigen idealen Gases. Zweite Abhandlung, *Sitzungsbericht der Preußischen Akademie der Wissenschaften* **II**, 3 (1925).

[4] A. Einstein, Zur Quantentheorie des idealen Gases, *Sitzungsbericht der Preußischen Akademie der Wissenschaften* **III**, 18 (1925).

[5] M. H. Anderson, J. R. Ensher, M. R. Matthews, C. E. Wieman, and E. A. Cornell, Observation of Bose-Einstein Condensation in a Dilute Atomic Vapor, *Science* **269**, 198 (1995).

[6] K. Davis, M.-O. Mewes, M. R. Andrews, N. J. van Druten, D. S. Durfee, D. M. Kurn, and W. Ketterle, Bose-Einstein Condensation in a Gas of Sodium Atoms, *Phys. Rev. Lett.* **75**, 3969 (1995).

[7] C. C. Bradley, C. A. Sackett, J. J. Tollet, and R. G. Hulet, Evidence of Bose-Einstein Condensation in an Atomic Gas with Attractive Interactions, *Phys. Rev. Lett.* **75**, 1688 (1995).

[8] C. C. Bradley, C. A. Sackett, and R. G. Hulet, Bose-Einstein Condensation of Lithium: Observation of Limited Condensate Number, *Phys. Rev. Lett.* **78**, 985 (1997).

[9] C. C. Bradley, C. A. Sackett, and R. G. Hulet, Analysis of in situ images of Bose-Einstein condensates of lithium, *Phys. Rev. A* **55**, 3951 (1997).

[10] M. R. Andrews, C. G. Townsend, H.-J. Miesner, D. S. Durfee, D. M. Kurn, and W. Ketterle, Observation of Interference Between Two Bose Condensates, *Science* **275**, 637 (1997).

[11] M.-O. Mewes, M. R. Andrews, D. M. Kurn, D. S. Durfee, C. G. Townsend, and W. Ketterle, Output Coupler for Bose-Einstein Condensed Atoms, *Phys. Rev. Lett.* **78**, 582 (1997).

[12] E. W. Hagley, L. Deng, M. Kozuma, J. Wen, K. Helmerson, S. L. Rolston, and W. D. Phillips, A Well-Collimated Quasi-Continuous Atom Laser, *Science* **283**, 1706 (1999).

[13] I. Bloch, T. W. Hänsch, and T. Esslinger, Atom Laser with a cw Output Coupler, *Phys. Rev. Lett.* **82**, 3008 (1999).

[14] M. Kozuma, Y. Suzuki, Y. Torii, T. Sugiura, T. Kuga, E. W. Hagley, and L. Deng, Phase-Coherent Amplifcation of Matter Waves, *Science* **286**, 2309 (1999).

[15] S. Inouye, T. Pfau, S. Gupta, A. P. Chikkatur, A. Görlitz, D. E. Pritchard, and W. Ketterle, Phase-coherent amplification of atomic matter waves, *Nature* **402**, 641 (1999).

[16] M. R. Matthews, B. P. Anderson, P. C. Haljan, D. S. Hall, C. E. Wieman, and E. A. Cornell, Vortices in a Bose-Einstein Condensate, *Phys. Rev. Lett.* **83**, 2498 (1999).

[17] K. Madison, F. Chevy, W. Wohlleben, and J. Dalibard, Vortex Formation in a Stirred Bose-Einstein Condensate, *Phys. Rev. Lett.* **84**, 806 (2000).

[18] Inguscio, S. Stringari, and C. E. Wieman, editors, *Proceedings of the International School of Physics Enrico Fermi, Course XVL* Amsterdam 1999 IOS Press.

[19] O. Morsch and M. Oberthaler, Dynamics of Bose-Einstein condensates in optical lattices, *Review of Modern Physics* **78**, 179 (2006).

[20] I. Bloch and M. Greiner, Exploring quantum matter with ultracold atoms in optical lattices, *Advances in Atomic, Molecular and Optical Physics* **52**, 1 (2005).

[21] K. Huang, *Statistical Mechanics* (John Wiley & Sons, New York, 1987).

[22] F. Dalfovo, S. Giorgini, L. P. Pitaevskii, and S. Stringari, Theory of Bose-Einstein condensation in trapped gases, *Review of Modern Physics* **71**, 463 (1999).

[23] H. J. Metcalf and P. van der Straten, *Laser Cooling and Trapping* (Springer, Berlin, 1999).

[24] H. F. Hess, Evaporative cooling of magnetically trapped and compressed spin-polarized hydrogen, *Phys. Rev. B* **34**, 3476 (1986).

[25] E. L. Raab, M. Prentiss, A. Cable, S. Chu, and D. E. Pritchard, Trapping of Neutral Sodium Atoms with Radiation Pressure, *Phys. Rev. Lett.* **59**, 2631 (1987).

[26] W. D. Phillips and H. Metcalf, Laser Deceleration of an Atomic Beam, *Phys. Rev. Lett.* **48**, 596 (1982).

[27] W. Petrich, M. H. Anderson, J. R. Ensher, and E. A. Cornell, Stable, Tightly Confining Magnetic Trap for Evaporative Cooling of Neutral Atoms, *Phys. Rev. Lett.* **74**, 3352 (1995).

[28] W. Ketterle, K. B. Davis, M. A. Joffe, A. Martin, and D. E. Pritchard, High Densities of Cold Atoms in a Dark Spontaneous-Force Optical Trap, *Phys. Rev. Lett.* **70**, 2253 (1993).

[29] A. Steane, P. Szriftgiser, P. Desbiolles, and J. Dalibard, Phase Modulation of Atomic de Broglie Waves, *Phys. Rev. Lett.* **74**, 4972 (1995).

[30] C. J. Myatt, N. R. Newbury, R. W. Ghrist, S. Loutzenhiser, and C. E. Wieman, Multiply loaded magneto-optical trap, *Optics Letters* **21**, 290 (1996).

[31] T. Bergeman, G. Erez, and H. J. Metcalf, Magnetostatic trapping fields for neutral atoms, *Phys. Rev. A* **35**, 1535 (1987).

[32] M.-O. Mewes, M. R. Andrews, N. J. van Druten, D. M. Kurn, D. S. Durfee, and W. Ketterle, Bose-Einstein Condensation in a Tightly Confining dc Magnetic Trap, *Phys. Rev. Lett.* **77**, 416 (1996).

[33] U. Ernst, A. Marte, F. Schreck, J. Schuster, and G. Rempe, Bose-Einstein condensation in a pure Ioffe-Pritchard field configuration, *Europhys. Lett.* **41**, 1 (1998).

[34] M. D. Barrett, J. A. Sauer, and M. S. Chapman, All-Optical Formation of an Atomic Bose-Einstein Condensate, *Phys. Rev. Lett.* **87**, 0104041 (2001).

[35] W. Hänsel, P. Hommelhoff, T. W. Hänsch, and J. Reichel, Bose-Einstein condensation on a microelectronic chip, *Nature* **413**, 498 (2001).

[36] H. Ott, J. Fortagh, G. Schlotterbeck, A. Grossmann, and C. Zimmermann, Bose-Einstein Condensation in a Surface Microtrap, *Phys. Rev. Lett.* **87**, 2304011 (2001).

[37] M. Greiner, I. Bloch, T. W. Hänsch, and T. Esslinger, Magnetic transport of trapped cold atoms over a large distance, *Phys. Rev. A* **63**, 0314011 (2001).

[38] H. J. Lewandowski, D. M. Harber, D. L. Whitaker, and E. A. Cornell, Simplified System for Creating a Bose-Einstein Condensate, *Journal of Low Temperature Physics* **132**, 309 (2003).

[39] D. E. Sproles, *in preparation*, Master's thesis, Stony Brook University, 2007.

[40] D. G. Fried, T. C. Killian, L. Willmann, D. Landhuis, S. C. Moss, D. Kleppner, and T. J. Greytak, Bose-Einstein Condensation of Atomic Hydrogen, *Phys. Rev. Lett.* **81**, 3811 (1998).

[41] S. L. Cornish, N. R. Claussen, J. L. Roberts, E. A. Cornell, and C. E. Wieman, Stable ^{85}Rb Bose-Einstein Condensates with Widely Tunable Interactions, *Phys. Rev. Lett.* **85**, 1795 (2000).

[42] G. Modugno, G. Ferrari, G. Roati, R. J. Brecha, A. Simoni, and M. Inguscio, Bose-Einstein Condensation of Potassium Atoms by Sympathetic Cooling, *Science* **294**, 1320 (2001).

[43] A. Robert, O. Sirjean, A. Browaeys, J. Poupard, S. Nowak, D. Boiron, C. I. Westbrook, and A. Aspect, A Bose-Einstein Condensate of Metastable Atoms, *Science* **292**, 461 (2001).

[44] F. P. D. Santos, J. Léonard, J. Wang, C. J. Barrelet, F. Perales, E. Rasel, C. S. Unnikrishnan, M. Leduc, and C. Cohen-Tannoudji, Bose-Einstein Condensation of Metastable Helium, *Phys. Rev. Lett.* **86**, 3459 (2001).

[45] T. Weber, J. Herbig, M. Mark, H.-C. Nägerl, and R. Grimm, Bose-Einstein Condensation of Cesium, *Science* **299**, 232 (2003).

[46] Y. Takasu, K. Maki, K. Komori, T. Takano, K. Honda, M. Kumakura, T. Yabuzaki, and Y. Takahashi, Spin-Singlet Bose-Einstein Condensation of Two-Electron Atoms, *Phys. Rev. Lett.* **91**, 0404041 (2003).

[47] A. Griesmaier, J. Werner, S. Hensler, J. Stuhler, and T. Pfau, Bose-Einstein Condensation of Chromium, *Phys. Rev. Lett.* **94**, 1604011 (2005).

[48] D. A. Steck, *Rubidium 87 D Line Data*, http://steck.us/alkalidata 2003.

[49] Y. Yoshikawa, T. Umeki, T. Mukae, Y. Torii, and T. Kuga, Frequency stabilization of a laser diode with use of light-induced birefringence in an atomic vapor, *Appl. Opt.* **42**, 6645 (2003).

[50] C. Cohen-Tannoudji, J. Dupont-Roc, and G. Grynberg, *Atom-Photon Interactions* (Wiley-VCH, Weinheim, 2004).

[51] C. Cohen-Tannoudji, Atoms in Strong Resonant Fields, in *Proceedings of Les Houches XXVII*, edited by R. Balian, S. Haroche, and S. Liberman pp. 3, Amsterdam, 1977, North Holland.

[52] A. M. Steane, M. Chowdhury, and C. J. Foot, Radiation force in the magneto-optical trap, *J. Opt. Soc. Am. B* **9**, 2142 (1992).

[53] C. J. Myatt, *Bose-Einstein condensation experiments in a dilute vapor of rubidium*, PhD thesis, University of Colorado at Boulder, 1997.

[54] C. Monroe, W. Swann, H. Robinson, and C. Wieman, Very Cold Trapped Atoms in a Vapor Cell, *Phys. Rev. Lett.* **65**, 1571 (1990).

[55] C. G. Townsend, N. H. Edwards, C. J. Cooper, K. P. Zetie, A. M. Steane, P. Szriftgiser, H. Perrin, and J. Dalibard, Phase-space density in the magneto-optical trap, *Phys. Rev. A* **52**, 1423 (1995).

[56] S. Chu, L. Hollberg, J. E. Bjorkholm, A. Cable, and A. Ashkin, Three-Dimensional Viscous Confinement and Cooling of Atoms by Resonance Radiation Pressure, *Phys. Rev. Lett.* **55**, 48 (1985).

[57] P. D. Lett, R. N. Watts, C. I. Westbrook, W. D. Phillips, P. L. Gould, and H. J. Metcalf, Observation of Atoms Laser Cooled below the Doppler Limit, *Phys. Rev. Lett.* **61**, 169 (1988).

[58] J. Dalibard and C. Cohen-Tannoudji, Laser cooling below the Doppler limit by polarization gradients: simple theoretical models, *J. Opt. Soc. Am. B* **6**, 2023 (1989).

[59] S.-Q. Shang, B. Sheehy, P. van der Straten, and H. Metcalf, Velocity-Selective Magnetic-Resonance Laser Cooling, *Phys. Rev. Lett.* **65**, 317 (1990).

[60] W. H. Wing, On Neutral Particle Trapping in Quasistatic Electromagnetic Fields, *Prog. Quant. Electr.* **8**, 181 (1984).

[61] H. Metcalf, personal communication.

[62] E. Hecht, *Optics* (Addison-Wesley, New York, 2002).

[63] H. Ruf, *Progress report from the Schneble lab*, *unpublished*, 2006.

[64] K. Lindquist, M. Stephens, and C. Wieman, Experimental and theoretical study of the vapor-cell Zeeman optical trap, *Phys. Rev. A* **46**, 4082 (1992).

[65] W. Petrich, M. H. Anderson, J. R. Ensher, and E. A. Cornell, Behavior of atoms in a compressed magneto-optical trap, *J. Opt. Soc. Am. B* **11**, 1322 (1994).

[66] C. Klempt, T. van Zoest, T. Henninger, O. Topic, E. Rasel, W. Ertmer, and J. Arlt, UV light-induced atom desorption for large rubidium and potassium magneto-optical traps, *Phys. Rev. A* **73**, 0134100 (2006).

[67] C. J. Myatt, E. A. Burt, R. W. Ghrist, E. A. Cornell, and C. E. Wieman, Production of Two Overlapping Bose-Einstein Condensates by Sympathetic Cooling, *Phys. Rev. Lett.* **78**, 586 (1997).

[68] W. Ketterle, D. S. Durfee, and D. M. Stamper-Kurn, Making, probing and understanding Bose-Einstein condensates, in *Proceedings Of the International School of Physics Enrico Fermi*, edited by M. Inguscio, S. Stringari, and C. E. Wieman pp. 67, Amsterdam, 1999, IOS Press.

[69] J. Stuhler, *Kontinuierliches Laden einer Magnetfalle mit lasergekühlten Chromatomen*, PhD thesis, Universität Konstanz, 2001.

[70] C. R. Monroe, E. A. Cornell, C. A. Sackett, C. J. Myatt, and C. E. Wieman, Measurement of Cs-Cs Elastic Scattering at $T = 30\,\mu\mathrm{K}$, *Phys. Rev. Lett.* **70**, 414 (1993).

Appendix A

Detailed explanation of lin $\perp$ lin-polarization gradient cooling

This appendix gives a more detailed treatment of the model for lin $\perp$ lin cooling proposed in [58] than the main chapter 2.

In chaper 2 it was discussed that the lin $\perp$ lin-configuration effects a spatially varying polarization that changes from circularly to linearly polarized, again back to circularly, but with opposite helicity and so on. The light shift discussed in section 2.3.3 depends on the Rabi frequency $\Omega = \frac{-eE_0}{\hbar} \langle \phi_\mathrm{e} | \hat{\epsilon}\vec{r} | \phi_\mathrm{g} \rangle$. The matrix element in that expression describes the transition. For a real atom with magnetic substates, the dependence on the polarization yields the well-known selection rules: circular σ^+-light, e. g., couples transitions with $\Delta m_J = +1$[1], light with σ^--polarization transitions with $\Delta m_J = -1$, and linearly polarized light transitions with $\Delta m_J = 0$. Spontaneous emission, however, can happen with any polarization, thus the selection rule for it is $\Delta m = 0, \pm 1$. We want to consider atoms with angular momentum $J_\mathrm{g} = 1/2$ in

[1]The quantum number m_J here is a magnetic number of an arbitrary total angular momentum, F for low fields. We do not consider atoms in the Paschen-Back regime.

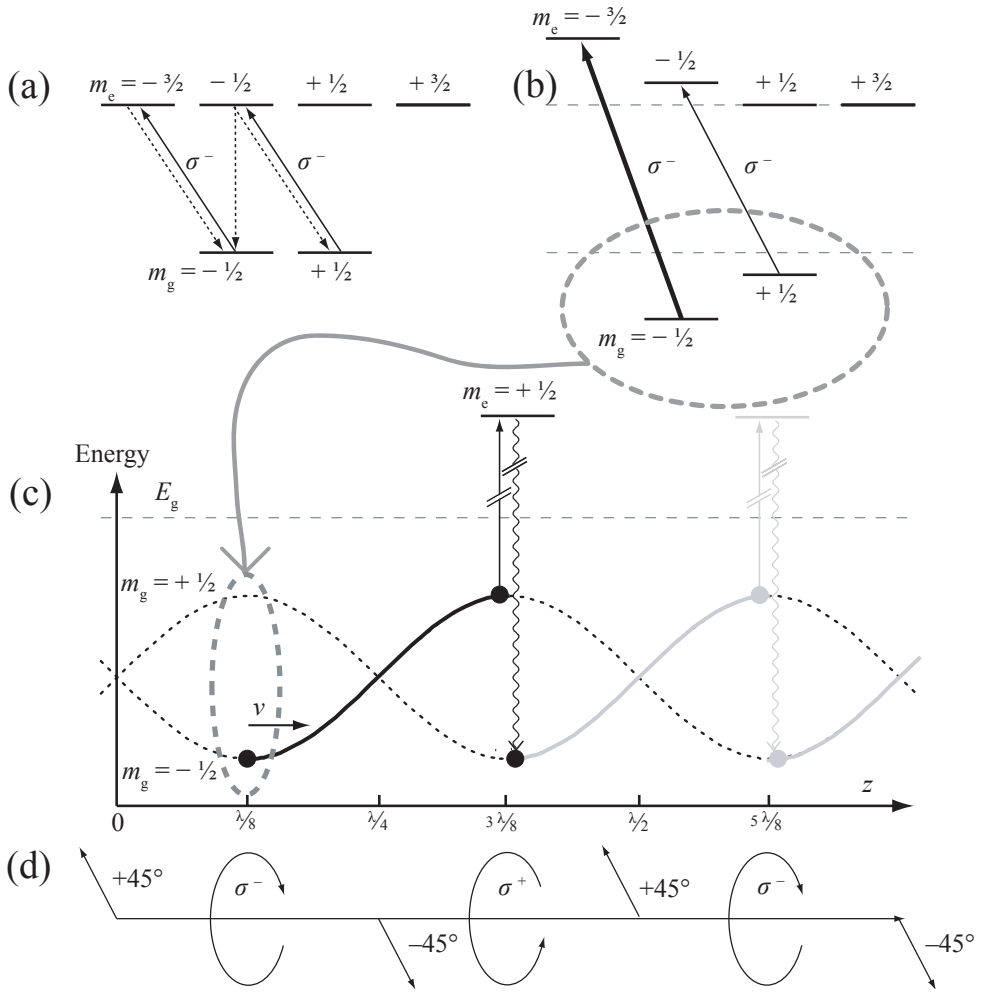

Figure A.1: lin $\perp$ lin-polarization gradient cooling: figure (a) illustrates optical pumping. The solid lines are the transitions possible with σ^--light, the dashed ones are the possibilites for spontaneous emission. Figure (b) shows the light shifts for the substates in σ^--light. Figure (c) visualizes the Sisyphus effect in this configuration. Figure (d) shows how the polarization changes within half a wavelength. The figures contain much information. Full explanations are given in the text.

the ground state and $J_e = 3/2$ in the excited state as an example. If such an atom has $m_g = 1/2$ in the ground state, then it cannot go to the $m_g = -1/2$-state: excitation can only drive the atom to $m_e = +3/2$, from where it can return only to $m_e = +1/2$ by spontaneous emission. In contrast, for atoms with $m_g = -1/2$ there is a chance to end up in the $m_g = +1/2$-state: eventually, all atoms will consequently gather in the $m_g = 1/2$-state. This process is called optical pumping, illustrated in figure A.1 (a). The matrix element also expresses the strength of a transition, which is directly proportional to the light shift. In σ^+-light, the matrix element and thus the light shift is three times larger for the $m_g = +1/2 \rightarrow m_e = +3/2$-transition than for the $m_g = -1/2 \rightarrow m_e = 1/2$-excitation (see figure A.1 (b)); the situation for σ^--light is the same, but with opposite signs. For linearly polarized light, the transitions are equally strong. In the light field of equation 2.30, this createas a spatially varying light shift shown in figure A.1. The cooling effect is now based on the following model which is visualized in figure A.1 (c): suppose an atom travels with velocity v in positive z-direction and is in the state $m_g = -1/2$ at $z = \lambda/8$ where the light is σ^--polarized. Because of the selection rules, it cannot be pumped to $m_g = +1/2$. We assume that it has traveled to $z = 3\lambda/8$ by the next absorption event. This means that it had to climb a potential hill and has converted kinetic energy to potential. At the top of the hill, the light is σ^+-polarized, so the atom will be pumped to the $m_g = +1/2$, which has a *lower* energy at that position than the $m_g = -1/2$-state. From there, it can climb the next potential hill and again be pumped to a lower state. To summarize in energy terms: by climbing the hill, the atom converts

kinetic energy to potential energy, which is then emitted to the light field. The atom loses kinetic energy, thus it is cooled. The mechanism is often called Sisyphus cooling because the repeated up-and-down in the potential reminiscent of the famous Greek myth. One can easily identify two limitations for this mechanism: if the atom is too fast, it will go over the potential hills without being scattered. If the atom is too slow, one can no longer assume that the pumping is delayed until the atom has reached the top of the hill: pumping then happens quasi-instantaneous as soon as the polarization contains a σ^+-part[2]. A time lag of the optical pumping with respect to the motion of the atom is, therefore, important such that the population of the states does not instantaneously follow the corresponding polarization at the atom's position. The optimum velocity v_{opt} is given when one pumping event happens for every climbing of a hill, so $v_{\mathrm{opt}} \approx \lambda\Gamma_{\mathrm{sc}}/4$.

[2]Note that linear polarization can be thought of as superposition of circularly polarized fields with opposite helicity.

Appendix B

Apparatus details

B.1 Vignetting

Vignetting [62] is a common effect in optics. We will discuss its influence on our measurements. In optical systems with more than one aperture, images of objects that are distant from the optical axis have a smaller luminosity than those of objects on axis. Consider the situation depicted in figure B.1 that corresponds to the situation in our imaging setup. The gray shaded areas symbolize the solid angle that can theoretically contribute to a point's image due to the finite size of the second aperture (a). If aperture (lens) 1 is not large enough, this angle will be diminished for off-axis objects resulting in a darker image than for a point on the axis of the same luminosity (b). We have calculated that for our experiment vignetting becomes a problem for point-like objects that are 21.5 mm or more away from the optical axis. If one assumes the diameter of a cloud to be 6 mm, this relates to a time of flight of 56 ms. Since we have never used such long times, the effect does not influence our

measurements.

Another minor effect with similar consequence is the variation of the angle $\alpha(r)$ in figure B.1 (a). If $l = f_1$, α is constant. In our case l is $\sim 52\,\mathrm{cm}$, so almost equal to $f_1 = 50\,\mathrm{cm}$: Even for objects at a distance where vignetting becomes relevant, the variation of $\alpha(r)$ is less than 0.01% and can thus be neglected.

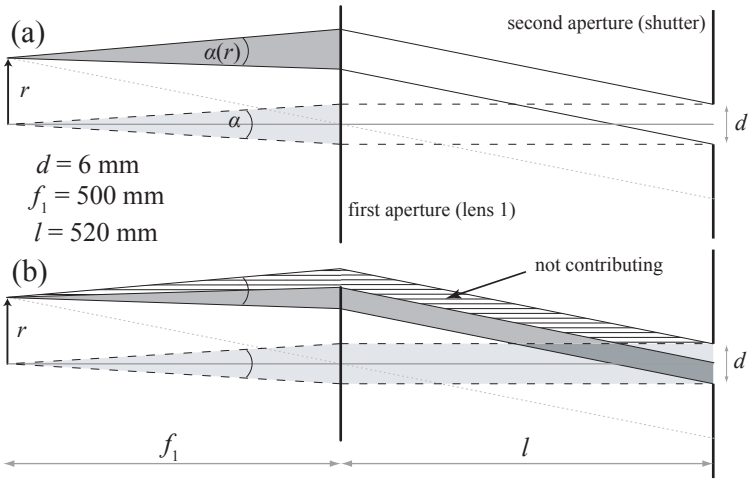

Figure B.1: Vignetting: in our setup, the variation of the angle $\alpha(r)$ in figure (a), respectively the solid angle $\Omega(r)$ that contributes to the image of a point is small over the size of the cloud: $\alpha(r)$ varies by less than 0.01% (figure (a)). Figure (b) shows the effect of vignetting: the angle $\alpha(r)$ is cut down because the diameter of the first aperture (the lens) is not large enough. Four our values this becomes a problem for $r > 21.5\,\mathrm{mm}$, which would only be relevant for very long times of flight.

B.2 Laser frequency jitter

In the course of the measurements for this thesis, a general inreproducibility for the atom numbers detected by absorption imaging was discovered. In contrast, the values obtained by fluorescence measurements, were reproducible

within 5 %. This discrepancy could be modeled by a rms-frequency jitter of the cycling laser of $\sim \pm 0.5\,\Gamma = \pm 3.0\,\mathrm{MHz}$. The specifications of the manufacturer for the linewidth of the laser is $< 1.0\,\mathrm{MHz}$. The frequency jitter influences the atom number obtained by absorption imaging more than the one obtained by fluorescence imaging for three reasons. The absorption imaging is on-resonance while the fluorescence imaging was performed with a detuning of $-3.5\,\Gamma$. A shift of the assumed frequency by a jitter weighs relatively more on-resonance than off-resonance as can be seen from equation 2.15. Thus, the jitter has a larger influence on absorption imaging than on fluorescence imaging. It was also found that the jitter is periodical with a frequency of 2 kHz, which corresponds to a period length of 500 µs. The exposure time in absorption imaging is 100 µs while we used 1 ms for fluorescence imaging. Consequently, the jitter effect averages out in fluorescence imaging, but not in absorption imaging. This was confirmed by an increase of the exposure time for absorption imaging: the fluctuations in atom number decreased for longer exposure times. Furthermore, fluorescence imaging is performed well above the saturation intensity, but absorption imaging far below. The power broadening for the fluorescence measurments reduces the sensitivity to frequency fluctuations. It was also possible to correct out the jitter of the frequency both for absorption and fluorescence imaging by monitoring and recording the frequency jitter during detection from the spectroscopy signal and calculating correction factors from this data. The jitter originates from instabilities of the voltage applied to the piezo-electric crystal of the laser. This was confirmed by measuring both the frequency jitter from the spectroscopy signal and the piezo voltage separately.

The two curves show a clear correlation. The laser was sent back to its producer, but this insufficiency could not entirely be removed, which means that the light of the cycling laser is not usable for quantitative analysis. All results in this thesis with information about absolute atom numbers were, therefore, obtained by fluorescence imaging.

B.3 Calibration of the analog channels

The calibration of the analog channels of the timing computer for cycling detuning (AO0), cycling power (AO1), repump power (AO2), and quadrupole coil current (AO7) define the "lab units" (in V applied to the channels) which are sometimes used in this thesis. For reference, the calibration curves are given in the following figure B.2.

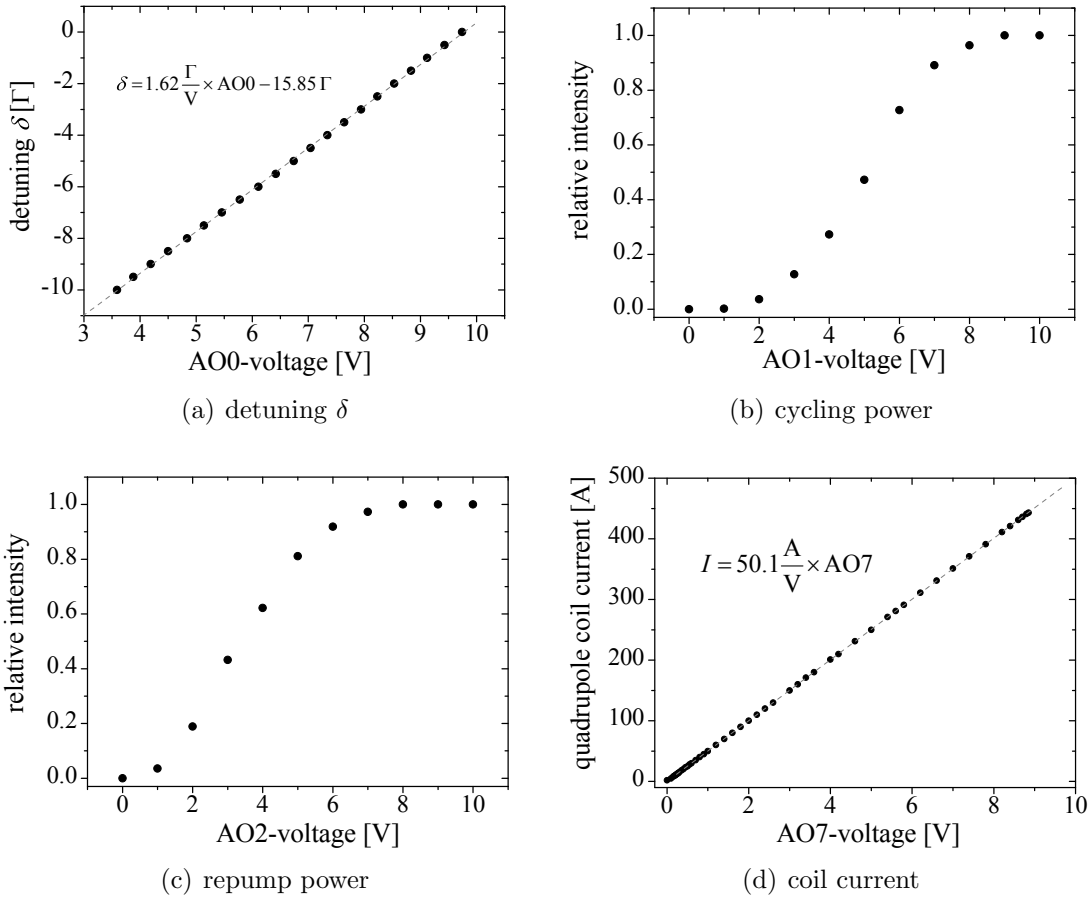

(a) detuning δ

(b) cycling power

(c) repump power

(d) coil current

Figure B.2: Calibration curves of the analog channels that define the "lab units". The data was taken by H. Ruf. The field gradient b can be calculated from the AO7-voltage by use of the regression in (d) and the field gradient per current $b/I = 0.88\,\mathrm{G/(cm\,A)}$.

Appendix C

Sequence illustration for overall efficiency experiments

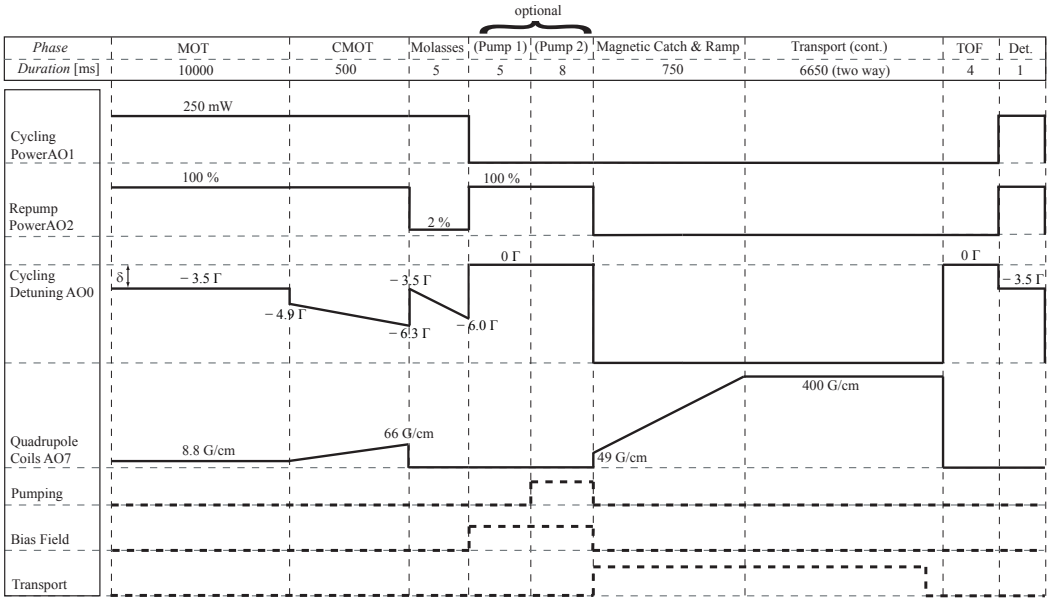

Figure C.1: The figure illustrates the preparation sequence that was used for the last data point ("two-way transport") in the overall efficiency measurements described in section 3.9.3. The atom numbers for the other stages ("Mot", "CMOT", "Molasses", "MT") were taken with the same parameters, but only the corresponding steps activated.

Appendix D

Abbreviations and rubidium properties

The following symbols may be used with a global meaning in this thesis. If they are not differently defined in the specific context of a section, they represent:

c	the speed of light in vacuum: $299\,792\,458\,\frac{\mathrm{m}}{\mathrm{s}}$
$\hbar$	reduced Planck constant: $1.054\,571\,628 \times 10^{-34}\,\frac{\mathrm{kg\,m^2}}{\mathrm{s}}$
e	elementary charge: $1.602\,176\,487 \times 10^{-19}\,\mathrm{A\,s}$
μ_B	Boor magneton: $9.274\,009\,15 \times 10^{-24}\,\mathrm{A\,m^2}$
u	atomic mass unit: $1.660\,538\,782 \times 10^{-27}\,\mathrm{kg}$
k_B	Boltzmann constant: $1.380\,6504 \times 10^{-23}\,\frac{\mathrm{kg\,m^2}}{\mathrm{K\,s^2}}$
g	standard acceleration of gravity: $9.806\,65\,\frac{\mathrm{m}}{\mathrm{s^2}}$
x	variable of a Cartesian coordinate system with variables x, y, z
y	variable of a Cartesian coordinate system with variables x, y, z
z	variable of a Cartesian coordinate system with variables x, y, z
$\hat{\epsilon}$	a unit vector
n	density of a gas, usually the density of a rubidium cloud
N	the amount of something, usually the number of rubidium atoms in a MOT, MT, etc.
V	volume
σ	$1/\sqrt{\mathrm{e}}$-width of a Gaussian distribution

$\mathcal{D}$	phase space density
m	mass of the isotope ^{87}Rb of rubidium
v	velocity
ω_l	laser light angular frequency $[2\pi \cdot \mathrm{Hz}]$
ω_a	atomic transition angular frequency: $\Delta E/\hbar$ $[2\pi \cdot \mathrm{Hz}]$
ω	atomic transition or laser angular frequency when difference between ω_l and ω_a is not relevant
δ	detuning of the laser from resonance: $\omega_\mathrm{l} - \omega_\mathrm{a}$ $[2\pi \cdot \mathrm{Hz}]$
λ	wavelength: $\frac{2\pi c}{\omega}$
k	wavenumber: $\frac{2\pi}{\lambda}$
Ω	Rabi frequency: $\sqrt{\omega^2 + \delta^2}$
Γ	natural linewidth of transition $[2\pi \cdot \mathrm{Hz}]$
Γ_sc	total scattering rate
σ_sc	scattering cross section
I	intensity of laser beam(s)
I_s	saturation intensity: $\frac{2\pi^2\hbar c\Gamma}{3\lambda^3}$
s_0	saturation parameter: $\frac{I}{I_\mathrm{s}}$
σ^+	left-circular polarization, helicity: $+1$
σ^-	right-circular polarization, helicity: -1
$\vec{E}$	an electric field
B	magnitude of magnetic field
b_j	magnetic field gradient in $\hat{\epsilon}_j$-direction ($j \in x, y, z$) at field zero: $\frac{\partial B}{\partial j}\Big\vert_{\vec{r}=(0,0,0)}$
b	magnetic field gradient in z-direction: $b := b_z$
J	total angular momentum number in theoretical considerations
g_J	Landé g-factor of J
m_J	magnetic quantum number of J
F	quantum number of total angular momentum $\vec{F} = \vec{L} + \vec{S} + \vec{I}$
g_F	hyperfine Landé g-factor of F

m_F	hyperfine magnetic quantum number of F
T	temperature
T_{D}	Doppler temperature limit: $\frac{\hbar\Gamma}{2k_{\mathrm{B}}}$
BEC	Bose-Einstein condensate *or* Bose-Einstein condensation
Rb	rubidium
MOT	magneto-optical trap
CMOT	compressed magneto-optical trap
MT	magnetic trap
TOP	time-orbiting potential
CCD	charge-coupled device
AOM	acousto-optical modulator
a. u.	arbitrary units
FWHM	full width at half maximum

Below some physical properties of ^{87}Rb are listed. The list contains only data relevant in equations used in this thesis. All spectroscopic data relates to the $5\,^2\mathrm{S}_{1/2} \rightarrow 5\,^2\mathrm{P}_{3/2}$-transition ($\mathrm{D}_2$). The values are taken from reference [48].

Z	Atomic number: 37
$Z + N$	total nucleons: 87
m	atomic mass: 86.909 180 520 u
T_M	melting point: 39.31 °C
p_V	vapor pressure at 25 °C: 3.0×10^{-7} torr
I	nuclear spin: $^3/_2$
ω_a	frequency: $2\pi \cdot 3.842\,304\,844\,68 \times 10^{14}$ Hz
λ_a	wavelength in vacuum $\frac{2\pi c}{\omega_\mathrm{a}} = 780.241\,209\,686$ nm
$\hbar\omega_\mathrm{a}$	transition energy: 1.589 049 439 eV
k_a	wavenumber $\frac{2\pi}{\lambda_\mathrm{a}} = 2\pi \cdot 12\,816.549\,389\,93\,\mathrm{cm}^{-1}$
Γ	natural line width (FWHM): $2\pi \cdot 6.065$ MHz
τ	lifetime: 26.24 ns
T_D	Doppler temperature limit: 146 µK
$g_{F=2}(5\,^2\mathrm{S}_{1/2})$	hyperfine Landé g-factor for $5\,^2\mathrm{S}_{1/2}, F = 2$: $^1/_2$
$g_{F=1}(5\,^2\mathrm{S}_{1/2})$	hyperfine Landé g-factor for $5\,^2\mathrm{S}_{1/2}, F = 1$: $^{-1}/_2$
$I_\mathrm{sat}(F = 2 \rightarrow F' = 3, \mathrm{iso})$	effective saturation intensity for cycling transition with isotropic polarization: 3.576 $\frac{\mathrm{mW}}{\mathrm{cm}^2}$
$I_\mathrm{sat}(F = 2 \rightarrow F' = 3, \sigma^+)$	saturation intensity for cycling transition $\lvert F = 2, m_F = +2\rangle \rightarrow \lvert F' = 3, m_{F'} = +3\rangle$: 1.669 $\frac{\mathrm{mW}}{\mathrm{cm}^2}$